

CHARLES UNIVERSITY IN PRAGUE.  
FACULTY OF MATHEMATICS AND PHYSICS  
DEPARTMENT OF CHEMICAL PHYSICS AND OPTICS

---

# Optical properties of silicon nanostructures

DOCTORAL THESIS



Mgr. Petr Janda

Advisor:  
Doc. RNDr. Jan Valenta, Ph.D.  
Prague, 2007

---

UNIVERZITA KARLOVA V PRAZE,  
MATEMATICKO-FYZIKÁLNÍ FAKULTA  
KATEDRA CHEMICKÉ FYZIKY A OPTIKY

---

# Optické vlastnosti křemíkových nanokrystalů

DISERTAČNÍ PRÁCE



Mgr. Petr Janda

Školitel:  
Doc. RNDr. Jan Valenta, Ph.D.  
Praha, 2007

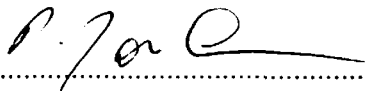
---

### Acknowledgement

I am very thankful to my adviser Doc. J. Valenta for his support during my PhD. study and I would also like to thank T. Ostatnicky, PhD. for his assistance during preparation of theoretical part of this work.

This work was supported by the following projects: the research plan MSM 0021620835 and the research center LC510 from the Ministry of Education of the Czech Republic, GAČR 202/03/0789 from the Grant Agency of Czech Republic, GAAV IAA1010316 from the Academy of Sciences of the Czech Republic and Australian Research Council Discovery Project DP0343308.

Prague, 28 February 2007

  
.....  
Mgr. Petr Janda

# Contents

<b>1</b>	<b>Introduction</b>	<b>3</b>
<b>2</b>	<b>Theoretical background</b>	<b>5</b>
2.1	Quantum confinement in nanocrystals . . . . .	5
2.1.1	Particle in a box . . . . .	6
2.1.2	Coulomb interaction . . . . .	7
2.2	Nanocrystals . . . . .	8
2.2.1	Si nanocrystals . . . . .	10
2.3	Optical properties of semiconductors . . . . .	14
2.3.1	Absorption . . . . .	15
2.3.2	Optical gain . . . . .	16
2.3.3	Waveguides . . . . .	17
2.4	Photonic crystals . . . . .	19
<b>3</b>	<b>Semiconductor nanocrystalline materials</b>	<b>21</b>
3.1	Preparation methods . . . . .	21
3.1.1	Nanocrystalline layer on the surface . . . . .	22
3.1.2	Nanocrystals embedded inside a matrix . . . . .	23
3.2	Studied materials . . . . .	24
3.2.1	Porous silicon and its colloids . . . . .	24
3.2.2	Nanocrystals implanted in silica glass . . . . .	27
3.2.3	Artificial opals . . . . .	30
<b>4</b>	<b>Experimental techniques</b>	<b>32</b>
4.1	Size and morphology determination . . . . .	32
4.2	Optical transitions . . . . .	35
4.2.1	Luminescence measurement . . . . .	36
4.2.2	Spatial distribution of luminescence . . . . .	37
4.2.3	Light coupling into a sample . . . . .	40
4.3	Strong excitation effects in nanocrystals . . . . .	43
4.3.1	Permanent grating burning . . . . .	43
4.3.2	Pump-and-probe measurement . . . . .	44
4.4	Spectral detection . . . . .	45
4.5	Single nanocrystal spectroscopy . . . . .	47



<b>5</b>	<b>Results and discussion</b>	<b>48</b>
5.1	Luminescence of porous silicon colloids . . . . .	48
5.2	Implanted silica glasses . . . . .	50
5.2.1	Characterization of samples . . . . .	50
5.2.2	Theory of Si waveguides . . . . .	52
5.2.3	Angular measurement of luminescence . . . . .	54
5.2.4	Waveguiding properties . . . . .	59
5.2.5	Prism coupling . . . . .	60
5.2.6	Direct coupling . . . . .	62
5.2.7	Permanent grating burning . . . . .	66
5.2.8	Pump and probe experiment . . . . .	68
5.3	Photonic crystals . . . . .	70
<b>6</b>	<b>Conclusion</b>	<b>73</b>
6.1	Presented results . . . . .	73
6.2	Future development of nanocrystalline materials . . . . .	74
<b>A</b>	<b>Published results</b>	<b>81</b>

# 1 Introduction

Nowadays, electronics systems are built of several different materials. With several exceptions, most electronics components are based on silicon. Integrated optical devices are mostly based on III-V and II-VI semiconductors. These materials are used for preparation of light emitting devices like laser diodes and light emitting diodes (LED), where energy gap and consequently emission wavelength are easily tunable by changing the ratio of materials in a compound. However, connection of these optical devices and electronic integrated circuits based on silicon is not easy due to the mismatch of lattice constants.

There are several research directions in integrated optoelectronic devices. One of them is investigation of light-emitting silicon structures potentially compatible with the current semiconductor technology. The possibility of combining light sources and detectors with integrated circuits on one chip is very interesting.

Bulk Si is an indirect band gap material with very low efficiency of radiative recombination. In fact, weak luminescence can be detected only at very low temperatures. However, there are some "tricks" to increase light-emission in bulk silicon and even to fabricate LEDs [1]. The principle consists in reducing non-radiative relaxation channels by restricting diffusion length.

Despite this fact, the low dimensional structures, nanocrystals, are even more attractive and promising. The discovery of luminescence in nanometric size silicon in 1990 [2] triggered large research effort toward the light-emitting devices based on low dimensional silicon. Such development could result in preparation of luminescence devices compatible with optoelectronic integrated circuits.

Construction of a light emitting device is, however, only the first step. The second step should be to answer the question of possible laser construction on such materials. Laser is based on nonlinear effects of material, so study of this property can provide the desired answer. An article on the possibility of nonlinear effects and on promising results leading to optical gain on Si nanoscale material was published at the end of the 20<sup>th</sup> century [3]. Optical gain in implanted layers of Si nanocrystals was first reported in the Nature magazine in 2000 [4] and the first laser based on Si was also produced [5]. However, it is not possible to yield optical gain so easily as it looks from results. Many other articles presented in various journals do not observe optical gain, even on similar materials. That is why the question of

optical gain on Si materials is not solved yet and why this thesis would like to provide some new information on this popular topic.

The above-mentioned perspectives considers present electronics build on a single chip, but still on the same basis as it is known in these days. Another possible direction of integrated circuits development could be linked to a much bigger change than simply the change of a light source and a detector. The size of electronic parts approaches the physical limit connected with influence of individual moving electrons to each other. The solution could be in using optics and photonics that means to substitute electrons with photons. The main usage will be in inter- or even intra-chip communications. The change of some electronics to photonics is still a long way, but it could bring many advantages to future informatics development.

This thesis follows both the possible directions of future development and contains a study of perspective optoelectronic materials as well as a perspective photonic materials. Silicon nanocrystals can be prepared by various experimental techniques. In our laboratory, three of them are studied: silica glasses implanted with Si nanocrystals, photonic crystals containing Si nanocrystals and colloids of porous silicon.

The study of waveguiding properties of implanted nanocrystals in silica glasses is the main part of this work. Its aim is to compare the theoretical models of this structure with the experiment and decide which model is correct. For all materials, the basic aim is to determine influence of different preparation conditions on properties of the samples. Colloids are influenced not only by preparation of silicon material, but also by a solvent. The photonic crystals implated by Si nanocrystals are really a new material, so the aim is to study luminescence of this structure and influence of the photonic band gap on nanocrystals.

## 2 Theoretical background

Material science is an important branch of science in which much work has been done up to now. That is why many (semiconductor) bulk materials have already been well characterized. Over the past decades, development focuses on low dimensional structures that present many important features originally visible only at low temperatures - for example presence of an exciton.

The decreasing size of studied materials, fabrication of new materials that consist of particles only few nm large, reveals new unusual properties coming from the so called quantum confinement effect. This effect is a result of a quantum theory coming into effect on such small materials.

Nanocrystals, the particles described in this thesis, are quantized structures confined in all three dimensions. Other confined structures are the following: A thin film of a material representing a 2D structure confined in one direction is usually called a quantum well. By adding a barrier to separate parts of the film, quantum wires (1D structure) are created. Further confining leads to quasi 0D structures, called quantum dots or artificial atoms [8].

Several names are used for 0D structures in literature: nanoparticle, nanometer-size crystal, quantum dot or nanocrystal. This work operates mostly with the term nanocrystal, because this term is used mainly for real material containing this small particles, in contrast to a quantum dot that is currently used more for theoretical study as a model system.

In the following paragraphs, we will give a brief introduction into this theory starting from the basics of quantum theory and continuing with the description of its use for real structures. The description will finally end by special samples (real structures) showing interesting properties.

### 2.1 Quantum confinement in nanocrystals

Quantum theory description will start with a stationary Schrödinger equation for a particle in a spatially periodic potential that is present in a bulk material. The electron states are usually obtained by solving Schrödinger equation in a form

$$\left(-\frac{\hbar^2}{2m}\nabla^2 + V(z)\right)\psi(x, y, z) = E\psi(x, y, z) \quad (1)$$

In a bulk crystal, periodic lattice gives potential

$$V(r) = V(r + R) \quad (2)$$

where  $R$  is a lattice vector.

Eigenstates for electrons  $\psi_{n,k}(r)$ , obtained from solution of the above-mentioned Schrödinger equation (eqn.1) are in form

$$\psi_{n,k}(r) = e^{i\mathbf{k}\times\mathbf{r}} u_{n,k}(r) \quad (3)$$

composed of an envelope function  $e^{i\mathbf{k}\times\mathbf{r}}$  and a periodic function  $u_{n,k}(r)$  with periodicity  $R$  (similar as for the potential). From these equations, we could get energy eigenvalues for a bulk material.

### 2.1.1 Particle in a box

In the following paragraphs, we take an example of an indefinitely high potential well of width  $L$  that confines movement of a particle in the  $z$  direction. Potential  $V(z)$  is defined by equations

$$\begin{aligned} V(z) &= 0 & \text{for } |z| \leq L_z \\ V(z) &= \infty & \text{for } |z| \geq L_z \end{aligned} \quad (4)$$

In such case, the solution of the Schrödinger equation (eqn.1) can be separated into two parts

$$-\frac{\hbar^2}{2m} \left( \frac{\partial}{\partial x^2} + \frac{\partial}{\partial y^2} \right) \phi(x, y) = E_{\perp} \phi(x, y) \quad (5)$$

$$-\frac{\hbar^2}{2m} \left( \frac{\partial}{\partial z^2} + V(z) \right) \xi(z) = E_z \xi(z) \quad (6)$$

The first part describes a free particle in 2D space without any confinement and the second one describes a particle confined in a quantum well. Solution of this basic quantum problem can be found in many books on quantum theory (for example [6]).

The total energy spectrum of a particle is a sum of both components

$$E_{\perp} + E_z = E = \frac{\hbar^2}{2m} \left( k_x^2 + k_y^2 + \frac{j_z^2 \pi^2}{L_z^2} \right) \quad (7)$$

When potential restricts movement in all directions, we get a structure confined in all three dimensions (0D structure). Energy spectra for that case will be in form

$$E = \frac{\hbar^2}{2m} \left( \frac{j_x^2 \pi^2}{L_x^2} + \frac{j_y^2 \pi^2}{L_y^2} + \frac{j_z^2 \pi^2}{L_z^2} \right). \quad (8)$$

where  $j_x, j_y, j_z$  quantum numbers have been introduced.

In reality, a barrier is always finite. The solution of a rectangular potential well with a definite height of confining potential is more complex [6]. The calculation could be separated into two cases: a particle with energy lower and a particle with energy higher than the border potential. An energy spectrum for a particle with lower energy contains discrete levels similar to the solution of an infinite potential. While an infinite barrier prevents a particle to be outside the potential well, a finite barrier does not confine a particle inside the well so strictly. Wavefunction outside the confining potential has a form of an exponential tail, in contrast to the case of an infinite barrier where such effect does not exist. A particle with energy exceeding the confining potential energy behaves like a free particle and does not feel confining potential. Energy spectrum of this particle is continuous.

### 2.1.2 Coulomb interaction

The previous description was a single particle approximation. However, this approximation neglects interactions between individual electrons and surface/interface effects. A more sophisticated method could reveal more about effects present in confined materials under our study.

The next step towards an exact treatment is to include the Coulomb interaction between an electron and a hole. Hamiltonian with Coulomb interaction has the following form

$$H = -\frac{\hbar^2 \nabla_e^2}{2m_e} - \frac{\hbar^2 \nabla_h^2}{2m_h} - \frac{e^2}{\epsilon |r_e - r_h|} + V_e(r_e) + V_h(r_h) \quad (9)$$

where  $m_e(m_h)$  is an effective weight of an electron (hole),  $r_e(r_h)$  are spatial coordinates of electrons (hole),  $V_e(V_h)$  are potentials for the electron (hole) and  $\epsilon$  is permittivity of free space.

In bulk materials, the influence of the Coulomb potential is essential and it is the reason for existence of excitons. The bulk Hamiltonian (eqn. 9 without the confining potential  $V_h$  and  $V_e$ ) is separable into the relative and center of mass motion of electron-hole pair. In spherical quantum dots, due to the broken symmetry, Coulomb potential depends on spatial distance between an electron and a hole.

Equation was solved using perturbation theory [7] and the lowest excited state is then given by

$$E_{10} = \frac{\hbar^2 \pi^2}{2R^2} \left( \frac{1}{m_e} + \frac{1}{m_h} \right) - \frac{1.8e^2}{\epsilon_2 R} \quad (10)$$

where  $R$  is the distance between particles.

Changing from single electron description to two particles, we get an exciton-bounded state of an electron and a hole. Basic characteristics of an exciton is its binding energy and related Bohr radius. There is analogy between an exciton and a hydrogen atom. The difference is, that exciton has a hole (with much smaller effective mass compared to a proton) instead of a nucleus formed by a single proton in case of hydrogen atom and consequently the exciton binding energy is much smaller. In semiconductors, we speak about Wannier excitons, whose radius is much larger than a lattice constant. Observing exciton in bulk material is generally restricted to low temperatures, because the binding energy in semiconductors reaches only several meV which is less than the vibrational energy at room temperature. However, in nanocrystals, the binding energy of exciton increases and in some cases it is possible to observe excitons even at room temperature.

## 2.2 Nanocrystals

At the beginning of this section, conditions under which a structure could be called a nanocrystal should be defined more precisely. The size, determining whether a structure should be called a nanocrystal, does not depend on the structure's specific size in nm, but is obtained by a comparison with the Bohr diameter of exciton for a given material. The particles (nanocrystals) of size smaller than Bohr diameter contain discrete energy spectra that change into a classical band structure when the size of particles grows.

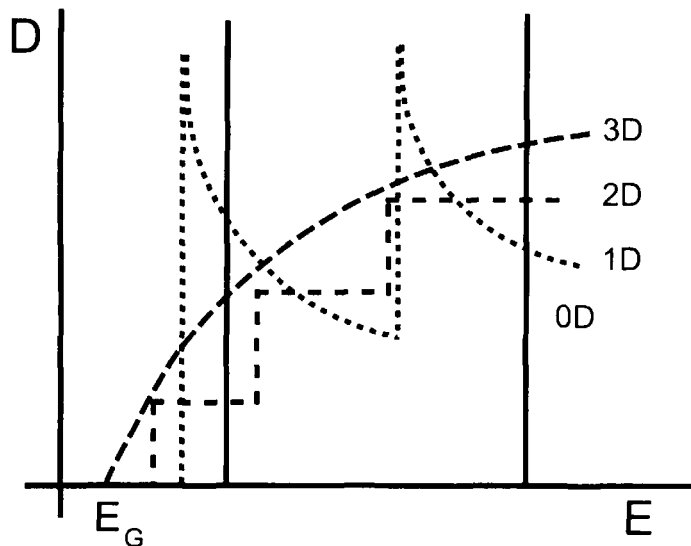


Figure 1: Density of states changing with respect to the quantum confinement.  $E_G$  is bulk energy gap. The lowest energy level moves to higher energy for lower dimension of material. Function of density of states dependence on energy changes from continuous function for bulk material to delta functions for 0D material.

The energy spectra of a nanocrystal, as a structure confined in all directions, can be approximated by a quantum well with the potential  $V$  indefinite in all directions. Solution of the Schrödinger equation then gives energy states given by equation (8). This solution is valid for cubic nanocrystals but could give good estimate also for real nanocrystals with shape much different from a cube. This basic model of a nanocrystal is used in many works and results agree well with the measured spectra.

Change from the band structure to the discrete level system is linked to the change of states density distribution. Energy states density  $D(E)$  determines the number of energy states in a small energy interval. In case of bulk materials, for band structure, this is a continuous function of energy. Quantum confinement changes function from continuous spectra into discrete levels for nanocrystals (Fig. 1). The discrete values of  $D(E)$  should lead to sharp absorption and emission spectra. However, different sizes of particles



in the material cause important inhomogeneous broadening of spectra in real materials.

Precise evaluation of Schrödinger equation with the Coulomb interaction is performed separately for particles divided into three groups according to their size in relation to Bohr diameter of exciton. We call them weak, strong and intermediate confinement regimes.

Weak confinement describes a situation where a particle is several times bigger than Bohr exciton diameter. The Coulomb interaction is the dominant effect and the quantization of kinetic energy of excitons is only a perturbation. Quantum confinement shifts spectra to higher energies (blue shift).

For particles smaller than Bohr exciton (strong confinement), we can consider only quantum confinement effect for electrons and holes and neglect Coulomb interactions. Free excitons are not present in this case and the Coulomb interaction between electrons and holes can be considered only as a small perturbation.

Situation is more complicated for particle size between these two variants. We can define a donor like exciton and consider effective mass of a hole (much higher than the effective mass of an electron) located at the center of a quantum dot. This case is often effective, because many nanocrystals are of a size comparable with the Bohr exciton diameter.

Another important aspect of nanoparticle properties, when compared to bulk material, is a large surface/volume ratio. This effect enhances influence of a surface related phenomena, like trap and interface states.

### 2.2.1 Si nanocrystals

In direct band gap materials, the minimum of the conduction band and the maximum of the valence band are coincident in the k-space. Hence, the probability of radiative recombination is high and radiative life time is of the order of a few nanoseconds. Silicon is an indirect band gap material. Thus, the energetically lowest transition is optically forbidden and appears in spectra only by assistance of momentum conserving phonon or impurity [11].

The radiative recombination of an electron and a hole has low probability in those materials. It can be increased either by increasing non-radiative life time, or by reducing radiative life time. Quantum confinement can support reduction of radiative life time due to the increasing probability of radiative transition. According to the Heisenberg's uncertainty relations, particles confined in spatial coordinate are more indefinite in k-space, which leads

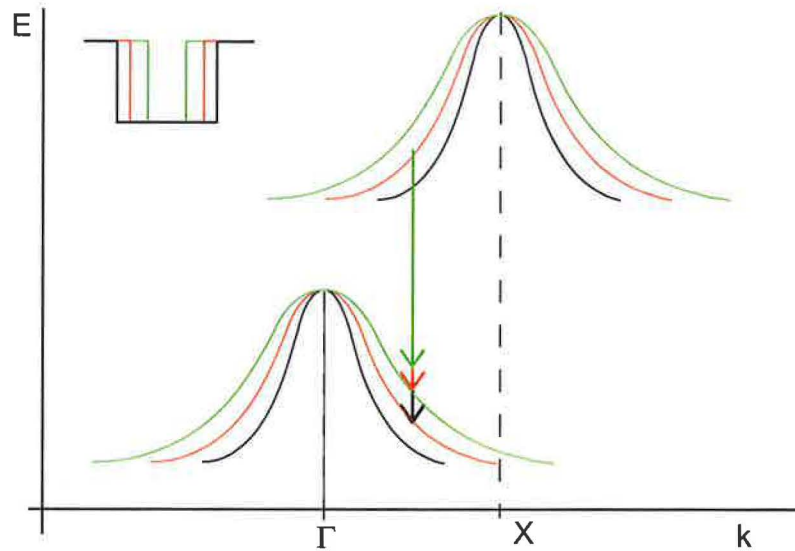


Figure 2: Schematic representation of wave function change caused by the decrease of the nanocrystal size (upper left corner present size of nanocrystal for each distribution)

to the  $k$ -space overlap of an electron and a hole wave function (sometimes described as breaking of the  $k$ -conservation rule effect [13, 1]) Fig. 2.

As described above, the quantum confinement effect appears when the geometric dimensions of nanostructures reach the value of the bulk excitonic Bohr radius. In silicon, it is about 4.3 nm [20].

One of the most challenging tasks concerning Si nanocrystals is determination of their energy gap size dependence. Obviously, the energy band gap is increasing with decreasing size, but the form exact of that dependence varies according to the theoretical approach. A large number of calculation methods have been used for evaluation of an energy gap (tight binding, electron mass approximation, etc. [1, 11]). However, in all cases one feature is similar - an increase in the energy gap with decreasing size of a crystalline particle. For sizes lower than 10 nm, growth in the energy band gap is observable. Luminescence quantum efficiency thus increases by several orders of magnitude, compared to the bulk silicon.

Theoretical works point out that chemistry of surface can have impact

on structural, electronic and optical properties of Si nanocrystals - mainly concerning nanocrystals on surface. Calculations and explanations usually start with H(hydrogen)-passivated Si nanoclusters and continue with H substituted by O(oxygen). Two forms of oxygen passivation are possible, Si-O-Si bridge bonds or Si=O double bonds. Simple bonds have minor influence on energy spectra, but surface structure is touched largely. On the other hand, Si=O (double) bonds cause only small surface distortion, but induce a huge redshift of the photoluminescence spectra [1].

Influence of O binding inside the material is also discussed in [12]. Calculation of electronic states for various sizes of Si nanocrystals leads to dependence presented in Fig. 3. If nanocrystals are oxygen passivated, stable electronic state connected with the Si=O (double) bond is formed. For nanocrystals passivated in this way, three recombination mechanisms are suggested. Zone I - free excitons - the photoluminescence energy increases with the confinement. Zone II describes recombination involving trapped electrons and free holes. As size decreases, the photoluminescence energy increases, but not so fast as was predicted by simple quantum theory, since the trapped electron level is nearly size independent. Zone III contains recombination of trapped both electrons and holes. Energy increases much slower than supposed by the theory.

Transition probability is also size dependent. The transition matrix element evaluation is very sensitive to the symmetry and the k-space overlap of the electron and hole wave functions. The general tendency is a large enhancement of several orders of magnitude. The decay time predicted by the theory reaches the range of microseconds for sizes below 2.5 nm in diameter. Such Si nanospheres are characterized by optical properties between those of direct and indirect gap semiconductors. However, theoretical increase of transition probability does not automatically imply an increased quantum efficiency resulting from confinement. As will be shown later, the luminescence decay time and the quantum yield are determined by the ratio between radiative and nonradiative transitions which can change for other reasons than quantum confinement.

The previous paragraphs presented behavior of a perfect nanocrystal. However, real material contains a large number of nanocrystals with various sizes. Energy gap changes for each nanocrystal size and hence an ensemble of particles with certain size distribution presents large inhomogeneous broadening of emission and absorption band. Distribution of sizes could be controlled during preparation process of the sample. Inhomogeneous broad-

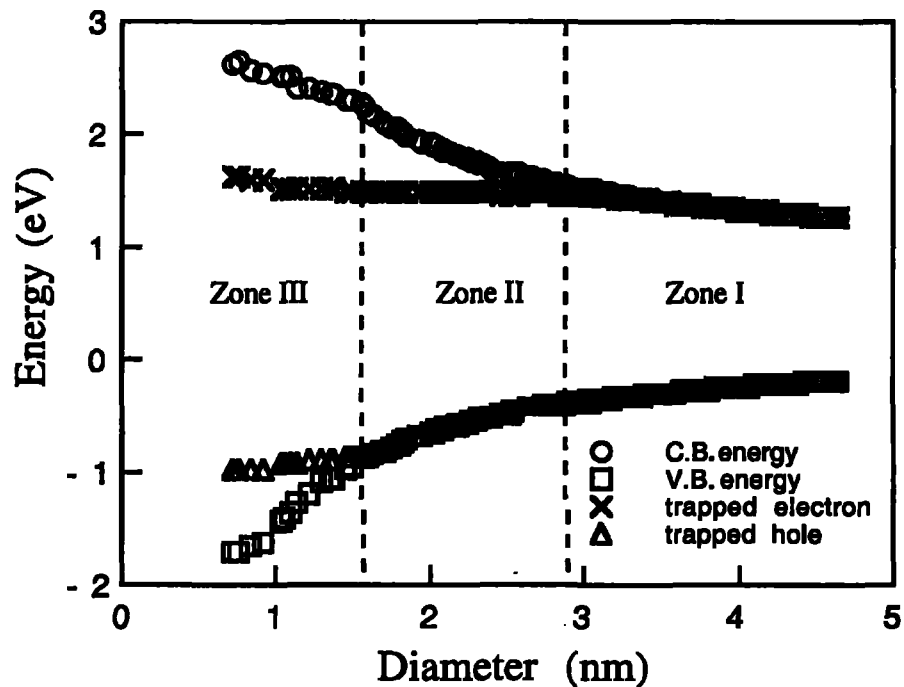


Figure 3: Electronic states in Si nanocrystals as a function of cluster size and surface passivation. The trapped electron state is a p-state localized on the Si atom of the SiO bond and the trapped hole state is a p-state localized on the oxygen atom [12].

ening is a standard feature of all nanocrystalline materials and it has to be considered in all measurements of low-dimensional structures, not only Si nanocrystals.

The last problem, not discussed up to now is influence of matrix material on energy states of a nanocrystal. To study influence of the surrounding material on nanocrystal properties is a difficult task, because it is hard to distinguish contribution from the matrix and from the nanocrystal itself in results. This problem could be overcome using methods with excitation of only one size of nanocrystals by spectrally narrow laser pulse and observation of either luminescence or absorption of a smaller number of nanocrystals. This topic is discussed for example in [11, 14].

## 2.3 Optical properties of semiconductors

Properties of materials containing nanocrystals include not only the energy structure evaluation, but also the interaction of material (semiconductor) and an external electromagnetic field.

The interaction contains various effects like absorption, reflection, scattering and dispersion of light by a material medium. The first effect that appears when radiation reaches the surface of the material is reflection. On the border between two materials of different refraction indexes, part of radiation is reflected.

The direction and the intensity of radiation propagating through the medium changes by interaction of atoms inside the material and present electromagnetic field.

A complete description of interaction is complicated. The interaction between radiation and a matter was examined by Einstein and his theory will be used in this study. This theory neglects nonradiative transitions and atomic energy structure is simplified to two levels (two level system). The theory is more deeply explained for example in [15, 16]; only its basic points will be mentioned in this work.

Energy levels are marked  $E_1$  and  $E_2$ . The number of atoms on each level is  $N_1$  or  $N_2$ , respectively, and  $g_1$ ,  $g_2$  are degenerative parameters of each level. Occupation of each level at thermodynamic equilibrium follows the Boltzmann statistics. For changes in occupation of each energy level, we can write the following equations [15]

$$\frac{dN_1}{dt} = -B_{12}\rho(\nu_{12})N_1 \quad (11)$$

$$\frac{dN_2}{dt} = -B_{21}\rho(\nu_{12})N_2 - AN_2 \quad (12)$$

where A,B are Einstein coefficients of spontaneous and stimulated emission (meaning frequency with which a given atom emits or absorbs photons). The first equation describes absorption of a photon and excitation of an atom at the higher level, and the second equation is a reverse action, emission of a photon with transition of an atom to the lower state. These equations show that at thermodynamic equilibrium, there are more atoms at ground level  $E_1$  than at excited energy level  $E_2$ , which leads to higher absorption than emission. Higher population on excited energy lever (population inversion)

is necessary to achieve optical gain. But the two level system described above is not suitable for amplification, since the emitted photon can be immediately absorbed back. It is important for optical gain to have at least three levels where it is possible to have different excitation and emission energies.

### 2.3.1 Absorption

A perfectly transparent medium permits the passage of a beam of radiation without any change in intensity other than caused by the scattering, divergence or convergence of the beam. Total radiant energy exiting from such a medium equals that which entered it. On the other hand the exiting energy from an absorbing medium is less than that which enters and in the case of highly opaque media exiting energy is reduced practically to zero. However, none of known material is opaque to all wavelengths of the electromagnetic spectrum, which extends from radio waves through visible region to gamma rays. Similarly, no material is transparent to the whole electromagnetic spectrum.

The capacity of absorption depends on a number of factors, including constitution of the medium, thickness of the absorbing layer, state of the medium and wavelength of absorbed radiation as well as radiation polarization. The absorption is described in the Lambert and Beer's law.

Lambert's law expressed the effect of the thickness of the absorbing medium. A homogeneous medium is thought to be constituted from layers of uniform thickness with similar absorption. Absorption of one such layer of infinitesimal width can be expressed as  $\alpha$  and is called absorption coefficient (constant for each material). If  $I$  is the intensity to which wave is attenuated after traversing thickness  $d$ , and  $I_0$  is the intensity of the beam at the surface (no loss by reflection is considered for simplicity), the change of intensity through the material is expressed by the following equation

$$I = I_0 e^{-\alpha d} \quad (13)$$

Beer's law refers to the effect of concentration of the absorbing medium and is mainly used for gases and liquid solutions. The smallest part considered as an element of absorption in this law is each individual molecule. Each molecule absorbs the same fraction of the radiation incident upon it, no matter whether it is closely packed in a concentrated solution or highly dispersed in a dilute solution. The effect of concentration  $c$  and thickness  $d$

on the absorption of a monochromatic radiation gives a simple mathematical expression

$$I = I_0 e^{-k'cd} \quad (14)$$

where  $k'$  is a constant characteristic for a given absorbing substance at constant wavelength and temperature.

### 2.3.2 Optical gain

The condition for achieving population inversion is spontaneous life time large enough so that stimulated emission is more probable than spontaneous emission. This condition can be mathematically expressed by the following expression for optical gain

$$g = \frac{c^2 f(\nu_{12})}{8\pi\tau_{sp}\nu_{12}^2} [N_2 - \frac{g_2}{g_1} N_1] \quad (15)$$

which comes from Einstein's equations (11) and where  $\nu_{12}$  is frequency of incident photon,  $f(\nu_{12})$  is a response function of the system,  $\tau_{sp}$  is lifetime of spontaneous emission and  $c$  is light velocity. This most simple model presents only conditions given at each level. It is important to say that real amplification, like those used for lasers, can be only achieved in systems with more than two levels.

The described calculation of optical gain for atoms can be easily adapted to nanocrystals because of the similarity in energy spectra (levels).

The material with optical gain is a potential active medium of a laser. Semiconductor lasers currently available are mostly constructed from gain media based on bulk materials. Potential advantage of using nanostructures instead of bulk material would be in lower threshold current and lower temperature dependence. The dependence can be expressed in the form [17]

$$J_{th} = J_{th}^0 \exp\left(\frac{T}{T_0}\right) \quad (16)$$

where  $T_0$  is characteristic temperature and  $J_{th}^0$  is a threshold current for temperature 0 °C. The reason of low temperature dependence is linked to the fact that characteristic temperature  $T_0$  depends on dimension of material, for 0D material  $T_0$  tends to infinity.

### 2.3.3 Waveguides

Some samples studied in this thesis contain waveguiding structures. This section will provide a brief introduction in the theory of waveguides that is described in greater detail in various books like [15, 18].

Propagation of light inside a dielectric material could be described by ray optics although the wave and modal description must be used for an exact description. The ray optics is sufficient for basic treatment of waveguides. The plane-wave approach to modal analysis is sufficient for studying those characteristic waves of the planar, perfectly conducting guide that can propagate unattenuated down its length. Additional modes are needed, however, to represent a general electromagnetic disturbance in the guide.

A waveguide can be defined as a structure capable of guiding the flow of electromagnetic energy in a direction parallel to the axis. A radiation field guided by the waveguide could take a form of a superposition of uniform plane waves propagating down the guide, undergoing successive internal reflections at various angles to its axis. Complete analysis of such a guided wave is quite complicated. We therefore look for a more simple set of elementary waves, that may be used to describe the expected state of the wave. These elementary waves, characteristic for a particular waveguide, are called the modes of a waveguide.

A waveguide mode is an electromagnetic wave that propagates along a waveguide with a well-defined parameters like phase velocity and group velocity. The modes are referred to as the "characteristic waves" of the structure because their field vector satisfies the wave equation in all the media of the guide, as well as the boundary conditions at the interfaces. Modes characterize the structure and do not depend on the source of radiation. Each propagating mode in the interior of a dielectric waveguide can be described as a superposition of uniform plane waves propagating at a fixed angle with the axis.

The number of modes is determined by spatial dimensions of the structure and the wavelength of the used light. For simplicity, the number of modes is determined by the ratio between waveguide size (width) and the wavelength. Each structure has critical wavelength that is the longest wavelength that can form a mode inside the structure. Critical wavelength for a dielectric waveguide also depends on difference of refraction index outside and inside the waveguide.

For a guide of finite thickness, we will only have a finite number of such



unattenuated propagating modes. To describe a general field, we will have to add a continuous spatial spectrum of modes corresponding to all real angles smaller than the critical angle in the guide, as well as a continuously distributed set of nonpropagating waves, it means waves that decay in the  $z$  direction away from sources or discontinuities. Characteristic waves that do not satisfy radiation condition fall into a broad class of modes called "improper". The most important of these, originally called "leaky waves", were first described in the microwave literature. As their name implies, some of their power is continuously radiated through the walls of the guide.

In semiconductor materials, a planar dielectric waveguide is often used. This structure contains one material in core of waveguide and another material with lower refraction index as substrate and superstrate. The electromagnetic wave is guided inside the structure with higher refraction index by reflections on borders between environment of different refraction indexes. Another large part of waveguides are structures used for optical communications or in fiber optics. A fiber is a cylindrical structure where profile of core and shell is round - conditions given on values of refraction index of core and shell are similar to the planar waveguide. However, for integration in optoelectronics, for small sizes, planar waveguides are more simple to form and use. More information can be found in monographies on waveguides, for example [18].

The description of propagation reveals basic properties of a waveguide, but one important task was omitted. Intensity of guided light is dependent on efficiency of coupling external source of light into the guiding structure. A large development of optical communications needs also improvement of this efficiency. Coupling can be performed by two methods. One method could be described as adaptation of electromagnetic field to the proper form, able to be guided in a waveguide, the second method is based on use of total reflections. The adaptation of field can be done by a lens or by a direction of incident light. Experiments using adaptation of the angle of coupling with the aim to use the desired mode in the waveguiding structure are also presented in [18]. Frustrated total reflection [18] is a coupling method developed in 1947. One possible realization contains a prism on surface of material and a gap of low refraction index between prism and material.

## 2.4 Photonic crystals

The optical analogue of a normal crystal is the photonic crystal where photons are constrained to propagate within dielectric lattice like electrons propagate through a periodic change of potential. Hence the theory of nanocrystals and quantum confinement from the electronic point of view has its optical analogue in optical region. Photons can be confined in one, two or three dimensions [9, 1] similarly to the nanomaterials discussed above. Quantum well is similar to planar optical waveguide, 2D quantum confined structure (quantum wire) is similar to the optical fiber and 0D structure (nanocrystal) is similar to the microsphere optical cavity, elemental part of a photonic crystal.

Photonic crystals represent a class of nanomaterials containing ordered structures of periodically changing refraction index on the scale of a light wavelength. In a photonic crystal, for a certain energy of a photon and a certain wave vector (direction of propagation), a photon cannot propagate through the crystal [19, 20]. The photon generated inside cannot propagate in this direction and light from outside the material is reflected. The contrast of refraction index of beads and interstices predicts the quality of the band gap.

In case of silica beads and voids of air, refraction index is not high enough to develop the real band gap in all directions. Preparation of sub-micron beads from material with high refraction index is difficult, hence inverse opal structure was prepared. The advantage of the inverse opal consist in full band gap. Voids are filled with material of high refractive index and beads are removed. Templates for preparing inverse opal are usually either polystyren or silica beads. Such beads are later removed. The polystyren is burnt out and silica beads are etched by HF acid.

The band structure of the photonic crystal determines the optical properties like transmission, reflection and their angular dependence. Therefore, the determination of the structure is a subject of interest for many laboratories. The theory of a photonic crystal is presented in various books [20]. An exciting fact of a photonic band gap structure is that it can be evaluated from the first principles and the results are consistent with experiment. Many methods for a photonic band gap determination were proposed and all can be divided into two main groups: frequency domain and time domain description [20]. In frequency domain techniques, the Transfer Matrix Method should be mentioned. Calculations are based on the transmission and reflec-

tion coefficients and band structure for electromagnetic waves by using the transfer matrix of the system. The band structure is calculated by diagonalization of the transfer matrix. This method can be sufficient for propagation of electromagnetic modes through a finite photonic crystal, but is limited to lower frequencies. The Finite-Difference Time Domain method is an example of the second group and is based on calculation of time evolution of the electromagnetic waves by direct discretization of Maxwell's equations. The advantage of this method is that results for a large frequency range can be obtained very quickly. This method is also suitable for calculations of transmission and reflection coefficient as well as for simulation of a wave packet propagation.

The analogy between electronics and photonics can be exploited by using the concept of doping photonic crystal. Acceptor or donor impurities in semiconductor introduce impurity states in the band gap. The same can be done in a photonic crystal by breaking symmetry of the dielectric function either by removing or by adding a constituent. This defect is spatially localized, so the photon has the allowed frequency in the band gap through which photon can propagate. The structure is called micro-cavity, and important property of this structure is directionality of emitted light.

### 3 Semiconductor nanocrystalline materials

Properties of a nanocrystal differ with respect to the substrate material and form of a nanocrystal. Combination of the shape of a nanocrystal, its surroundings and its size gives a number of completely different samples even if the same elements are used for preparation. Different spectra are obtained also from samples with various positions of nanocrystals inside the material (in a layer, whole volume, etc.). Even material containing nanocrystals of identical size and composition could behave differently due to the fact that in one case, nanocrystals form a layer on the surface, and in the other case they are embedded inside the matrix material.

Nanocrystals on the surface could be prepared in high density and usually there is no matrix material between them. Such material can be studied by direct observation in contrast to nanocrystals embedded inside the matrix material. Properties of nanocrystals of high density are more easily studied due to the fact that large concentration of nanocrystals presents larger changes in behavior in comparison to bulk properties.

Nanocrystals embedded inside the matrix material are usually more separated one from another. Each nanocrystal is surrounded by a matrix material, and on interface of those two materials, different surface energy states are formed. These states are the reason why the same nanocrystal (same size, material) has different properties when on surface and when embedded inside the material. Concentration of nanocrystals is correlated with mean distance between nanocrystals, so we can prepare sufficient sample to study one single nanocrystal.

These changes of nanocrystal properties and their control are topic of this section. At first, preparation methods of nanocrystals will be explained, followed by a detailed description of materials studied in our laboratory.

#### 3.1 Preparation methods

There are many methods of preparing nanocrystals. For easier description, it is convenient to group methods by a common part of preparation or for example by the similar form of prepared material. Selection criteria can be for example: state of matter used for preparation (gas, liquid or solid state) or temperature of preparation (high and low temperature of preparation) [21]. Preparation techniques may be also grouped according to the direction of formation: (i) bottom-up techniques - growth of nanocrystals from

atomic and/or molecular constituents (precursors), (ii) top-down techniques - dividing bulk material into small parts.

Due to the different properties of nanocrystals on the surface or embedded inside the substrate, preparation methods in this thesis will be divided according to the resulting form of sample into methods forming a layer of nanocrystals on the surface and methods preparing nanocrystals inside the matrix.

### 3.1.1 Nanocrystalline layer on the surface

Methods for preparation of a thin layer of material on the surface have been studied for a long time. Very thin layers can possess different properties in comparison to the bulk material and this property has been widely examined for example in electronics. Advanced development of these methods gives the possibility to utilize this knowledge also for preparation of nanocrystals.

The first described method is important for its simplicity and low costs, that allows nearly every laboratory to prepare own samples. It is precipitation of semiconductors from liquid precursors in solution. The preparation has two steps: growth of the nanocrystals from the precursor and the second phase is formation of a solid material from the nanocrystals in liquid. According to the concentration and temperature of the precursors the nanocrystals of a specific size are formed. Solid samples can be prepared from solution using various methods, e.g. the sol-gel method and deposition of layers by the dip- and spin-coating. Dip coating forms solid layers on substrate repeatedly dipped into the suspension which is attached on the surface due to cohesive and viscous forces. Spin coating uses a rotating plate (substrate) on which suspension is poured. Due to the centrifugal forces, solution flows radially outwards and covers the substrate with a uniform layer. The spin- and dip-coating techniques may be applied to form layers of nanocrystals from their colloidal suspensions.

A method used mainly for preparation thin films of III-V and II-VI semiconductors is chemical vapor deposition (CVD). This basic name can be extended with another more precise specifications: metalorganic chemical vapor deposition (MOCVD), plasma enhance chemical vapor deposition (PECVD) etc.. The chemical vapor of precursors is directed to a heated substrate in the reaction chamber where the desired semiconductor material is formed. One modification of this method, called Stransky-Krastanov growth, can produce nanocrystals by deposition a very thin layer of semiconductor which collapses

due to strain into small nanocrystalline islands. These techniques are potentially dangerous as they often use poisonous gases. Even if this method is expensive, it is available commercially and used in many laboratories.

Fabrication of complex structures in microelectronics is based on lithography. This technology has many variants with different sources of radiation used for writing structures into the resist: electron-beam lithography, X-ray lithography or optical lithography. For example electron-beam lithography was used for preparation of quantum dots (QD) [21, 22]. The most common lithography employs irradiation of samples with light through a mask. Irradiated (or non-irradiated) parts of the surface are removed and the desired pattern is etched into the substrate. Wavelength of the applied light is a limiting factor determining the size of minimal features (diffraction limited resolution). Therefore, advanced methods like electron beam lithography must be used to achieve nanometer resolution.

The etching may be performed by a beam of ions or by a chemical reaction on the surface of the material. The electrochemical etching without lithographical mask used to prepare the so called porous silicon [23] - the first and the most popular nanocrystalline silicon material. This method was used for preparation of our samples and will be described in separate section (Sec. 3.2.1).

Lithography and etching methods are also suitable for the fabrication of two dimensional photonic crystals. A planar pattern on surface can be written for example by the e-beam lithography.

### **3.1.2 Nanocrystals embedded inside a matrix**

Nanocrystals embedded inside the host matrix are formed mainly from a solution. To incorporate nanocrystals inside the host matrix in solid form is more difficult and needs a specialized equipment. Samples presented in this section are more stable, because nanocrystals are not in direct contact with the surrounding ambient and may be well passivated.

Precipitation from solution is one of the oldest methods of preparing nanocrystals. The original methods do not produce a thin layer, as in the method described above, but produce thick solid samples. Materials using special nanocrystal properties without understanding them had been used a long time before the discovery of nanocrystal existence. Namely in color glasses that contain different numbers and sizes of nanocrystals causing filtration of light. Such materials are prepared by precipitation from melted glass.

Popular nanocrystal materials prepared in this way are CdS and CdSe. The size of prepared nanoparticles can be controlled in three ways - duration and temperature of annealing and concentration of reactants. Optimal grain size and uniformity was achieved with the lowest concentration demonstrating important role of kinetics in this method of preparation.

Semiconductor concentration plays a major role in size dispersion of quantum dots in glass. Lower dopant concentration leads to larger quantum dot sizes with less dispersion. Dispersion could be decreased also by double annealing of the glass, separated nucleation and growth regime. Such effect was presented in [21]: single annealing reached size dispersion of 10.5% but double annealing resulted in a 3% distribution.

Another method in this section is ion implantation, method that incorporates impurity material into a solid matrix. In semiconductor technology, this method has recently almost completely replaced chemical doping. During implantation, source material of impurity atoms is vaporized (ionized) and ions are then accelerated and directed on the desired substrate. The most important parameter of implantation is kinetic energy of accelerated ions and total dose. As the implanted ions enter the matrix material, their kinetic energy decreases by collisions of host material atoms until it finally stops at a certain depth. The stopping power is function of implantation energy and property of matrix material. This method was also used for preparation of samples described in this work and will be the subject of the following sections.

## **3.2 Studied materials**

Nanocrystals we use are all based on the most popular semiconductor material, silicon. Reasons for choosing this material were discussed above, we would only like to emphasise its high reserve in nature and well developed technology for its industrial production. Among various forms of Si nanocrystals [24, 11, 21], we study three of them: nanocrystals implanted in silica glass, nanocrystals in artificial opals and colloids of porous silicon. Each form is discussed in a separate paragraph.

### **3.2.1 Porous silicon and its colloids**

Material called porous silicon was the first presented form of silicon nanostructure emitting visible light [2]. The porous silicon used in this study

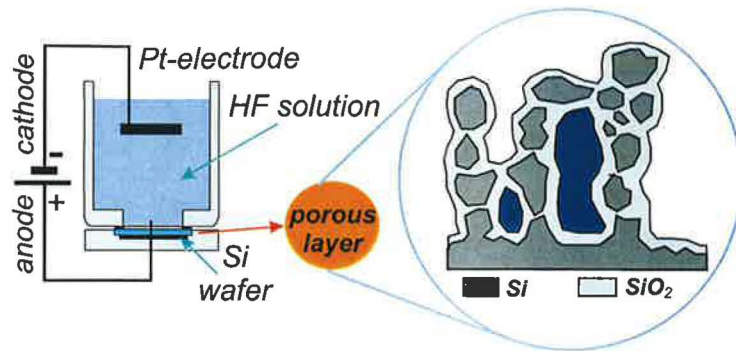


Figure 4: Schematic illustration of the porous silicon preparation.

was prepared in the Institute of Physics, Academy of Science of the Czech Republic [1].

Preparation can be simply described as an electrochemical reaction on the Si surface in an HF solution in electric field [1, 23]. The preparation schema is presented in Fig. 4.

Several conditions for porous silicon formation should be fulfilled. The first parameter that must be controlled is electrical potential given on the sample. Polarization of applied potential have to be anodic - holes flow from the source material into an electrolyte. Under use of cathodic polarization, no dissolution of Si surface could be observed. Proper value of potential is important, at high potential the Si surface is polished instead of making porous material. The current value on the border between polishing and porous Si formation, called electropolishing peak, depends mainly on substrate resistivity and HF concentration.

The exact dissolution chemistry of Si is still under investigation, and different mechanisms have been proposed. However, it is generally accepted that holes are required for electropolishing as well as for pore formation. During pore formation, two H atoms evolve for every Si atom dissolved. The H evolution disappears when the process enters the electropolishing regime, because current efficiencies are about two electrons per one dissolved Si atom in the pore formation regime and about four electrons during electropolishing - see following equations [1].



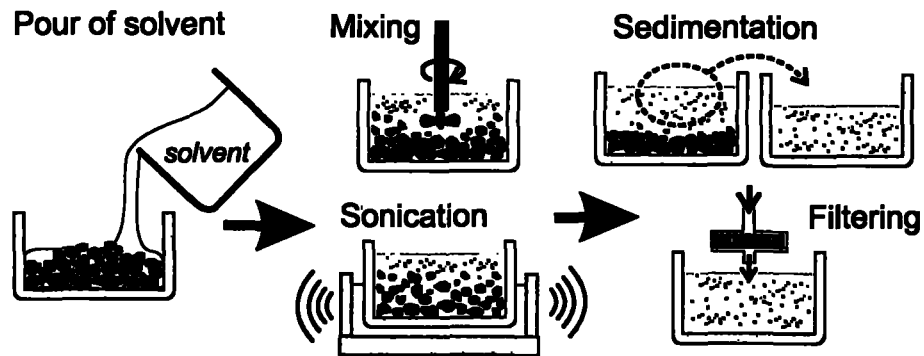


Figure 5: Schematic illustration of the preparation of colloidal suspensions from the porous silicon powder.

pore formation



electropolishing



The aqueous solution used for etching does not contain only HF and water. HF is dissolved in water with ethanol to increase wettability of the porous silicon surface and to improve the uniformity of the porous silicon layer in depth. The pure aqueous solution forms bubbles and sticks them on the Si surface. Bubbles are removed in solution with contents of ethanol.

Drying of porous silicon layers is the crucial step especially for material with high porosity. Different methods have been developed to reduce or eliminate the capillary stress. In this study, reduction of this effect is not needed because we use porous silicon as powder removed from a substrate silicon.

Preparation method of colloid is presented in Fig. 5. Colloids were prepared by pouring an organic solvent onto porous silicon powder and mixing it with a small propeller or in ultrasonic bath. As the prepared powder contains grains with size of even tens  $\mu\text{m}$ , mixing decreases size of the biggest particles but is inefficient on particles smaller than  $\mu\text{m}$  size. Further size selection is possible by using repeated sedimentation or centrifugation. It

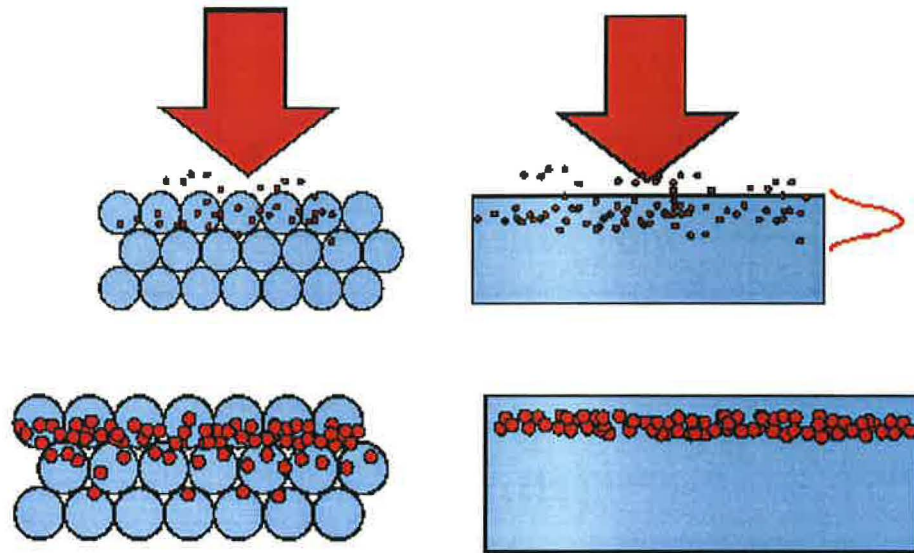


Figure 6: Scheme of implantation method where material is implanted with  $\text{Si}^+$  ions. Material can be silica glass (right) or artificial opal (left). After implantation, samples are annealed to form nanocrystals shown as larger red circles in the lower pictures.

is also possible to filter suspension by a membrane with pores hundreds nm big.

The suspension can be then deposited on a cleaned surface by spin- or dip-coating method. Proper combination of substrate and solvent could form interesting self-organized structure.

### 3.2.2 Nanocrystals implanted in silica glass

More stable material than porous silicon can be obtained by embedding nanocrystals into the  $\text{SiO}_2$  matrix [31]. Implantation is a technology largely used in electronics, so its use for nanocrystals preparation is a step toward nanocrystals incorporated into standard electronic circuits. (CMOS compatible technology)

The most important material for our work is silica glass implanted with Si nanocrystals. This type of material is presently studied in many groups

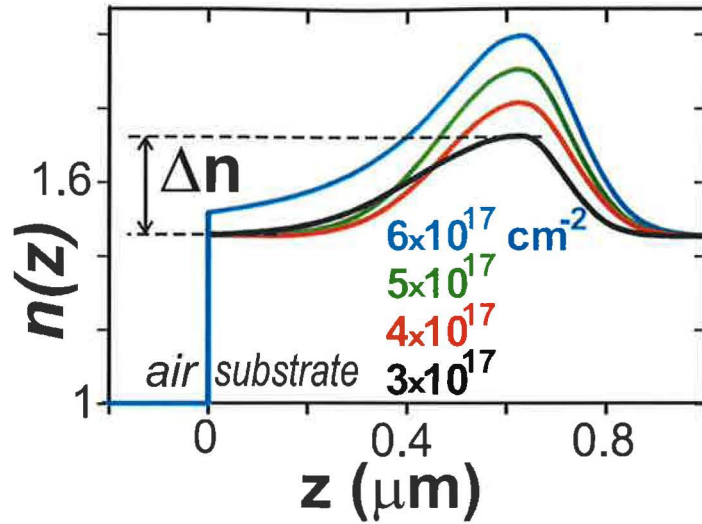


Figure 7: Profile of the refractive index for implantation doses from  $3 \times 10^{17} \text{ cm}^{-2}$  up to  $6 \times 10^{17} \text{ cm}^{-2}$

[25, 26, 27, 28]. Our samples are prepared in cooperation with the Australian National University of Canberra - Laboratory of Prof. Elliman. This laboratory has wide experience with preparation of such implanted samples [29, 30].

The advantage of silicon ion implantation consist in a good control of the size, depth profile and concentration of silicon nanocrystals. Preparation can be divided into three steps. At first the implantation increases concentration of Si ions in implanted material, annealing then forms nanocrystals and the final step is enhancing luminescence of the formed nanocrystals.

The implantation is performed in a high vacuum chamber. Silica glass is implanted by  $\text{Si}^+$  ions with desired implantation dose (see Fig. 6). Higher doses imply formation of bigger nanocrystals. Energy of implantation determines the refractive index profile and depth of implanted nanocrystals under the surface which have to remain constant during the whole implantation lasting for several hours.

The second step is annealing. Samples are annealed for 1 hour at high temperature ( $1100 \text{ }^\circ\text{C}$ ) in an  $\text{N}_2$  ambient. In this step, nanocrystals are formed from implanted ions. Excess concentration linked to time of annealing determines nanocrystal size.

The last step is passivation of surface which is done in forming gas ( $N_2/H_2$ ) under temperature of  $500^\circ C$  for one hour. This step is important to improve passivation of surface effects. Influence of passivation on stability of prepared materials was confirmed for example by [30], where authors proposed that interface trap density can be reduced by annealing in forming gas.

The smallest observed size of Si nanocrystal prepared by implantation was 2.5 nm [31], which indicates existence of minimal excess Si concentration necessary for nanocrystal formation. Concentration should be of a few atomic percent, requiring implantation doses in the range of  $10^{17} cm^{-2}$ .

The depth of nanocrystals implanted in a material depends on implantation energy and on properties of the implanted material. The higher implantation (energy), the deeper nanocrystals are buried in the material. Implantation intensity held constant for the whole implantation time forms a layer of implanted material at a certain depth. Hence materials prepared and studied in this work contain a layer of nanocrystals in a specific depth according to the implantation energy.

The refraction index of nanocrystals is higher than that of a matrix material and hence the mean refraction index is proportional to the concentration of nanocrystals (Fig. 7). The layer of buried nanocrystals forms an asymmetric planar waveguide. A material prepared by implantation contains density of nanocrystals varying with depth under the surface. Maximal concentration is at the depth specified according to implantation conditions. Depth of each nanocrystal follows the asymmetric Gaussian distribution and therefore structure formed by nanocrystals is a gradient waveguide. The profile of refraction index depends on implantation energy, fluency and also annealing conditions. All these conditions are difficult to keep when using different equipment. Therefore a preparation of identical samples, or samples with desired conditions is quite difficult.

Connecting the depth distribution of nanocrystals with refraction index value leads to an explanation of the implanted layer property. Spatial restriction of waveguide is only in one direction and two remaining directions are limited only by the size of a sample. What is more important is that structure buried near the surface has two different boundary conditions (see Fig. 7). On the surface, there is jump in refraction index from glass (also with few nanocrystals possibly inside) to air. Interface inside the sample has no such sharp change and this side is more similar to gradient waveguide where core slowly changes to shell.

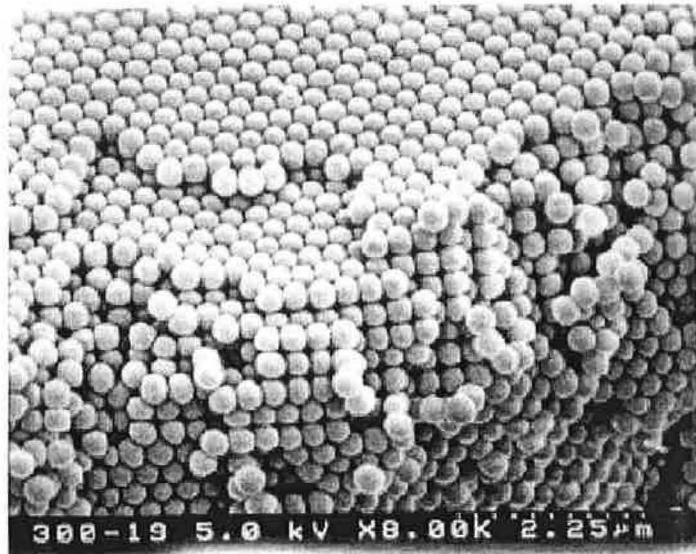


Figure 8: SEM image of typical boundaries of the cleaved facets in the  $\text{SiO}_2$  opal. [35]

### 3.2.3 Artificial opals

Artificial opals were named after natural gemstone with similar micro-structure. Silica opal has relatively low contrast of refraction index to form real photonic gap. However, preparation of an inverse structure with interstitials filled with semiconductor or beads composed of semiconductor gives us refraction index contrast high enough to observe photonic gap.

The 3D photonic structure was first prepared in 1987 by two groups in the United States [32, 33]. To grow photonic crystal, the ion beam technology was used. The structure formed in this method contains a photonic band gap at  $1.55 \mu\text{m}$  (important telecommunication wavelength).

There are several methods of photonic structures preparation, for example gravity sedimentation or chemical synthesis with particles self organized into silica beads of sizes ranging between 100 and 700 nm [34].

Gravity sedimentation is a process where particles, suspended in solution, settle to the bottom of the receiver, as solvent evaporates. The critical point is finding the proper conditions for liquid evaporation so that parti-

cles form a periodic lattice. The size of crystallites depends on duration of crystallization, temperature, humidity, source solvent properties and others.

In this thesis, preparation from solution will be described. The process started with solution in electric field. Sedimentation was controlled by field of order 0.1 V/cm present in between a platinum grid and a mercury layer. The sedimentation took several days. Self supporting opals were formed by partial sintering of the silica particles at temperature of approximately 900 °C for about 2 hours. Silica balls formed by this process were of size around 300 nm with size dispersion better than 2%.

Another possible method is a sample prepared by hydrolysis and condensation of tetraethoxysilane in a mixture of water, ammonia and ethanol. The result of this method is presented in Fig. 8 [35]. This figure also illustrates low size distribution of opal beads; in this experiment, standard deviation of size distribution was lower than 5%.

We should also describe another material similar to artificial opals, called inverted opals. Inverted opals are prepared usually from solution. In which an artificial structure of beads (similar to opals) serve as template for the final structure. This structure is later removed (for example by chemical way) and the studied material is only in places where spaces between individual beads were [36, 37].

Even more interesting is filling voids with material emitting light. The first experiment with light emitting material embedded inside opals and having bigger refraction index contrast was carried out 10 years ago [38]. In that experiment laser dye was used as a light source inside the artificial opal, matrix material contained approximately 200 nm big silica beads.

Samples used in this study contain Si ions implanted into the opals [39, 40]. The aim is to incorporate a nanocrystal as a source of light inside an opal sphere. Preparation is similar to the implantation of silica glasses with Si ions (section 3.2.2). The annealing needs more control compared to the implantation of silica glass, because high temperature of annealing could destroy the photonic structure. Alternatively the Si nanocrystals were introduced into opal voids by impregnating porous silicon suspensions into an artificial opal [V].

Our opal samples are prepared by the Group of Inorganic Chemistry (GMI), Institute of Physics and Chemistry of Materials, Strasbourg, France. Implantation is again performed on Australian National University in Canberra. The samples are fragile and handling it is difficult.

## 4 Experimental techniques

In the following sections, differences between experimental methods to observe nanocrystals on the surface of the sample and those embedded inside the sample will be described. What is similar for both of them is change of energy spectra due to the size of nanocrystals described in the theoretical section.

Up to now, most attention was paid to effects relating to the size of nanocrystals, so it might seem that preparation method forms material with nanocrystals of definite size. However, in a real sample, sizes of nanocrystals are distributed with certain probability around the mean size. This size distribution is an important criterion providing information about the quality of the prepared sample. The experimental method must consider this fact and, when we would like to study basic property of a certain size of nanocrystals, we have to try to eliminate this broadening.

In the following sections, experimental methods are divided into groups. Optical methods are the most important for us because we are interested in optical properties of materials with their potential use as a source of radiation. However, optical methods could not give us all information about the studied material. Additional information about morphology of the sample could reveal facts important for proper evaluation of data obtained from optical measurements. Methods described in the following sections are mainly those used to study three types of materials discussed in this thesis, complemented with several methods used for similar materials or specially developed for nanocrystals investigation.

### 4.1 Size and morphology determination

The following sections will provide basic information on methods usable for the morphology characterization, distribution of sizes, mean size, density of nanocrystals and their shape in samples studied in this thesis. An introduction into the method used for similar samples in other laboratories will be also given.

**Scanning electron microscopy** Nanocrystals and other particles of size smaller than  $\mu\text{m}$  could not be observed directly by using standard optical microscopes. Scanning electron microscopy (SEM) is a method using interaction of an electron and an atom to visualize the surface of the sample

[20].

The maximum resolution of optical methods is about half of used wavelength, so for visible light it is not less than 200 nm, which is too rough for observation of nanocrystals of several nm size. Objects of such small sizes could be visualized only by methods based on radiation with much smaller wavelengths. Electron microscopes use electrons at energies of a few thousand electron Volt (eV), which is not comparable with optical photons with energy up to 3 eV. According to de Broglie equation, wavelength of such high energy particles is at the range of 0.01 nm. Although real resolution that could be achieved is only in the range of 0.1 nm, it is a great advance against an optical microscope.

SEM is a technique used to obtain an image of the sample by scanning of an electron beam over the surface of a specially prepared sample (especially non-conducting samples need special treatment). The electron beam is focused on an area usually 10-20 nm in diameter, which is a real resolution value. The beam is scanned over the sample (similar to the television) and stays on each point for a period of time determined by the scan speed. There are several types of effects that could be used to form SEM image, for example: back-scattered electrons, secondary electrons, low energy X-rays.

**Raman spectroscopy** Nanocrystals inside the matrix are even more difficult to observe. For example, it is not possible to use the SEM method described above. Raman spectroscopy is one of the possible nondestructive methods for such samples [42, 43, 44].

The Raman spectra were discovered in 1928 in sunlight scattered by a liquid. By using complementary filters, it was found out that frequencies present in scattered light are lower than in filtered light. Later experiments were performed with spectrally narrow laser pulses. In the spectra observed, there was not only excitation wavelength, but also new frequencies characteristic for the studied material.

The mechanism of the Raman effect is based on collision of a photon passing through a material with an atom or a molecule. If collision is elastic, the photon bounces off the molecules with unchanged energy and momentum, and hence with unchanged frequency - Rayleigh scattering. On the other hand, an inelastic collision of a photon causes change in its energy and momentum. New frequency of the photon is determined according to the rotation and vibrational energy state of an interacting molecule or atom. The



frequency shift corresponding to the vibrational or rotational states contains two parts, Stokes and anti Stokes line. The Raman spectra measurement detects such changes. Experiments are described in many works, for example [16]. Excitation by highly monochromatic light from a laser impacts on a sample in an appropriate transparent cell and scattered radiation is then detected and analyzed.

This method can reveal size distribution of nanocrystals inside material according to the change of Raman spectra detected from a given sample (change of shape and position of the Raman peaks [42]). The article [43] theoretically models changes of Raman spectra according to the Si sphere size. The model consider two types of particles columns and beads. Equations in this article allow to determine size of nanocrystals from the detected Raman spectra.

**Infrared spectroscopy** Infrared spectroscopy studies interaction of materials with radiation in the infrared region of the spectrum. The infrared region is valuable for the study of material structure because energy of vibrations of atoms in molecules and crystals falls in the infrared range. The infrared spectroscopy is often used for characterization of molecules, because the infrared absorption spectrum is highly characteristic and could be used as a molecular fingerprint.

But our samples are mostly composed of amorphous silica glass and the classical infrared spectroscopy gives little information. Instead we measured near infrared transmission spectra in which clear interference fringes are presented that are used to calculate refraction index profile of the implanted layers. The profile is supposed to have a double Gaussian shape and its parameters are obtained by optimizing the numerical fit of experimental spectra presented in Fig. 7.

**X-ray scattering** A recent article [45] describes use of X-ray photoelectron spectroscopy (XPS) on samples containing a layer of nanocrystals (similar to our samples). XPS gives data about bonds and coordination on surface of the sample. The authors support this method with an Ar ion sputtering that allows also probing the bulk, but at the expense of destruction of the sample. So, this method could be used in case we are able repeatedly prepare identical samples so that we can afford destroying one of them.

## 4.2 Optical transitions

This study is focused on optical properties, so this section contains most of the used experimental equipment.

Set-ups used for experiments are mainly home made. The advantage of own equipment consist in the fact that it is prepared with respect to special needs of each measurement. Measurements done using devices described in this section contain luminescence measurement and luminescence angular dependences.

Excitation sources used for our measurements were three powerful lasers: Ar-ion, Nd:YAG and excimer XeCl laser.

Ar-ion laser is a gas laser based on ionized Ar emission lines. Ar ion emission spectra contain a number of lines useful for lasing, and our laser (Coherent Innova 250) was tunable on each of the line quite simply. The maximum emission power is in the range of several W. In our experiments, mainly the line 458 nm was used.

The Nd:YAG laser (EKSPLA NL 303) is a solid state pulsed laser with fundamental emission wavelength at 1064 nm. The laser used in the following experiments is complemented with an Optical Parametric Oscillator (OPO) PG 122 that enables tuning of emission wavelength quasi continuously (step 0.1 nm) in range from ultra violet (UV) up to near infrared (NIR).

The excimer laser is based on transitions in excited molecules of rare gases. Our laser works with XeCl and its pulse duration is 30 ns at emission wavelength 308 nm. The laser could be complemented with a dye laser to change the emission wavelength. However, no dye laser was used for the described experiments.

As the excitation laser light is relatively very strong compared to studied signals, reflection or scattering of an excitation laser beam should be blocked to prevent its detection on sensitive detectors. Spatially, it is provided by detecting the signal from different angle than the incident and reflected laser beam propagates. Spectral filtering is performed by edge filters in detection part that removes the spectral part containing laser emission wavelength.

Luminescence study can give us basic knowledge about energy levels that are involved in radiative transitions. More information on energy structure can be obtained only by a combination of luminescence measurement with other methods like absorption, luminescence excitation, Raman spectroscopy etc.. Some of them we applied for investigation of our silicon nanostructures.

#### 4.2.1 Luminescence measurement

Standard luminescence set-up consists of an excitation source, detection optics and a detector. Luminescence measurement was excited by a continuous wave Ar-ion laser on wavelength from 458 nm to 514 nm. Variations of basic luminescence measurement include time resolved measurement, photoluminescence excitation and several others.

Simple luminescence measurement was performed on colloids of porous silicon either deposited on a substrate or observed as a liquid in a cuvette. The signal spatial distribution does not contain any preferred direction, so detection with high numeric aperture could give a higher signal to noise ratio. There are no such effects like those, observed in waveguiding samples, where detection with high aperture could mix various modes and cause difficulties in results interpretation.

The sample excitation at one wavelength could bring a lot of information about energy levels in a material. However, for different excitation energies, different levels could come into effect. Measurement of the change in luminescence spectra, according to the excitation wavelength, is called photoluminescence excitation (PLE). The source used for this measurement should enable variation of an excitation wavelength without any other changes. This can be done either by a source with broad spectra filtered with interference filters or monochromator (one for each used wavelength), or by a tunable laser.

Luminescence excited by a pulsed source must be detected in specific time after the excitation source is switched off. Time-resolved measurement could be realized for example by using fast photodiode array or a fast CCD device that could measure processes down to several ns. Faster processes need special high-speed detection system, for example streak camera. Luminescence decay depends on the studied material (its energy levels properties) and could be expressed by an exponential function of time, in the simplest case. But often it is necessary to use a more complicated fit with at least two exponentials. Firstly for porous silicon and later for other materials containing nanocrystals, decay line shape is recognized as a stretched exponential [31, 1].

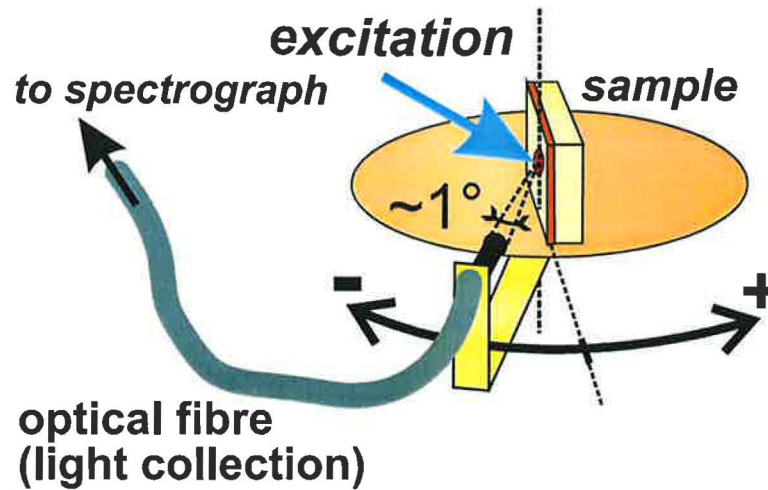


Figure 9: Scheme of angular PL measurement. A blue laser beam is used for excitation. The detection fiber is attached to the moving part of a goniometer and the detection collection angle is  $1^\circ$ .

#### 4.2.2 Spatial distribution of luminescence

The first luminescence measurements of the implanted samples reveal different spectral shape detected from the edge and those detected from the plane of the sample [46]. A special experimental set-up was prepared for those measurements to detect angular dependence of luminescence spectra that could lead to better understanding of the observed effect.

The set-up for angular measurement is based on a rotating part with attached detection fiber. The detection fiber was approximately 5 cm from the sample with detecting angle  $1^\circ$ . The scheme of experimental arrangement is in Fig. 9. For polarization measurement, the analyzer was placed between the sample and the detection fiber.

The first experiment was done by modifying a commercial goniometer, without its original optical part, see Fig. 10 (upper part). This figure shows angular arrangement with excitation by an optical fiber (bottom part). The edge of the sample from which we detect the signal is at the axis of the goniometer. In this setting, scale determines the detection angle.

For basic angular measurement, such goniometer was sufficient. How-

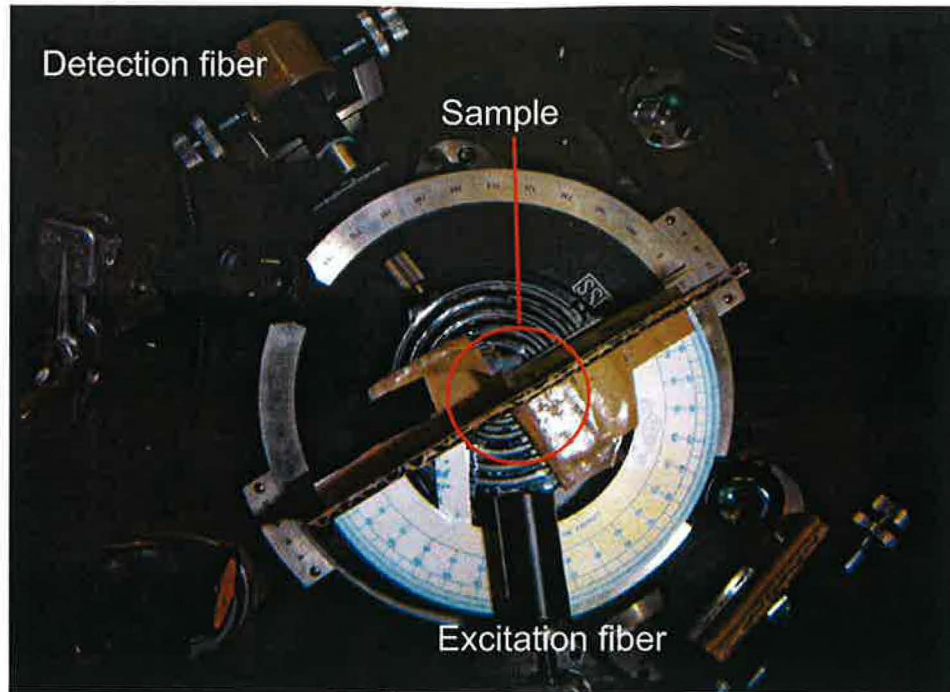


Figure 10: The first set-up for angular PL measurements, using an excitation beam sent through optical fiber.

ever, future needs reveal several disadvantages, for example problems with fixing the sample. To overcome such problems, a new arrangement was designed. This task was done by using a new arrangement, completely composed of components of the Lithuanian Standa company, specializing in opto-mechanical components. The goniometer was smaller than the previous one and gave us more freedom in performing all the desired arrangements as well as in improving repeatability.

The whole angular set-up was placed inside a black box in order to decrease background signal. Laser excitation was provided to the sample through an aperture in one of the walls. As an excitation source, continuous Ar-ion laser at wavelength 458 nm with output intensity on this wavelength up to 1 W was used. A beam focused on a spot of size less than 1 mm in diameter was directed on the sample. The sample was situated perpendicularly

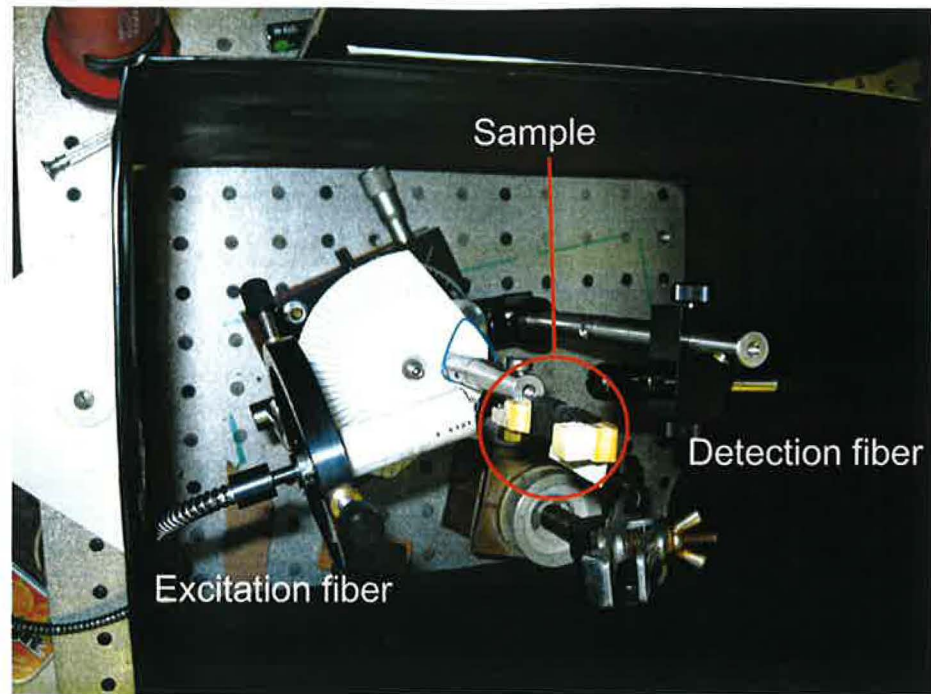


Figure 11: Second set-up for angular measurements, with an excitation fiber.

to the excitation beam. To enable measurement of the whole angular range and to prevent reflection of excitation to the detection part, excitation was not horizontal, but coming under an angle approximately 10 degrees descending. The angle is small enough to neglect its influence during measurement evaluation.

The new goniometer construction started with the aim to easier fasten the sample into the holder and to control its position against detection. Although this goniometer has also some disadvantages, it is a great advance in comfort and possibilities of measurement. The basic part is of course the rotation stage with angle control of detected signal in respect to the orientation of the sample. The detection fiber was fastened on this micrometer-screw moving wheel and holding of the sample was built in the center of this circle. Fastening of the sample enables us to excite and detect the signal in a wide range of angles and also to move the sample in vertical direction. This direction



is important for measurement of regions with different implantation doses without changing arrangement of the set-up. A picture of this goniometer is in Fig. 11. On the left side of the figure, there is the excitation source with its scale. The excitation fiber ends by a shield with pinhole to obtain a small and low divergence excitation source. No sample is present, but it is normally fastened at the center of the picture. In the right part of the picture, there is the end of the detection fiber connected to scale for determination of the detection angle.

The angular set-up was also used for absorption measurement with the source of white light used instead of the excitation laser. The first experiments with excitation light guided via an optical fiber are also on Fig. 10, the excitation part is in the lower section of the picture. In the following measurements, the excitation fiber was mounted on a rotating part, with the axis of rotation above the second edge of the sample. The angle was determined on a scale fastened to the sample holder with center arranged at the excited edge of a sample.

For subsequent absorption measurement, the second goniometer was modified. An external light was guided through an optical fiber and at the end near the sample, there was a collimator. The collimator was approximately 1 cm in diameter and this part was connected to the set-up in a way to enable moving and fixing the whole mechanism to prevent movement of excitation against the sample and detection parts. A scale of excitation angle was connected with the sample holder.

#### **4.2.3 Light coupling into a sample**

An idea to measure guiding properties comes from the fact that luminescence excited in one part of the sample is guided and then exits the sample at some angles. The aim is to couple white light into the sample to observe exiting signal and compare it with luminescence spectra. A similar experiment was carried out three years ago by the group of R.G. Elliman [47], but with a sample implanted with lower implantation dose than the samples presented in our work.

The excitation of desired mode inside the sample could be achieved without any coupling element, only by setting a proper angle of excitation and a proper wavelength. An experiment describing angular dependence of the excited mode could be found for example in [18], where an experiment with coupling light under different excitation angles is described.

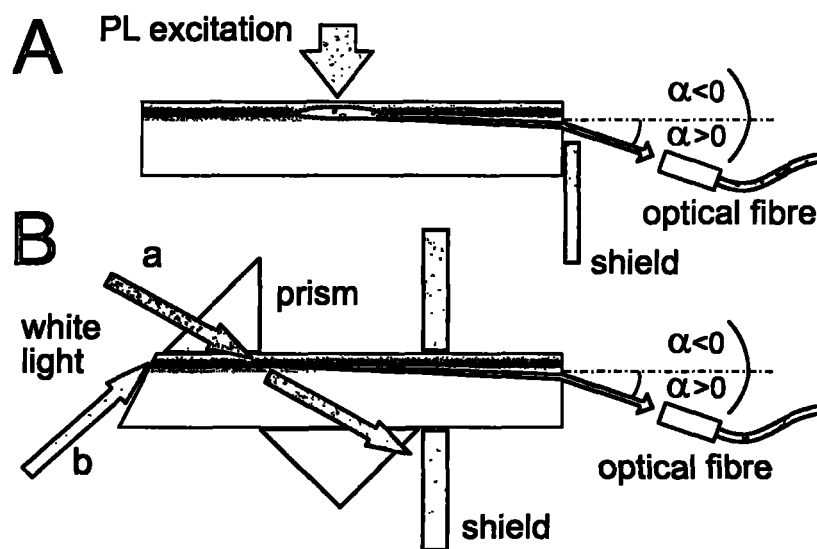


Figure 12: (A) Scheme of the luminescence measurement and (B) two ways of coupling light into the sample - through the prism (a) and by direct coupling (b).

Two different settings were prepared for experiments. The first was coupling of light using a prism on the surface of the sample, which is similar to setting in [47]. The second setting was direct coupling of light through a truncated edge of the sample. One part of the set-up for this measurement has already been discussed in angular measurement set-up description (direct coupling) and the rest will be described in the following paragraphs separately for each measurement. Fig. 12B shows the scheme of settings used for coupling light into the sample and its angular resolved detection. The left side of the image shows excitation part and detection part is on the right side. The shield near the center of the sample prevents detecting signal directly from the excitation source.

**Prism coupling** The first experiment with light coupling was performed by using a continuous excitation source, either Xe or halogen lamp. Both sources emit white spectrum, but with a different spectral profile. The signal was guided through a pin hole and a lens with long focus to decrease



divergence of the excitation beam. A quartz prism coupled low divergence beam into the sample. Good optical contact between the prism and the sample provided immerse liquid (refraction index  $n = 1.515$ ) under the prism. Spatial movement of the prism could cause changes in spectra due to the different length of the track of light inside the sample. Change of implantation region was done by movement of the sample keeping fixed detection and excitation parts. The angle of detection was estimated with lower precision compared to the angular luminescence measurement. Measurements were done before construction of the second goniometer. The new goniometer could be, however, also used for such measurement, which is one of its great advantages.

**Direct coupling** The sample for this measurement was truncated at an angle of 30 degrees. The intention was to spatially separate light entering the implanted layer from those entering substrate and detect only the light coming through the nanocrystalline layer. The experiment was excited with a white LED. Light from LED was coupled via a collimator into an optical fiber delivering signal to the proximity of the sample. The fiber ended with a collimator similar to the prior one. Divergence of the light exiting fiber was, using the collimator, decreased to approximately 10 degrees. The excitation angle was determined in a similar way as the detection angle and the scale was related to the excited edge of the sample. A spot on the sample was not bigger than the size of the implanted layer to prevent problems with excitation of two different implanted layers at once and to detect mixed spectra of those two different implantations.

The LED was powered by a battery connected to the LED by a resistor. Later, we used the laboratory power supply. The first experiments were done in this setting with a common white LED, however later we exchange it with a warm white LED (WWLED) that has a better spectral profile. Electrical connections were similar, but some minor changes were done after incorporating the WWLED which was bigger than the usual LED. The WWLED dissipate some energy and needs at least passive cooling. A block of Al material connected with thermal conductive paste to the WWLED sufficiently guided thermal energy out of the WWLED active part.

### 4.3 Strong excitation effects in nanocrystals

Measurements described up to now concerned only linear optical properties. However, nonlinear effects depend on the intensity of excitation and appear when intensity overcome certain threshold. The most studied nonlinear effect on semiconductor nanocrystals is optical gain. Various methods for determining the presence of optical gain in material exist.

The method used for the first optical gain measurement on a semiconductor nanocrystal [4] is called variable stripe length (VSL). This method was originally developed for materials with large value of optical gain. Immediately after the article in Nature, many scientists tried to repeat gain observation in Si nanocrystals. However, it was proved that for samples with a low gain coefficient and waveguiding properties, this method has to be supplemented with the shifting excitation spot (SES) method [41].

More direct method to reveal optical gain, is the pump and probe measurement. The method requires two pulses with controlled delay between them. The pump pulse is a strong one, spectrally narrow - a pulsed laser. The probe pulse is low-intensity and spectrally broad. Change of absorption is detected according to the delay between pulses.

Nonlinear measurements performed on our samples were burning of a permanent grating and a pump-and-probe experiment.

#### 4.3.1 Permanent grating burning

Strong optical pulse can damage or destroy the Si nanocrystal layer in implanted materials. Two beams interfering on a sample can burn on a sample grating formed from regions with and without nanocrystalline layer. This is similar to the method of nanocrystals preparation, presented in [48], where two strong lasers are used for burning out holographic grating.

The scheme of set-up is in Fig. 13. Strong excitation for this experiment was provided by ns pulses from a Nd:YAG laser connected to a tunable optical parametric oscillator (OPO). The laser beam was split into two parts by a beam splitter with the 50:50 division ratio. Both beams were then focused on the sample by a single lens. Focus of lens was at the surface of the sample. The sample was mounted on a XYZ translation stage that enables to precise positioning of the sample.

To observe the result of a laser ablation, the Carl Zeis Jena Amplitval optical microscope with total magnification up to 1000 $\times$ , was used. Another

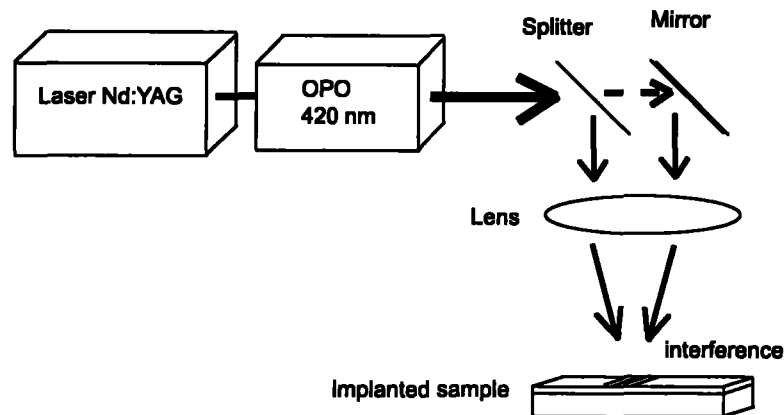


Figure 13: Scheme of arrangement for burning grating into an implanted sample, using strong Nd:YAG laser, with OPO.

direct method is a use of a commercial diode laser that is positioned on the same mount as a prism and a lens. Its light is directed on the sample and then observed on a paper screen behind the sample. If there is a grating on the sample, diffraction pattern can be observed.

#### 4.3.2 Pump-and-probe measurement

Pump-and-probe is an experimental method used to study optical gain and other nonlinear properties of materials. The previous experiments with absorption measurements brought us to the idea that we could try this measurement with white light coupled into the sample as a probe beam.

The sample was positioned in our angular dependence set-up and perpendicularly exposed to a strong laser beam. The angular set-up was used for proper setting of probe and detection angles.

The pump-and-probe measurement is much more complex than the previous measurements, so it is necessary to set and control all the components properly. The best way to control and synchronize all incident pulses is to use pulse generator and oscilloscope. We used two pulse generators and an oscilloscope to detect and check time correlation of each pulse and to send pump and probe pulse at the right time.

The optical part of this experimental setting is presented in Fig. 14. The

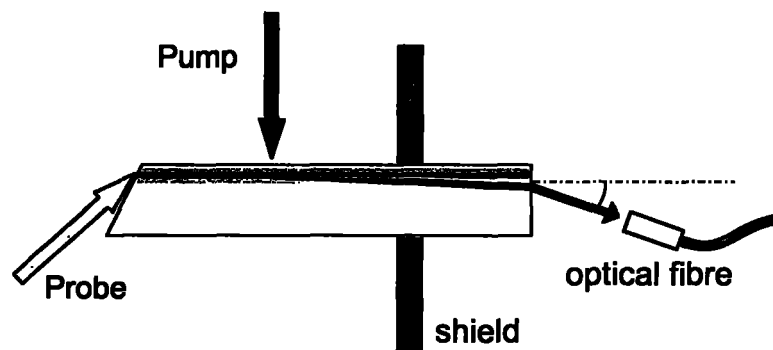


Figure 14: Scheme of the set-up for pump and probe measurement. The probing part is similar to those used for experiments with coupling WWLED into the waveguide. Excitation is supplied by a Nd:YAG laser with OPO.

most important feature is a strong excitation laser with narrow spectral line and a probe pulse with wide emission spectrum. The probe part has already been explained as a direct coupling of WWLED light.

The first pulse-generator, Stanford Research Systems DG535, gives us the reference TTL pulse with duration  $200\mu\text{s}$ . The pulse is then splitted into two channels, one into the laser and the second into the control unit of the intensified CCD (ICCD) camera. The pulse width was chosen as the minimal duration needed for laser triggering. The timing unit and the control software of the ICCD enable to set a delay sequence, which must be synchronized with the test pulse from the WWLED. An output pulse of the ICCD camera triggers the second generator (Avtech AV-1010-B), used as a power supply for the WWLED. The advantage of pulsed WWLED operation is that it can operate at higher current and generate more signal in the detection time window - better signal to noise ratio is achieved and shorter detection windows are applicable.

#### 4.4 Spectral detection

A detection system was set similarly for most of the measurements except grating burning where no spectral detection was used. Detection itself could be separated into several parts. The first is collecting of detected signal from the sample, and then the signal should be spectrally analyzed and detected.

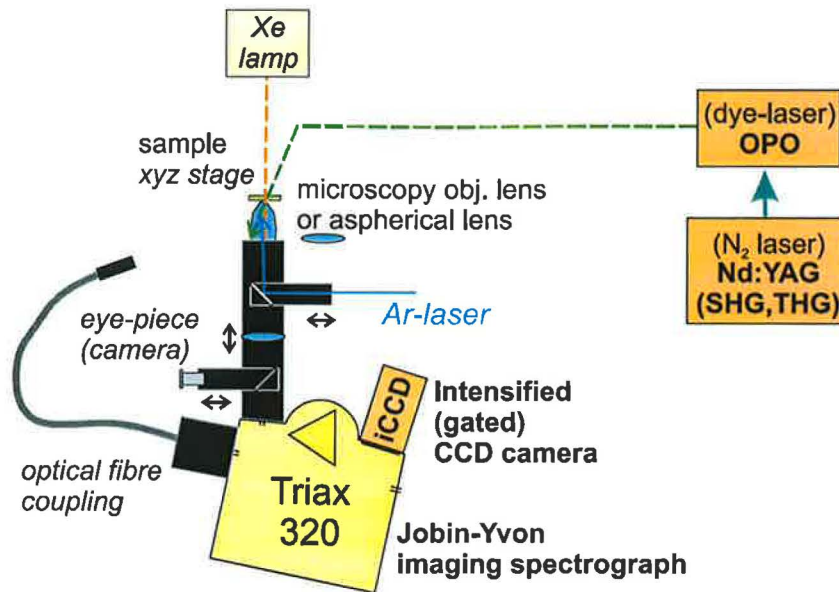


Figure 15: Scheme of a detection part of experiments. System contain gathering of the signal (black parts), an imaging spectrometer and an ICCD camera.

The signal collection in our set-up is performed by two ways (Fig. 15-black part). One way is a double lens system consisting of an aspherical collection lens ( $f=5$  cm) and a collimating achromatic lens ( $f=20$  cm), which focuses light onto the entrance slit of a spectrometer. The other is an optical fiber with round core of 1 mm in diameter. A detection angle of the fiber is about  $1^\circ$ . The second termination of the fiber is shaped into rectangular arrangement of the core adapted for connection to the spectrometer.

The signal is guided on the entrance slit of the imaging spectrometer Jobin Yvon Triax 320. Although spectrometer consists of three gratings on a turret, only one of them was used for all measurements - the low-dispersion grating with 100 grooves/mm. One of two possible sources of the signal is selected by a mirror behind the entrance slit which switches axial or side entrance. Both entrance slits, as well as the mirror (not presented in Fig. 15, could be controlled separately by a computer software allowing easy change of the signal source.

The final detection is performed by the ICCD PI-Max Princeton Instruments camera attached to the exit of the spectrometer. It is possible to cool the camera down by incorporated Peltier cooling (thermoelectric effect) to decrease dark noise. For all measurements temperature of the camera was set at  $-20^{\circ}\text{C}$ . This camera is designed for visible light and has lower sensitivity at longer wavelengths. This fact should be considered when results at wavelength longer than 850 nm are discussed.

Time resolved spectra could be measured by the same equipment. The ICCD is able to measure processes down to 5 ns resolution. This feature was used for time-resolved photoluminescence measurement in porous silicon colloids.

For polarization resolved measurement, linear polarizer positioned between the sample and the detection fiber was used. The polarizer is manually controlled.

#### 4.5 Single nanocrystal spectroscopy

Common optical investigation of nanocrystals is done with samples containing huge number of nanocrystals. In such ensemble measurement the distribution of individual properties causes inhomogeneous broadening of spectra. Therefore much information is lost. There are some special spectroscopy techniques like the site-selective or spectral hole-burning spectroscopy that can, to some extent, overcome inhomogeneous broadening. But they are quite complicated, applicable only in special cases and sometimes difficult to interpret. Therefore, the best way is to measure directly spectra of single nanocrystals. The technique was developed first for single molecules in 1990 and modified for nanocrystals in 1992. There are three main requirements for single nanocrystal measurement: (i) preparation of very clean and diluted sample, (ii) excitation and detection of the smallest possible volume (using high NA wide-field optics or near-field optics), (iii) the highest possible efficiency of signal collection and detection. The single nanocrystal spectroscopy was used mainly for nanocrystals of II-VI and III-V semiconductors and even for Si nanocrystals. These experiments revealed not only hidden fine spectral features but also new unexpected effects like on-off blinking (intermittency)[51].

## 5 Results and discussion

The samples used in this work have already been described above. They include colloidal suspensions of porous silicon, implanted layers of nanocrystals in silica glasses and nanocrystals in photonic crystals. Results obtained on each material are described in a separate section with discussion following immediately.

All experiments presented in this thesis were measured at room temperature and atmospheric pressure and the spectra were corrected for the spectral response of the applied detection system.

### 5.1 Luminescence of porous silicon colloids

Luminescence from Si nanocrystals has been known since 1990 [2] when it was first detected on Si material at room temperature. The material used in this experiment was porous silicon. Porous silicon is also the source material for the preparation of colloids used in this work and the related article [1].

Properties of porous silicon itself can be found in many articles like [12, 31]. Here we describe only properties of porous silicon colloidal suspensions.

As prepared suspension contain mainly sub- $\mu\text{m}$  grains of porous silicon with yellow color that emit strong orange luminescence (Fig. 16 - green line). After few hours lasting sedimentation, the luminescence spectra intensity decreases and the maximum blue shift (Fig. 16 - red line). Sedimentation time depends on viscosity and density of the suspension. Filtration through filter with a pore size of  $0.2 \mu\text{m}$  removes the biggest particles. The filtered suspension lost its color and spectra move to a shorter wavelength (blue shift), see Fig. 16 - black line. Both the presented effects suggest that the majority of nanocrystals were lost and only very small particles remained in the colloid.

The presence of the nanocrystals in the colloid is proved by absorption or by the Raman spectroscopy. The absorption spectra present a blue shift when compared to the non-filtered suspension. The change of the Raman spectra indicates mean diameter of silicon nanocrystals approximately 2 nm in both filtered or non-filtered suspension.

Fig. 16 shows appearance of otherwise hidden green photoluminescence band when big grains of porous silicon are sedimented or filtered away.

The theory suggests that a green photoluminescence should be linked to the presence of small nanocrystals with oxygen related surface states not

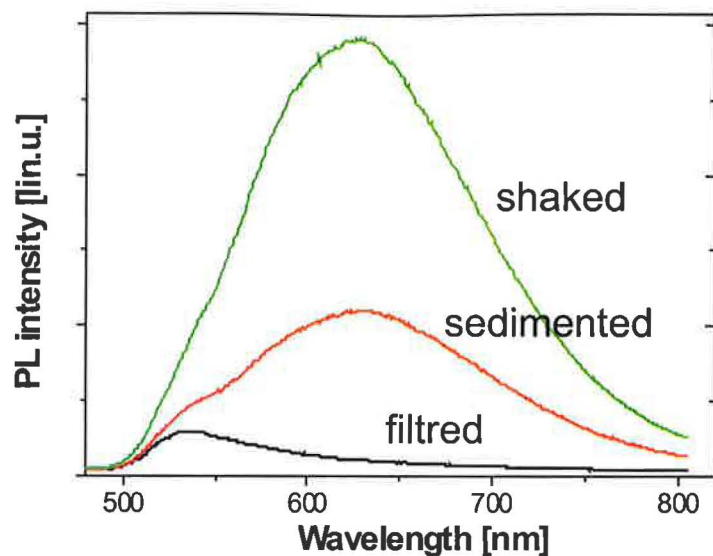


Figure 16: Luminescence spectra of Si nanocrystals in ethanol (excitation by the 458 nm line of the Ar-laser): a - freshly shaken colloid, b - 1 hour sedimented colloid, c - filtered colloid.

affecting the radiative recombination of electron-hole pairs. The same effect, green photoluminescence, was well described by several observations of various samples. The reason why oxygen-related surface states are not so effective has to be investigated in future. We can suggest that it is due to the high curvature of a small nanocrystal surface that disable formation of stable O=Si bonds.

Diluted suspensions allow single quantum dot spectroscopy of the individual silicon nanocrystals. The green photoluminescence of silicon nanocrystals remains stable even after evaporation of a solvent. High value of auto-correlation function and presence of intermittence in the photoluminescence prove that signal is from single nanocrystal. The shape of the single silicon nanocrystal spectra is asymmetrically enlarged to lower energies. Similar single nanocrystal spectra, described in [52], explained this enlargement by a sub-band connected with the Si-O-Si vibrational feature.



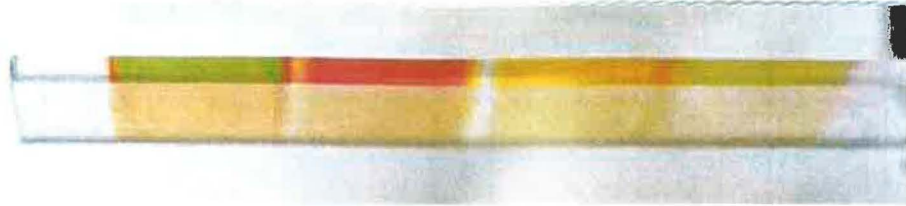


Figure 17: Photography of an implanted sample in diffused ambient light. The four regions were implanted with doses  $6 \times 10^{17} \text{cm}^{-2}$ ,  $5 \times 10^{17} \text{cm}^{-2}$ ,  $4 \times 10^{17} \text{cm}^{-2}$  and  $3 \times 10^{17} \text{cm}^{-2}$  (from the left to right ).

## 5.2 Implanted silica glasses

Two series of samples containing Si nanocrystals implanted in fused silica glasses were used in this study. Each glass was divided into regions with different implantation doses. The first set prepared with four regions, contains implantation doses from  $3 \times 10^{17}$  to  $6 \times 10^{17} \text{cm}^{-2}$  with steps in implantation  $1 \times 10^{17} \text{cm}^{-2}$  (Fig. 17). The second sample, was designed according to previous results to have higher implantation doses and smaller steps. The glass contains 5 regions with implantation doses from 4 up to 6 with dose step  $0.5 \times 10^{17} \text{cm}^{-2}$ .

Explanation of our measured data will start with characterization of samples (some measurements were performed in cooperating laboratories). Knowing basic information about our samples, we can build equipment to study its properties. In this thesis we describe experiments on luminescence and its angular dependence, waveguiding properties with coupling light into the layer, and at the end, there are results from measurement of nonlinear properties of our samples.

### 5.2.1 Characterization of samples

The preparation of Si nanocrystals inside a silica glass was described in the section 3.2.2 and a change of the absorption spectra before and after last annealing (passivation) will be described here. The spectra were measured by the commercial two beam absorption spectrometer Perkin Elmer and the result is presented in Fig. 18. Nanocrystals are formed during the annealing stage of the sample preparation, hence the change observed in absorption

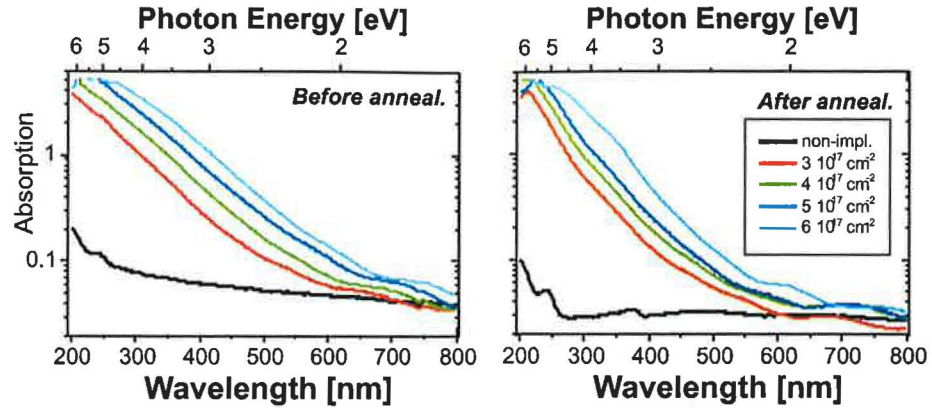


Figure 18: Absorption measurement of the samples as implanted and annealed in  $N_2$  atmosphere for 2 hours. Each line stands for one implantation dose.

measurement is the change between the as implanted sample and the sample with a layer of nanocrystals inside the sample. Similar results were presented in [53] by the Khriachtchev's group studying similar samples. Knowledge of absorption spectra is important also for luminescence measurement to choose the proper wavelength which is sufficiently absorbed in nanocrystals.

In order to numerically model the optical properties of samples, the refraction index profile should be characterized separately for each implantation. The first piece of information could be obtained from implantation parameters and the known depth and density of ions for applied implantation energy. Determination of properties can continue by measuring infra-red transmission spectra [III] and fitting the interference fringes using an asymmetric double-Gaussian refraction index profile. The maximum of the profile is usually approximately 600 nm below the surface with a half width of approximately 300 nm. The peak refraction index increase up to the value of 2, for the highest implantation fluence (see Fig. 7).

The diameter of nanocrystals in our samples is estimated using Raman scattering presented for example in [49]. The evaluation of a nanocrystal size from its Raman spectra was carried out according to the equation derived in the article [42]. The shift of Raman spectra and the change of its shape reveal that used samples contain nanocrystals of approximately 4 nm in diameter.

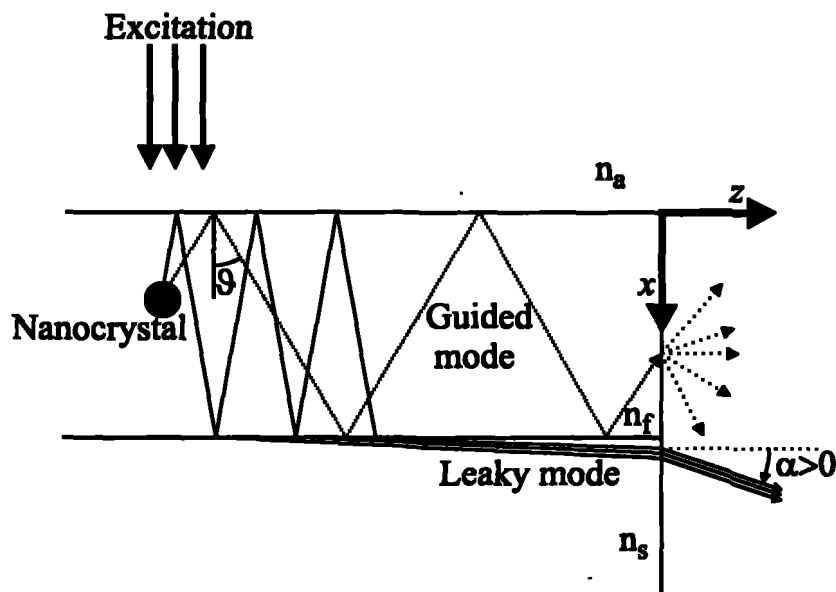


Figure 19: Schematic representation of the model of leaking modes, with one nanocrystal as a radiation source, adapted from [50].

### 5.2.2 Theory of Si waveguides

Our implanted samples contain a layer of nanocrystals formed from excess Si ions in a silica glass matrix. The nanocrystalline layer has a higher refractive index than matrix, and hence it reveals waveguiding properties. Such a waveguide may be called "active" because the light-emitting nanocrystals are embedded within the waveguide.

Currently there are two different theoretical models able to explain observed behavior of waveguides. One model was developed in our department by T.Ostatnicky [50] and is based on the theory of radiative modes leaking out of the waveguide core (Fig. 19). At the University of Helsinki [53, 45] a different model was developed considering the delocalized guided modes inside waveguiding structure. In this section both models are explained but more attention is given to the model of leaking modes.

The refractive index profile of a waveguide layer is in fact asymmetrical (revealing the shape of implantation profile and proximity of the surface of

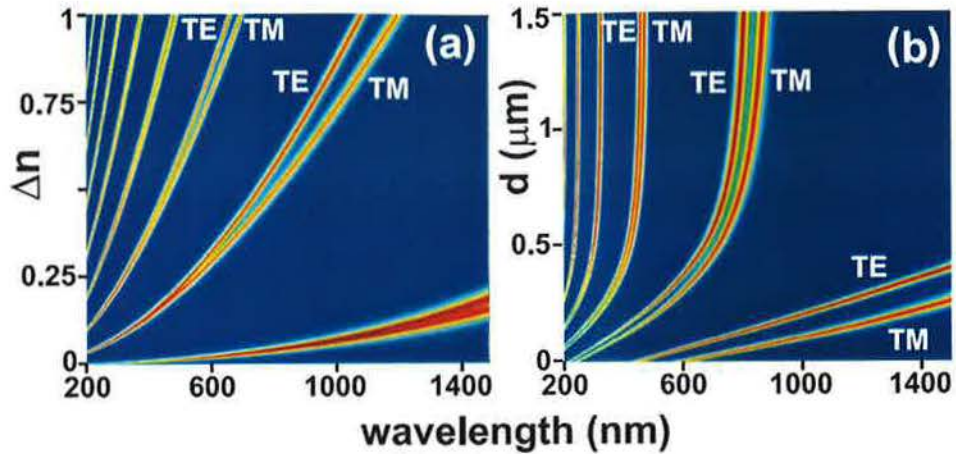


Figure 20: Model calculation of spectral splitting of TE and TM modes. Intensity of each maxima is presented by color temperature as a function of (a) wavelength and change of refraction index, (b) wavelength and depth of refraction index maxima. (Numerical calculation by T. Ostatnicky)

a substrate) and may be approximated by a combination of two Gaussian profiles - see Fig. 7. The standard waveguiding theory consider radiation propagating inside the structure and energy that get out of the core is considered as losses. However, both developed models expect radiation near the boundary of the waveguide as the signal detected at the edge of the sample.

The model, developed by Khriachtchev's group, suppose that the polarization splitting of the guided signal is due to delocalized guided mode. The model expects signal guided in the "weakly guided" modes. Such modes propagate in the waveguide in direction almost parallel to its axis. Ray optics describes these modes with angle of incidence greater (but only slightly) than the critical angle for the total reflection.

The competitive model, developed by T. Ostatnicky, involve leaking radiation modes. These modes propagate with the angle slightly smaller then critical angle. These modes are totally reflected on the upper boundary with higher refraction index contrast (air/waveguide) and only partially reflected on the bottom boundary with lower refraction index contrast (waveguide/substrate). Small fraction of energy is radiated to the substrate at each reflection and form "leaking modes". The leaking modes propagate almost



parallel to the implanted layer. The larger number of reflections inside the material results in narrower modes. The polarization splitting of modes is caused by different phase shift of the transverse electric (TE) and the transverse magnetic (TM) waves on the waveguide boundaries.

Both the described models are able to explain main features of our experiments. In order to prove which model is valid the following experiment was proposed and performed by Pelant's group at Institute of Physics Czech Academy of Sciences. It is based on local modification of surface refraction index by drops of liquids. It was shown that a drop influences observed modes only when it is placed above the excited spot of waveguide, but not when it is placed between that spot and the sample edge from which radiation is detected. This is in conflict with a model of guided modes but agrees with a model of leaking modes. The leaking modes radiates in substrate and cannot be influenced by changes of the upper waveguide boundary any longer. These measurements were presented in [49].

Previous paragraph has shown superiority of the model developed by T. Ostatnicky. Therefore we will compare our experimental results only with numerical calculations based on the modes of substrate leaking modes. The numerical calculations based on this model are in excellent agreement with our experiments and may be applied to design modified samples with desired properties. In Fig. 20 we presented calculated dependence of the leaking modes spectral positions on the refraction index contrast on the waveguide boundary and the depth of waveguide under the surface.

### 5.2.3 Angular measurement of luminescence

Under laser excitation, nanocrystals emit luminescence in all directions. This luminescence propagates through the sample and part of it may be reabsorbed, refracted or scattered.

Fig. 21 presents luminescence spectra detected from nanocrystals implanted in the sample. Different intensities for each implantation dose could be observed. The theory would predict that lower implantation would imply smaller nanocrystals and therefore higher energy gap. However, it is difficult to observe such changes in this figure, a comparison of this spectra with other photoluminescence results on Si nanocrystals presented for example in [1] show significant agreement. This could be presented also as a proof of the presence of Si nanocrystals inside the material.

In Fig. 22, differences between spectra detected from the edge and from

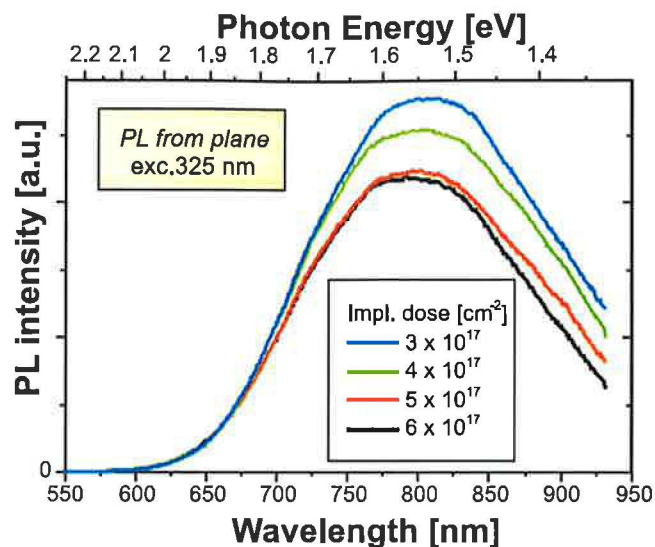


Figure 21: Luminescence from the plane of the samples with implantation doses from  $3 \times 10^{17} \text{ cm}^{-2}$  up to  $6 \times 10^{17} \text{ cm}^{-2}$ .

the plane of the sample are presented. Spectra from the plane (the angle bigger than  $15^\circ$ ) are similar to those detected from Si nanocrystals themselves (Fig. 21). On the other hand, the signal from the edge of the sample contains two narrow polarization resolved peaks (polarization splitting will be discussed later).

The following figures will contain only spectra detected from the edge. Fig. 23 and Fig. 24 present change of polarization resolved maxima according to the implantation dose for our two sets of implanted glasses. The broader bands are due to normal guided light while the narrow peaks are the leaking polarization-splitting modes. The left part of the Fig. 23 shows the detected spectra, and its right side shows theoretically calculated spectra. Behind the edge detected data, there is a dotted line representing luminescence spectra detected from the plane. It is possible to see a very good agreement between the detected and calculated spectra. Luminescence spectra of the second set of implantations (Fig. 24) are presented in a logarithmic scale of the luminescence intensity.

Fig. 25 shows the linearly polarized spectra of a region with implantation

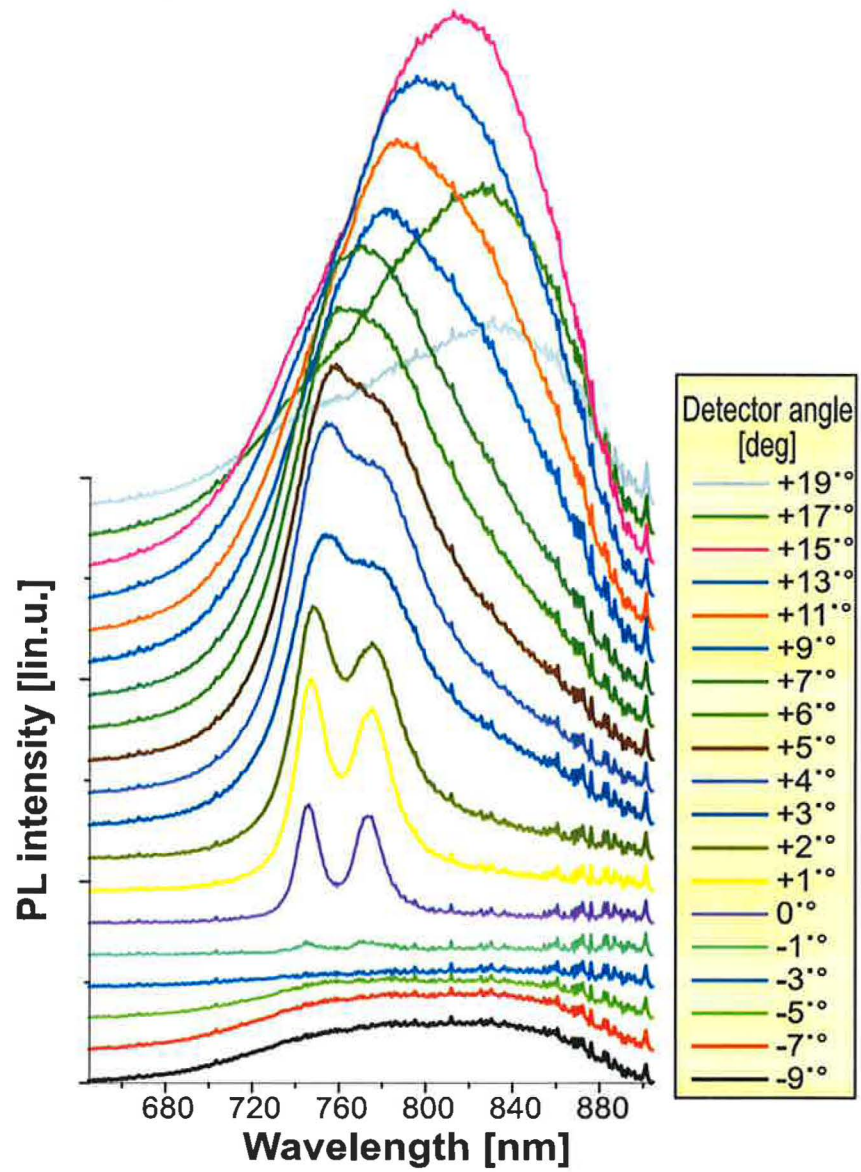


Figure 22: Angular dependence of luminescence, implantation dose  $5 \times 10^{17} \text{ cm}^{-2}$ . Angle  $0^\circ$  is in direction parallel to the implanted layer.

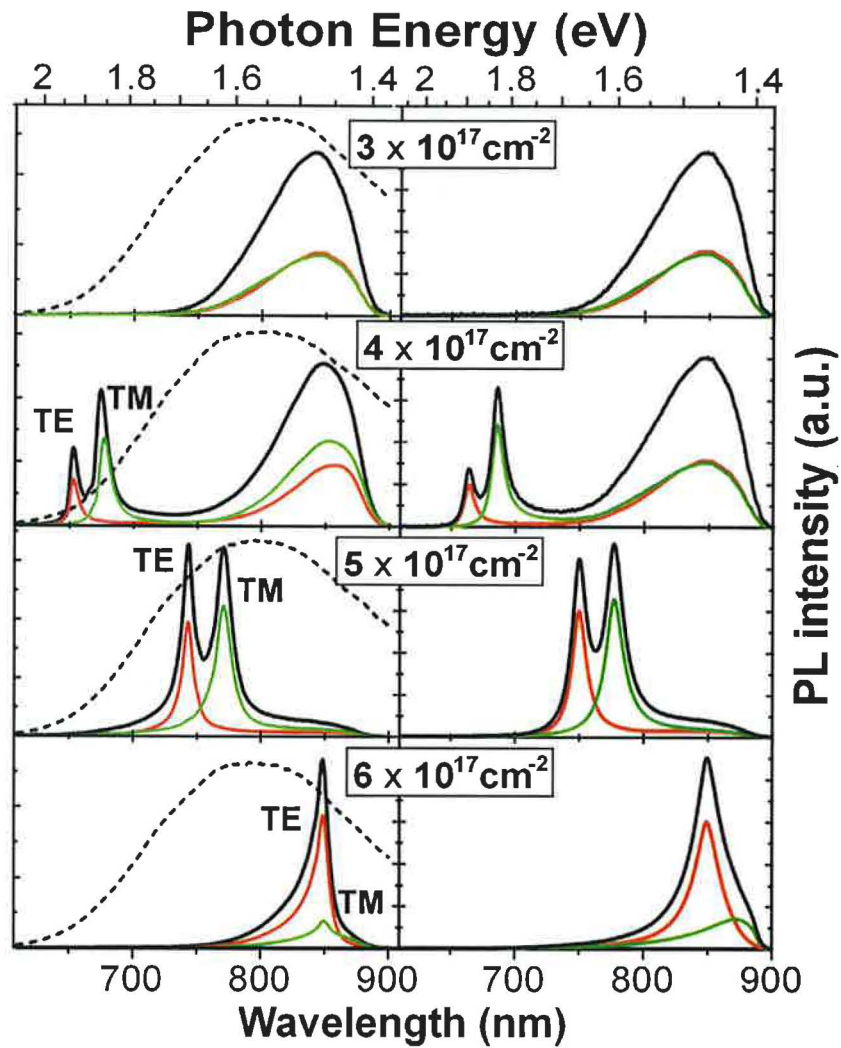


Figure 23: Luminescence spectra of samples with implantation dose from  $3$  to  $6 \times 10^{17} \text{ cm}^{-2}$  - sample 1. The figure compares data obtained by measurement (left part) and theoretical calculations (right part). Luminescence spectra from the edge (solid line) are supplemented with luminescence spectra from the plane (dashed line). (Figure adapted from [54]).



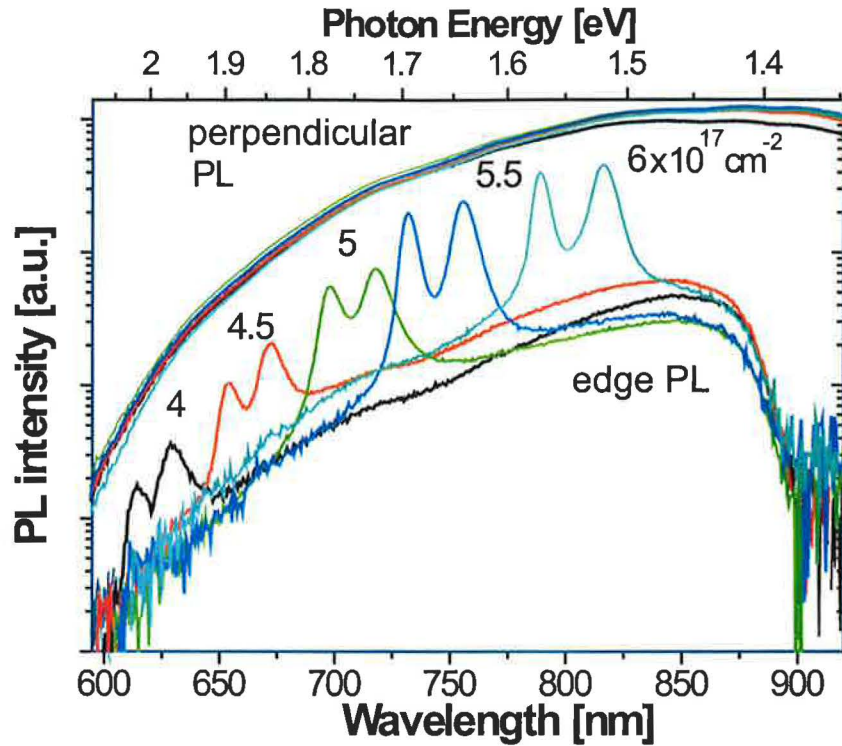


Figure 24: Luminescence spectra of samples with implantation dose from 4 to  $6 \times 10^{17} \text{ cm}^{-2}$  - sample 2. Spectra of all implantations are compared to luminescence from the plane, logarithmic scale of PL intensity axis.

dose  $5.5 \times 10^{17} \text{ cm}^{-2}$ . Peak at lower wavelength is TE polarized and the second one is TM polarized. Changing polarizer orientation causes a change in proportion of each maxima. It is possible to set the desired ratio between those two polarizations. Indicated angles are related to zero which is set as TM polarization. This figure also shows a broad band at longer wavelength. This is the remaining part of normally guided light. For greater detail, see Fig. 23, 24 where this effect is also noticeable.

The presented luminescence spectra were compared with oxidized silicon layers implanted with Si ions [III]. The layer of implanted nanocrystals presents similar effects for both substrates. However, in silica glasses lumi-

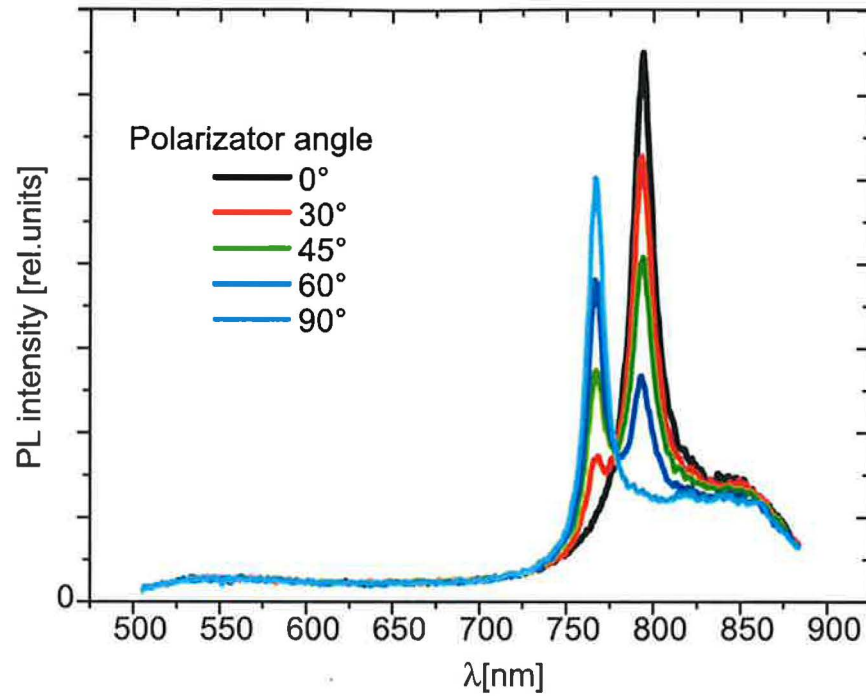


Figure 25: Polarization resolved luminescence spectra detected from the sample with implantation dose  $5.5 \times 10^{17} \text{ cm}^{-2}$ . Relative angles of the polarizer are counted from TM polarization (0 degrees) up to TE polarization (90 degrees).

nescence spectra from the edge are narrower, and present higher polarization splitting.

#### 5.2.4 Waveguiding properties

Experiments with light coupling into the sample started with direct coupling of a white LED guided through an optical fiber. The spectrum of this source consists of one strong blue peak and a broad orange band with much lower intensity. Results of this measurement are not presented here because only absorption spectra for sample with implantation  $5.5 \times 10^{17} \text{ cm}^{-2}$  were detected. As was later recognized, the problem consisted in an unsuitable

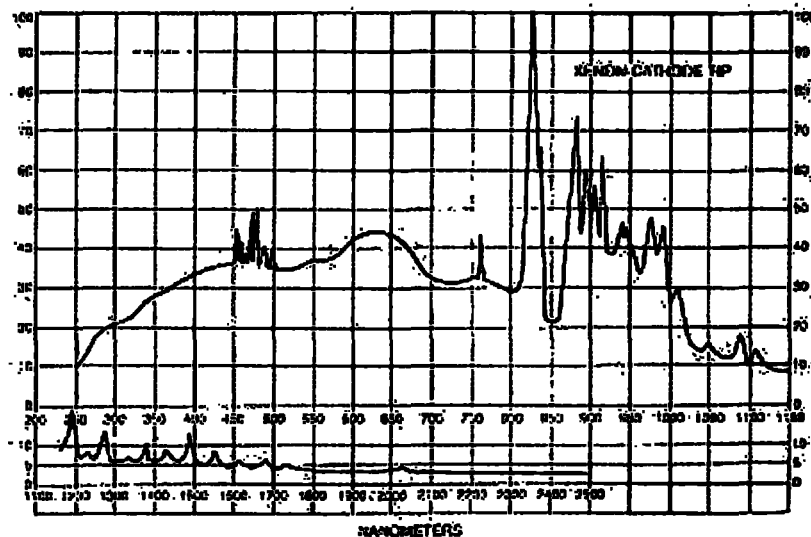


Figure 26: Spectrum of Xe lamp taken from data sheet of of Photon Technology International company.

source of white light - a bad profile of the spectra.

The attention was then changed to a prism coupling experiment similar to measurement done by Prof. Elliman's group [47]. An interesting results obtained from measurement with light coupling into the sample lead us to an idea of trying once more measurement of directly coupled white light. This time, a better LED with wider spectra and with lower blue peak (or higher intensity at longer wavelength) was found. More precise explanations of both coupling methods are in the following sections and were published in [II,III].

### 5.2.5 Prism coupling

Emission spectrum of the Xe lamp is shown in Fig. 26. This spectrum reveals quite narrow peaks at 750 nm and 850 nm. When measuring the absorption spectra (by comparing incident Xe-lamp spectrum with that modified by passing a sample), these two strong peaks cause serious problem. On the other hand a halogen lamp with smooth spectrum is much better for wavelengths around 800 nm, but the emission at short wavelength is too low for

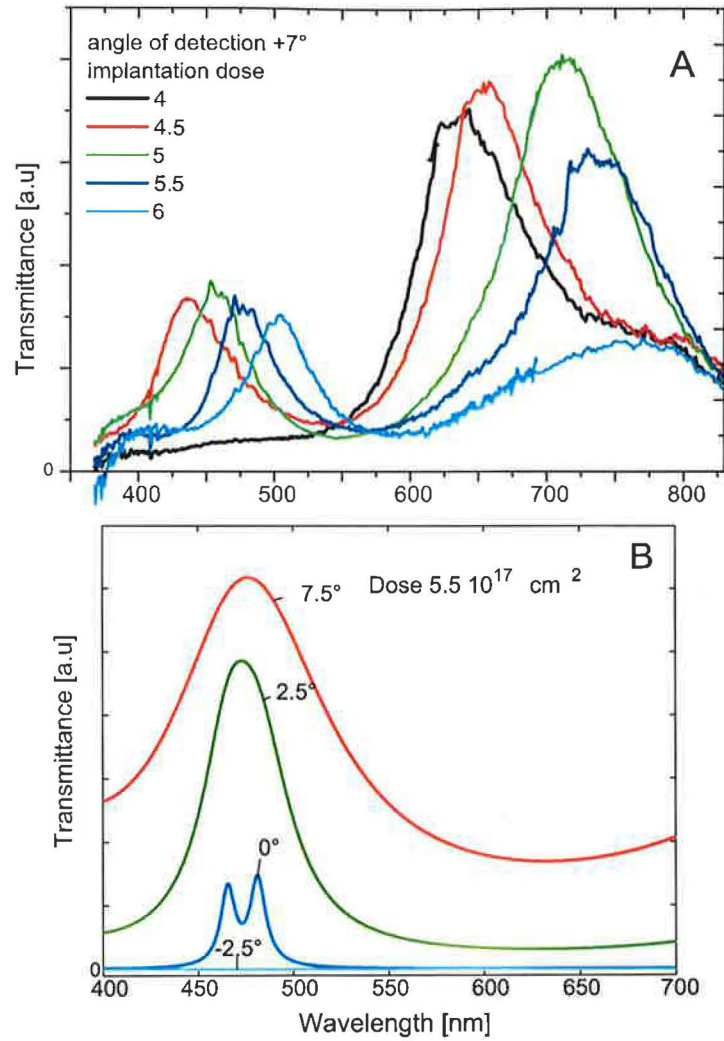


Figure 27: (A) Prism coupled light from Xe and halogen lamps, for all implantation doses, detected at  $7^\circ$ . The positions of maxima at longer wavelength are comparable to the positions of luminescence maxima, (B) Theoretical transmission spectra of prism coupled signal, calculated for implantation dose  $5.5 \times 10^{17} \text{ cm}^{-2}$  by T. Ostatnicky.

our measurements. The first measurements were done with the Xe lamp for all implanted areas. Later we changed the lamp and measured all samples with the halogen lamp coupled to an optical waveguide.

Fig. 27A shows the detected transmittance spectra. Spectra obtained with both lamps are adapted for proper correspondence. Each spectrum contains two bands whose position red-shifts with the increasing implantation dose. Position of the long wavelength bands coincide with the luminescence bands, detected from edge of the sample for each implantation (Fig. 24). The short wavelength bands agree with the theoretically calculated higher order (3<sup>rd</sup>) of the leaking modes. The presented spectra were detected at 7°. The signal at different detection angles were not so strong, so the individual bands were not visible so clearly.

The theoretical calculation (done by T. Ostatnicky) of the measured data is in Fig. 27B. The graph presents only the spectra of implantation dose  $5.5 \times 10^{17} \text{ cm}^{-2}$  that are presented in Fig. 27A (dark blue line). The theoretical calculation contains only one band (shorter wavelength). The theoretical model shows that transmission for polarization resolved spectra should be much lower than for our presented 7° and that is the reason why it was not detected. The second reason is that our detection system for this measurement has too big numerical aperture for detection of well resolved modes. The influence of numerical aperture on spectral resolution has been mentioned in the description of the theoretical model.

The shape and intensity of the signal were very sensitive to the position of the prism. Moving the prism or rotating it changes the amount of the signal as well as the quantity of immersion oil. However, no systematic change linked to the movement of the prism was observed and hence is not presented here.

### 5.2.6 Direct coupling

The results of the measurement with a normal white LED show absorption peak only for implantations  $5.5 \times 10^{17} \text{ cm}^{-2}$  and other implantation present no interesting properties. However, after measurement using prism, where the transmission spectra for all implantations were detected, we decided to find a better source of white light than the standard white LED. The best spectral shape present Luxeon warm white LED LXHL-BW03 with color temperature 5500 K (WWLED). This source allows detecting absorption spectra with a strong peak for implantations from  $5 \times 10^{17} \text{ cm}^{-2}$  up to  $6 \times 10^{17} \text{ cm}^{-2}$ .

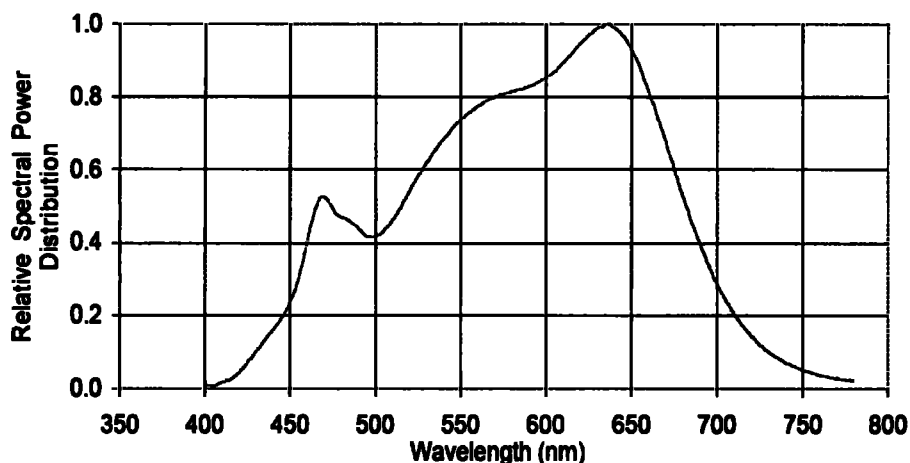


Figure 28: Spectrum of the warm white LED - Luxeon Emitter - taken from original data sheet.

The Fig. 28 shows spectra of the WWLED used as a source of white light. In comparison to the standard white LED, the intensity of the orange band is much higher and there is also one more peak in the red part of the the spectra (630 nm). The WWLED has an emission angle of 40 degrees. However, in our arrangement where light from the WWLED was coupled into the optical fiber, the most important number is the exit aperture of the fiber. This value was adapted using a collimator at the end of the fiber near the sample.

According to the results of the prism coupled signal, the signal was expected at certain wavelengths. However, coupling light directly shows different spectra. The position of the peaks is similar, but instead of higher transmission, we observe absorption peaks. Fig. 29 shows the comparison of the directly coupled signal and the signal coupled by a prism. Polarization splitting is proved by polarization resolved measurement, only for direct coupling, the prism coupling signal reveals only weak polarization dependence. The second transmission maxima as presented in Fig. 27 cannot be compared because they are not detected in the direct coupling experiment. This fact can be explained by two consequent effects. For lower implantation doses, absorption is low and therefore spectra are difficult to evaluate. A higher

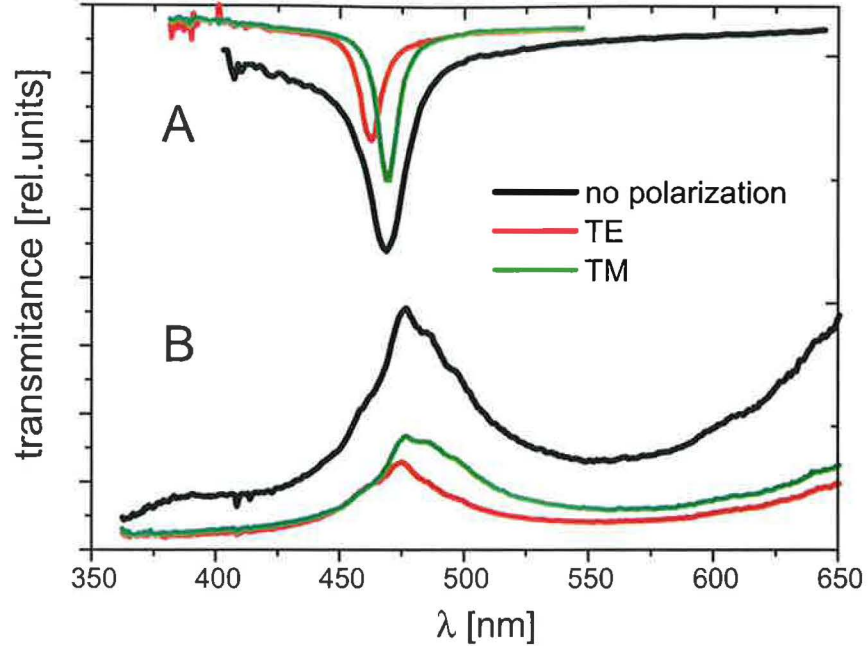


Figure 29: Absorption spectra from direct coupling compared with those coupled through the prism - implantation dose  $5.5 \times 10^{17} \text{ cm}^{-2}$ .

implantation dose presents a higher absorption but the position of the second maxima are in a region where the WWLED has low emission intensity so absorption is hard to evaluate again. The shape of spectra detected by direct coupling is more similar to luminescence measurement than it is for the prism coupled signal.

Fig. 30 presents absorption spectra for three implantation doses from  $5 \times 10^{17} \text{ cm}^{-2}$  up to  $6 \times 10^{17} \text{ cm}^{-2}$ . The position of the absorption peak follows similar dependence on implantation dose as that expected from the luminescence spectra shift as well as from the prism coupled spectra. Non-polarized spectra do not show visible splitting. However, separate measurement of the TE and TM polarization reveals polarization splitting presented by red (TE polarization) and green (TM polarization) lines in the spectra of each implantation dose. The theory published in [IV] predict similar behavior of



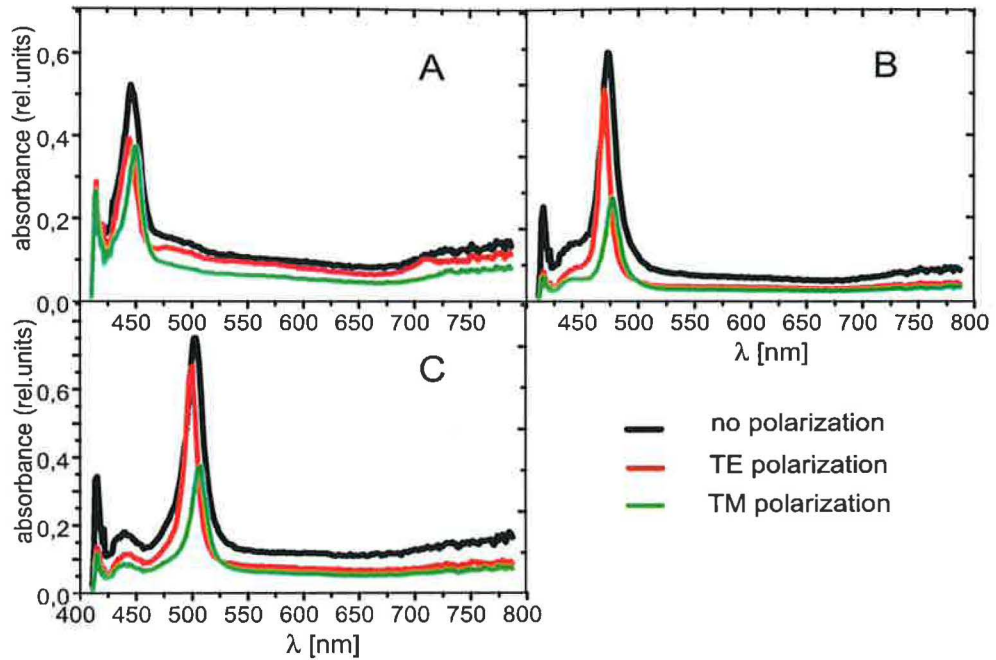


Figure 30: Absorption spectra obtained with directly coupled WWLED light. Three figures present three implantation doses ( $5, 5.5, 6 \times 10^{17} \text{ cm}^{-2}$ ) and polarization splitting of each spectra is represented with different colors.

signal directly coupled to the sample.

The angular dependence of the absorption spectra was measured to compare with the luminescence spectra already presented. The observed dependence presented in Fig. 31 reveals a sharp peak moving its spectral position according to the angle of detection. The spectra are normalized at wavelength of 650 nm. The absorption at low angles has no structure and in fact there is much higher absorption than when using higher angles. The reason is that light absorption is mainly in the waveguiding layer and hence when we detect the signal directly from the layer, the signal is low. This effect was also calculated and results of the calculated and detected spectra suggest the same behavior of maxima according to the angle of detection.



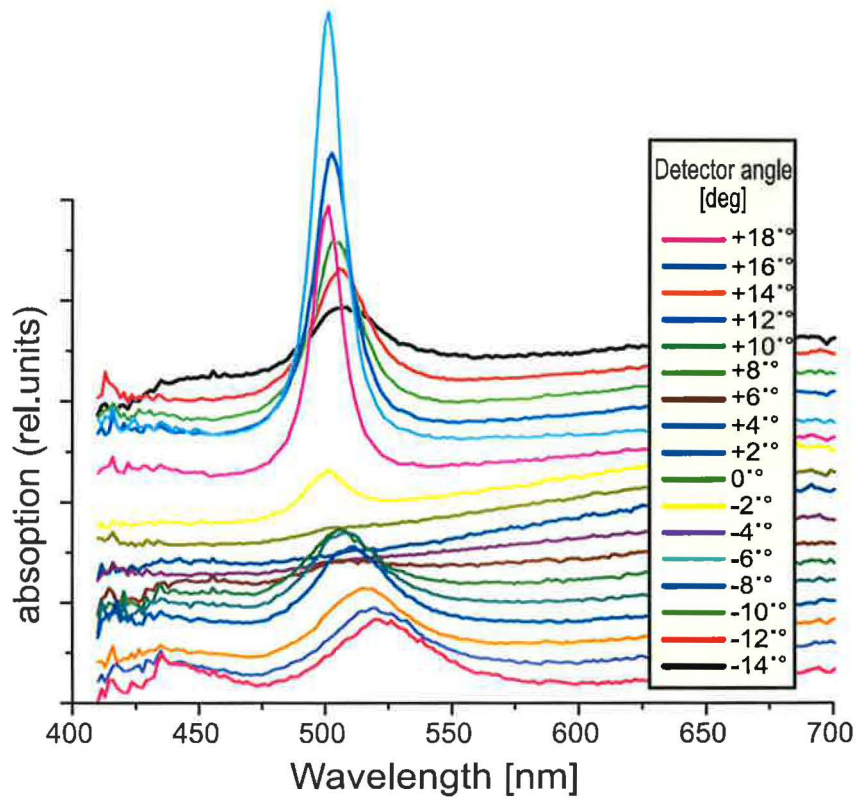


Figure 31: Angular dependence of absorption spectra, implantation dose  $6 \times 10^{17} \text{ cm}^{-2}$ .

### 5.2.7 Permanent grating burning

For this measurement, the spot on the sample was calculated to be approximately  $10 \mu\text{m}$  in diameter. The value comes from the diameter of the laser beam and the position of the lens with known focal length. Direct measurement is quite difficult and this is a sufficient precision for our purposes.

The important step in observing nonlinear properties of a material is to determine the maximum possible energy for excitation before the sample is damaged permanently. For determination of this limit, an old sample which had already been partially damaged and divided into several parts was used.

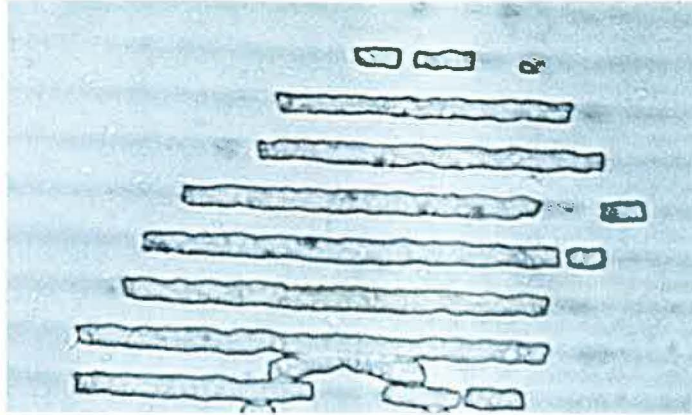


Figure 32: Microscopy image of a burned structure - grating burned in Vilnius laboratory with fs laser pulses.

The data about the threshold measurement were used for the subsequent pump and probe experiment to avoid permanent changes.

The Prof. Pelant's group from the Academy of Science with Tomasiunas's group in Vilnius University has recently published a study on grating burned into implanted samples [III]. Using 400 fs pulses at 400 nm from SHG-Ti:sapphire laser. The interference of the pulses form a high contrast grating in the sample, Fig. 32.

These results inspired us to study similar effects with our ns laser. A different duration of laser pulses in our system (ns), together with the previous results, could reveal more information about the processes taking place in these samples under strong excitation.

Fig. 33 presents a diffraction pattern obtained by diffraction of a HeNe laser beam aimed at one burned spot. Fig 33A presents our results and Fig. 33B is the pattern of grating burned out in Vilnius. The grating in our sample has low contrast, so the diffraction pattern obtained from it reveals only the second order maxima instead of more than 4<sup>th</sup> order for grating prepared by the fs laser pulses. It is considered that in the case of ns pulses the most probable explanation is heating and even melting of Si-NCs [55] which leads to failure of the silica matrix.



Figure 33: Pattern of a laser beam diffracted on a grating burned in the sample. (A) An excitation with ns laser pulses, (B) excitation with fs laser pulses.

### 5.2.8 Pump and probe experiment

The basic experimental setting was based on an angular set-up which enable proper setting of the optimal excitation and detection angle. The adaptations done for this measurement have already been described. The WWLED used in the pulsed regime could be fed by higher current, than in case when used in continuous regime because of possible thermal damage, and hence obtain a higher signal. The pulses were  $100 \mu\text{s}$  long, which were the shortest pulses that the detection system could detect. In the detection part, inside the detection spectrometer (Jobin Yvon Triax 320), there was the GG3 filter to block the laser wavelength scattered at the sample and collected by the detection fiber.

The pump-and-probe measurement in this study was the first experiment of this kind carried out on this sample in our laboratory. The system prepared and used for coupling of white light is in fact one part of the experimental set-up necessary for a pump-and-probe measurement. The only important

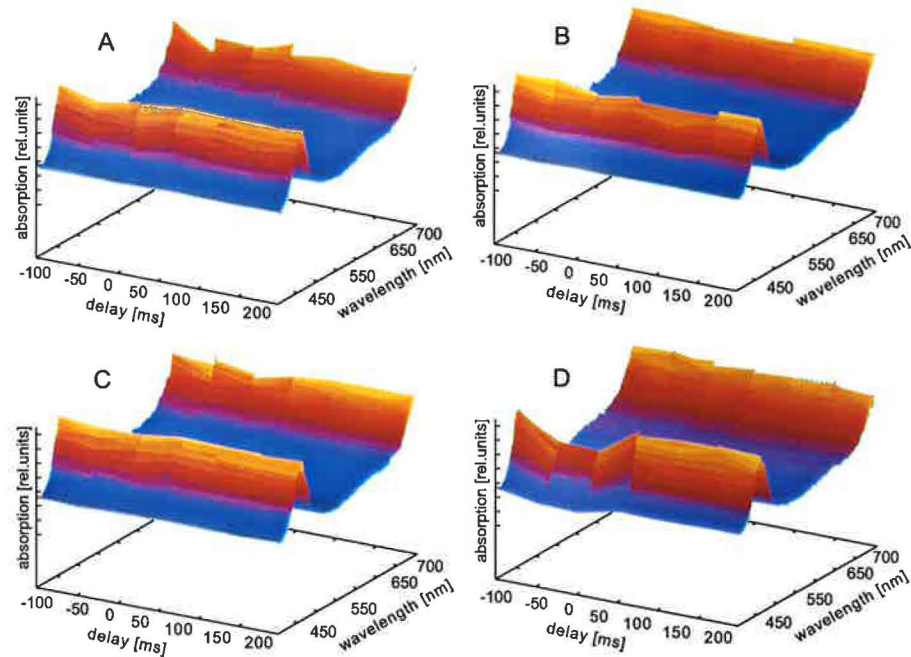


Figure 34: Pump-and-probe measurement of a sample with implantation dose  $6 \times 10^{17} \text{ cm}^{-2}$ . Absorption spectra detected for various delay time between the pump and probe pulses. Time 0  $\mu\text{s}$  agrees with time when the laser pulse was present. The letters A - D present growing pump pulse energy. Figure D is for excitation above  $50 \text{ kW/cm}^2$ .

change is that one strong excitation pulse is also present and in contrast the absorption measurement, the pump-and-probe need pulsed sources. The WWLED used for experiments is fast enough, its time constant is approximately several  $\mu\text{s}$ . It is shorter time than was the time-resolution of our experiments.

As a pump pulse we used 420 nm, 5 ns output of the optical parametric oscillator (OPO) pumped by the SHG-Nd:YAG (NL 303 + PG122, Ekspla). Pump beam is directed in the first half of the sample length, from the view of the incoming WWLED beam.

It is clear from the measurements that using a WWLED with the shortest possible pulse of 100  $\mu\text{s}$  is not sufficient for signal accumulation. We found

changes in this sample, but probably due to the long accumulation time of the signal, we were not able to detect faster processes than several hundreds of  $\mu\text{s}$ .

Fig. 34 presents intensity dependence of the absorption spectra, the increasing intensity of excitation follows the letters on the chart. When the pumping energy density exceeds  $50 \text{ kW/cm}^2$  (Fig. 34D), a decrease of the absorption is observed. An effect is observed only for measurements at time when the pumping laser is present on the sample. This observation means that decay of this effect is faster than tens of  $\mu\text{s}$  and our system is not able to detect it. The decrease of the absorption is a desired effect, which is promising for achievement of optical gain - negative absorption coefficient.

### 5.3 Photonic crystals

The problems with preparation of materials containing photonic crystals were described in the section 3.2.3. The samples we study were fragile and hard to handle. Their implantation was even more difficult, and hence only several samples were suitable for the measurements. Investigation of new method of preparation, colloid suspension of porous silicon, gives another possibility to prepare high quality photonic crystal with nanocrystals embedded inside.

The first article on this topic from our group [39], presented luminescence, reflection and absorption spectra revealing basic properties expected when studying photonic crystals. The stop-band was observed on a high quality ordered photonic structure, and respectively low effect was observed on disordered parts of the sample.

The latest experiments were done on opals with voids filled with colloidal suspension of porous silicon. The original sample, where nanocrystals are implanted inside the opals, differ in position of nanocrystals inside the material. However, the theory predicts that spectra should be similar, because it does not depend strongly on the position of the luminescence source. Properties of material depend mainly on the contrast of refraction index of voids and opal beads.

Reflection measurement of prepared photonic crystal reveals that structure is not homogeneous but contain parts with various crystalline quality. The crystalline quality determines the quality of the stop-band. The perfect stop-band at  $690 \text{ nm}$  (presented in [V]) in reflection spectra is used as a proof of quality of the structure in the direction perpendicular to the opal (111) plane. The nanocrystals incorporated inside opal have no influence on



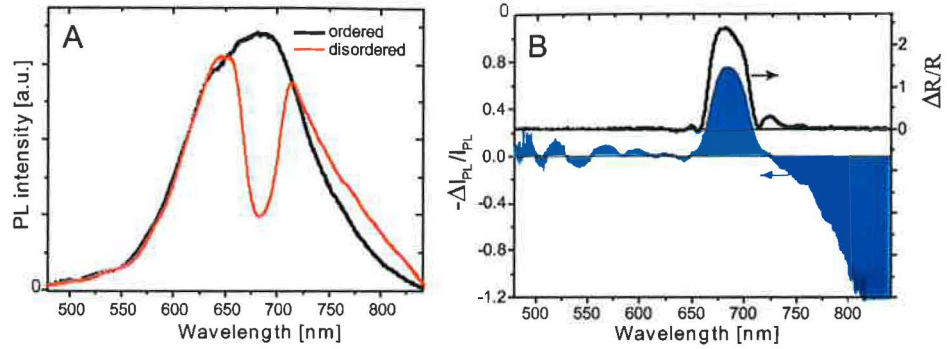


Figure 35: The photoluminescence spectra of the photonic crystal impregnated by the porous silicon in colloid. The black line is a bare opal and the red line is opal with incorporated silicon nanocrystals.

the position or shape of the stop-band. The variation depend only on the photonic crystal characteristics, mainly its quality.

The opals without silicon nanocrystals excited with UV-light show weak bluish photoluminescence. At the position of the stop-band the photoluminescence intensity is reduced up to 70%. The width at half-maximum is almost equal to the reflection band detected in reflection experiments on the same place of the sample.

The photoluminescence of photonic crystal with incorporated nanocrystals shows wide band typical for silicon nanocrystalline materials. The change of spectra is observed in the range where the stop-band of the photonic structure is present. The photoluminescence reduction in the stop-band depend on the type of sample. The photoluminescence depression in implanted sample is approximately 50% and in material with colloid impregnated into the opal the depression is observed to be more than 70% (Fig. 35). The lower depression in implanted samples could be due to the implantation profile, when is we consider 100 keV used in our case, only first two or three layers close to the surface are affected by the implantation. At the long wavelength of the photoluminescence spectrum increase of signal is observed. The absolute values of the photoluminescence from different places are not equal but this change is systematically observed to be considered as real. The change is proposed to be reabsorption of the photoluminescence from small nanocrystals by the larger nanocrystals and their reemission.

The photonic crystals show local variation of photoluminescence intensity. This effect was observed mainly on the implanted opals with homogeneous distribution of Si nanocrystals in contrast with opals impregnated by porous silicon colloids. The high spatial resolution necessary for this experiment needs detection system with high numerical aperture. Such type of detection system cause missing signature of stop-band because of the mixture of wide range of angles leaving the sample. These local changes of photoluminescence are most probably due to structural defects that break symmetry of structure [V].

## 6 Conclusion

### 6.1 Presented results

The current situation in material science shows tendency to the low dimensional structures. Especially silicon nanocrystalline light-emitting materials, topic of this thesis, are intensively studied as promising material for Si-based optoelectronics.

Three main types of nanocrystalline materials studied in this work are: porous silicon colloidal suspensions, nanocrystals embedded in a waveguide and photonic crystals. Each material has certain advantages for future development of commercial devices. In this thesis the attention was focused on optical properties of those materials.

Change of luminescence spectra according to the preparation conditions and matrix material was observed for all studied materials.

Colloids present changes of spectra connected with different solvent and sedimentation or filtering that cause blue shift of luminescence maxima. This form of silicon nanocrystals is interesting for possible single nanocrystal spectroscopy experiments. The single nanocrystal spectra are important to reveal properties of individual particle not observable in measurement of large ensemble of nanocrystals.

Implanted samples with the layer of silicon nanocrystals have interesting waveguiding properties with possible use in optoelectronics or photonics. An implantation energy and fluence determines the profile and the depth of the waveguide in the sample. Two theoretical models were presented. All our experiments support model of leaking substrate modes. Measured spectra are in excellent agreement with numerically calculated spectra.

The photoluminescence spectral profile is found to be significantly different when detected from the plane or the edge of a sample. Wide luminescence spectra (with a maximum around 780 nm) detected from the surface are similar to the inhomogeneously broadened luminescence signal commonly detected from Si nanocrystalline samples. On the other hand luminescence detected from the edge of the sample contains two sharp polarization resolved peaks. The reason for polarization modes splitting was explained by theoretical models to be due to different phase shifts of each polarization on waveguide boundaries. Because of large number of reflections, the shift can be easily observed. Polarization modes shift to longer wavelengths with increasing implantation dose.



The study of waveguiding properties shows possibility to couple and guide light inside the sample. Different principles of coupling are suggested by experiments with prism coupling through the upper interface and a directly coupled light through the sample edge.

The implanted silica glasses excited by a fs laser present small optical gain [56]. Our nonlinear experiment, pump-and-probe, gives promising results despite the fact that time resolution is poor. However, these nonlinear experiments were just pilot experiments and need more future study, to reveal and prove observed effects.

Two different photonic crystals with incorporated silicon nanocrystals were studied. The first structure was obtained by implantation of artificial opal structure with silicon ions and subsequent annealing (the nanocrystals are inside the beads). The second type of sample contains nanocrystals in form of colloid embedded in voids between the beads forming opal. The photoluminescence spectra present strong decrease of luminescence in range of the opal stop-band. The deeper spectral hole was obtained from samples with colloid in voids of the opal structure, the decrease of photoluminescence was more than 70%. The width of the stop-band was similar in reflection measurement as well as in decrease of photoluminescence. The spectral position of the stop-band depends on the periodicity of opal structure and the direction of light propagation in the structure and is not significantly influenced by the implanted or impregnated silicon nanocrystals.

## 6.2 Future development of nanocrystalline materials

The improvement of preparation of colloidal suspensions should be possible by developing efficient method to break large grains of porous silicon into sub-micron particles. The curvature of the small nanocrystal surface and the strain on interface affect the stability of O=Si bonds which are supposed to be involved in orange-red emission of Si nanocrystals. Colloids are interesting materials for studies by techniques of single nanocrystal spectroscopy. Such techniques could help to understand mechanisms of light emission in Si nanocrystals. Implanted silica glasses with narrow, polarized and directional luminescence, may be used in various photonic devices. The possible optical gain and nonlinear properties of such layers should be studied in future experiments to prove its possible use as an active medium for lasing. Direct writing of structures by a laser beam into the planar waveguide could produce photonic structures like resonators, gratings etc..

Photonic crystals present a new direction of silicon materials development. The directionality of refraction index in the material could be used for optical waveguides that guide signal in the structure with high refraction on the boundary and low losses inside. Advantage of this structure is also wavelength selection of such structure where only one wavelength is guided in one direction. Photonic crystal fiber has ability to steer light at sharp angles which is important for large variety of compact integrated optical devices. Future application of Si nanocrystals in real light-emitting devices requests an efficient electroluminescence. Such studies are performed in our Si nanostructures and by other groups [57] but were not the subject of this thesis.

Development described in previous paragraphs is motivated by the aim of all-silicon optoelectronics. After observation of luminescence, electroluminescence and also optical gain in nanocrystalline material, we could say that all silicon optoelectronic chip is feasible. However, now the question remains, which of many possible materials will be the best one, which material has the best properties and which will be the easiest to incorporate in present electronics. In real life, as happened many times in history, we can see that simple and cheap preparation can help material with even not the most optimal properties to become the most successful- it is not only a question of sufficient properties but also economy and timing.

The silicon as a material of high supply all over the world is a very promising material not only for optoelectronics and photonics, but also for other science branches like chemistry and medicine. Biosensing materials are another direction of possible future development. In presence, there are first results with porous silicon based materials for detection of various organic substances and in the following years we could expect many new inventions based on silicon nanomaterials. Even nanophotonic-based sensors utilizing multiple probes provide new possible advance.

Despite many open questions about nanocrystals, specific branches of industry already use advantages of nanocrystalline materials. Nanomaterials could be prepared from many various elements, not only silicon, but also from other semiconductors, metals etc. For example surface coatings, already in real application used special electrical, mechanical or optical properties of nanocrystalline materials. For example the automobile clearcoat "cerami-clear" containing 10-20 nm particles in 40 nm layer gives higher resistance against mechanical damage during cleaning. Nanomedicine is currently utilizing light-guided and light activated therapy. However, for the future ad-

vance in medicine applications, there is one important fact, which moderates use of new nanocrystalline materials in health care: their unknown biocompatibility and biotoxicity. Materials and devices used for therapy must be long-time tested for possible unexpected health effects.

## References

- [1] S. Ossicini, L. Pavesi, F. Priolo, *Light Emitting Silicon for Microelectronics*, Springer Tracts in Modern Physics 194, Springer, Berlin 2003
- [2] L. T. Canham; *Appl. Phys. Lett.*, 57, 1046 (1990)
- [3] M. Nayfeh, O. Akcakir, J. Therrien, Z. Yamani, N. Barry, W. Yu, and E. Gratton; *Appl. Phys. Lett.*, 75, 4112 (1999)
- [4] L. Pavesi, L. Dal Negro, G. Franzo, F. Priolo; *Nature*, 408, 440 (2000)
- [5] H. Rong, R. Jones, A. Liu, O. Cohen, D. Hak, A. Fang and M. Paniccia; *Nature*, 3346, 135552 (2005)
- [6] A. S. Davydov, *Kvantova mehanika*, Moskva 1973, 2. edition
- [7] L. E. Brus; *J. Chem. Phys.*, 80, 4403(1984)
- [8] Anders Gustafsson, Mats-Erik Pistol, Lars Montelius, and Lars Samuelson; *J. Appl. Phys.*, 84, 1715 (1998)
- [9] Albert Birner, Ralf B. Wehrspohn, Ulrich M. Gsele, and Kurt Busch; *Adv. Mater.*, 13, 377 (2001)
- [10] B. E. A. Saleh, M. C. Teich, *Fundamentals of photonics*, part 3, John Wiley & Sons, New York, 1991
- [11] U. Woggon, *Optical properties of semiconductor Quantum Dots*, Springer-Verlag, Berlin, 1997
- [12] M. Wolkin, J. Journe, P. M. Fauchet, G. Allan, and C. Delerue; *Phys. Rev. Lett.*, 82, 197 (1999)
- [13] D. Kovalev, H. Heckler, G. Polisski, and F. Koch; *Phys. Stat. Sol.*, 215, 871 (1999)
- [14] O. Wind, F. Gindele, U. Woggon, C. Klingshirn; *J. Crystal Growth* 159, 867 (1996)
- [15] B. E. A. Saleh, M. C. Teich, *Fundamentals of photonics*, part 2, John Wiley & Sons, New York, 1991

- [16] S. P. Parker; Optics source book, McGraw-Hill, New York 1988
- [17] S. V. Gaponenko; Optical properties of semiconductor nanocrystals, Cambridge University Press, 1998
- [18] N. S. Kapany and J. J. Burke, Optical waveguides, Academic press, New York 1972
- [19] Yu. A. Vlasov, V. N. Astratov, A. V. Baryshev, A. A. Kaplyanskii, O. Z. Karimov, and M. F. Limonov; Phys. Rev. E, 61, 5784 (2000)
- [20] Paras N. Prasad, Nanophotonics, John Wiley & Sons, New Jersey, 2004
- [21] Hari Sing Nalwa, Handbook of nanostructured materials and nanotechnology - Volume 1, Academic Press, San Diego 2000
- [22] J. Valenta, R. Juhasz, J. Linnros; Appl. Phys. Lett., 80, 1070 (2002)
- [23] A. G. Cullis, L. T. Canham and P. D. J. Calcott; J. Appl. Phys., 82, 909 (1997)
- [24] J. D. Holmes, K. J. Ziegler, R. C. Doty, L. E. Pell, K. P. Johnston, and B. A. Korgel; J. Am. Chem. Soc., 123, 3743 (2001)
- [25] R. Smirani et al.; J. Lumin., 115, 62 (2005)
- [26] Serincan U, Yerci S, Kulakci M, et al.; Nucl. Instrum. Meth. B, 239, 419 (2005)
- [27] P. Pellegrino et al.; J. Appl. Phys. 97, 74312 (2005)
- [28] L. Khriachtchev, M. Räsänen, S. Novikov; Appl. Phys. Lett., 83, 3019 (2003)
- [29] S. Cheylan and R. G. Elliman; Appl. Phys. Lett., 78, 1225 (2001)
- [30] A. R. Wilkinson, R. G. Elliman; Appl. Phys. Lett., 83, 909 (2003)
- [31] J. Linnros, N. Lalic, A. Galecks and V. Grickas; J. Appl. Phys., 86, 6128 (1999)
- [32] E. Yablonovitch; Phys. Rev. Lett., 58, 2059 (1987)

- [33] S. John; *Phys. Rev. Lett.*, 58, 2486 (1987)
- [34] O. E. Rogach, A. Kornowski, A. M. Kapitonov, N. V. , S. V. Gaponenko, A. Eychmüller, A. L. Rogach; *Mat. Sci. Eng. B*, 64, 64 (1999)
- [35] Peigen Ni, Peng Dong, Bingying Cheng, Xinyan Li, and Daozhong Zhang; *Adv. Mater.*, 13, 437 (2001)
- [36] David J. Norris and Yurii A. Vlasov; *Adv. Matter.*, 6, 371 (2001)
- [37] Henry P. Schriemer, Henry M. van Driel, A. Femius Koenderink, and Willem L. Vos; *Phys. Rev. A*, 63, 11801 (2000)
- [38] E. P. Petrov, V. N. Bogomolov, I. I. Kalosha, and S. V. Gaponenko; *Phys. Rev. Lett.* 81, 77 (1998)
- [39] J. Valenta, J. Linnros, R. Juhasz, J.-L. Rehspringer, F. Huber, C. Hirliemann, S. Cheylan, R. G. Elliman; *J. Appl. Phys.*, 93, 4471 (2003)
- [40] M. Ajgaonkar, Y. Zhang, H. Grebel, and C. W. White; *Appl. Phys. Lett.*, 75, 1532 (1999)
- [41] J. Valenta, I. Pelant, J. Linnros; *Appl. Phys. Lett.*, 81, 1396 (2002)
- [42] G. Viera, S. Huet, L. Boufendi; *J. Appl. Phys.*, 90, 4175 (2001)
- [43] Jian Zi, H. Büscher, C. Falter, W. Ludwig, K. Zhang and Xide Xie; *Appl. Phys. Lett.*, 69, 201 (1996)
- [44] Soumyendu Guha; *J. Appl. Phys.*, 84, 5211 (1998)
- [45] Khriachtchev, M. Räsänen, S. Novikov, J. Lahtinen; *J. Appl. Phys.*, Vol. 95, 7593 (2004)
- [46] J. Valenta, I. Pelant, K. Luterova, R. Tomasiunas, S. Cheylan, R. G. Elliman, J. Linnros; *Appl. Phys. Lett.*, 82, 955 (2003)
- [47] R. G. Elliman, M. J. Lederer, N. Smith, B. Luther-Davies; *Nucl. Inst. and..*, 206, 427 (2003)
- [48] M. Ezaki, H. Kumagai, K. Toyoda, and M. Obara; *IEEE J. Select. Top. Quantum Electron.* 1, 841 (1995)

- [49] I. Pelant, T. Ostatnicky, J. Valenta, K. Luterova, E. Skopalova, T. Mates, R. G. Elliman; *Appl. Phys. B*, 83, 87 (2006)
- [50] T. Ostatnicky, J. Valenta, I. Pelant, K. Luterova, R. G. Elliman, S. Chelyan, B. Hönerlage; *Opt. Mat.*, 27, 781 (2005)
- [51] K. T. Shimizu, W. K. Woo, B. R. Fisher, H. J. Eisler, and M. G. Bawendi; *Phys. Rev. Lett.*, 89, 117401 (2002)
- [52] D. S. English, L. E. Pell, Z. Yu, P. F. Barbara, and B. A. Korgel; *Nano Letters* 2, 681 (2002)
- [53] Khriachtchev, M. Räsänen, S. Novikov, J. Sinkkonen; *Appl. Phys. Lett.*, 79, 1249 (2001)
- [54] J. Valenta, T. Ostatnicky, I. Pelant, R. G. Elliman, J. Linnros, B. Hönerlage; *J. Appl. Phys.*, 96, 5222 (2004)
- [55] B. V. Kamenev, H. Grebel, and L. Tsybeskov; *Appl. Phys. Lett.*, 88, 143117 (2006)
- [56] K. Luterova, M. Cazzanelli, J.-P. Likoforman, D. Navarro, J. Valenta, T. Ostatnicky, K. Dohnalova, S. Cheylan, P. Gilliot, B. Hönerlage, L. Pavesi, I. Pelant; *Opt. Mater.*, 27, 750 (2005)
- [57] A. Irrera, D. Pacifici, M. Miritello, G. Franzo, F. Priolo, F. Iacona, D. Sanfilippo, G. Di Stefano, P. G. Fallica; *Appl. Phys. Lett.*, 81, 1866 (2002)

## A Published results

- I. Colloidal suspensions of silicon nanocrystals: From single nanocrystals to photonic structures; J. Valenta, P. Janda, K. Dohnalová, D. Nižňanský, F. Vácha, and J. Linnros; *Optical Materials*, Volume 27, February 2005, Pages 1046-1049
- II. Light propagation in planar optical waveguides made of silicon nanocrystals buried in silica glass; P. Janda, J. Valenta, T. Ostatnický, I. Pelant, R.G. Elliman; *Thin solid films*, 515, 797(2006)
- III. Silicon nanocrystals in silica Novel active waveguides for nanophotonics; P. Janda, J. Valenta, T. Ostatnický, E. Skopalová, I. Pelant, R.G. Elliman, R. Tomasiunas; *Journal of Luminescence*, 121, 267(2006)
- IV. Optical gain in planar waveguides; T. Ostatnický, J. Valenta, P. Janda, I. Pelant; *SPIE Proceedings* (in press) of XV Czech-Polish-Slovak optical conference, September 11-15, 2006, Liberec, Czech republic
- V. Modified spontaneous emission of silicon nanocrystals embedded in artificial opals; P. Janda, J. Valenta, J.-L. Rehspringer, R.R. Mafouana, J. Linnros, R.G. Elliman; article sent in February 2007 to *Applied Physics B*



I

Colloidal suspensions of silicon nanocrystals:  
From single nanocrystals to photonic structures

J. Valenta et al.  
Optical Materials  
October 2004



## Colloidal suspensions of silicon nanocrystals: from single nanocrystals to photonic structures

J. Valenta <sup>a,d,\*</sup>, P. Janda <sup>a</sup>, K. Dohnalová <sup>b</sup>, D. Nižňansky <sup>c</sup>, F. Vácha <sup>d,e</sup>, J. Linnros <sup>f</sup>

<sup>a</sup> Department of Chemical Physics and Optics, Faculty of Mathematics and Physics, Charles University, Ke Karlovu 3, CZ-121 16 Prague 2, Czech Republic

<sup>b</sup> Institute of Physics, Academy of Sciences of the Czech Republic, CZ-162 53 Prague 6, Czech Republic

<sup>c</sup> Faculty of Sciences, Department of Inorganic Chemistry, Charles University, CZ-128 43 Prague, Czech Republic

<sup>d</sup> Institute of Physical Biology, University of South Bohemia, CZ-370 05 Budweis, Czech Republic

<sup>e</sup> Institute of Plant Molecular Biology, Academy of Sciences of the Czech Republic, CZ-370 05 Budweis, Czech Republic

<sup>f</sup> Department of Microelectronics and Information Technology, Royal Institute of Technology, S-164 21 Kista, Sweden

Available online 18 October 2004

### Abstract

Colloidal suspensions of Si nanocrystals (NCs) are prepared from light-emitting porous Si grains obtained by mechanical pulverization of electrochemically etched layers. Sedimented and/or filtered Si NCs sols reveal a green photoluminescence (PL) band around 530 nm, which is interpreted as radiative recombination of electron–hole pairs inside Si NCs with diameter about 2 nm. These colloidal solutions have multiple advantages for both fundamental investigations and for nanotechnology. In one extreme, single molecule spectroscopy techniques can be applied to investigate PL of single grains of Si NCs dispersed on substrates from highly diluted solutions. On the other hand, concentrated suspensions enable us to fabricate bulk samples with embedded Si NCs or to prepare self-organised nanostructures on surfaces.

© 2004 Elsevier B.V. All rights reserved.

### 1. Introduction

Among many techniques to prepare silicon nanocrystals (Si NCs), electrochemical etching of porous Si remains the cheapest and fastest method. It may be the most promising for production of large amounts of Si NCs required for potential applications in nanotechnology.

In this paper we investigate properties and technological prospects of colloidal suspensions formed by dispersing a Si NCs sol (from pulverized porous Si layers) in different organic solvents. Special attention is paid to a surprising observation of intense green photoluminescence (PL) in sedimented and/or filtered suspensions.

### 2. Sample preparation and experimental techniques

Porous Si (PSi) powder has been prepared by standard electrochemical etching of Si wafers ((100)p-type,  $\rho \sim 0.1 \Omega \text{cm}$ ) in a HF-ethanol (1:2.5) solution. The etching current density was kept relatively low ( $1.6 \text{ mA/cm}^2$ ) in order to obtain higher porosity and, consequently, resulting in a low mean size of Si-NC (the PL band peak is around 680 nm). PSi powder (i.e. grains of interconnected oxidized Si NCs) is then obtained by mechanical pulverization of the PSi film from the silicon substrate. Such a powder (showing intense orange PL under UV excitation) is a starting material for production of various Si nanostructures through colloidal phase—see schematic illustration in Fig. 1.

Colloidal suspensions were prepared by pouring different organic solvents (ethanol, isobutanol, heptanol, hexane, heptane) onto the PSi powder and mixing with

\* Corresponding author. Fax: +420 2 21 91 12 49.

E-mail address: [jan.valenta@mff.cuni.cz](mailto:jan.valenta@mff.cuni.cz) (J. Valenta).

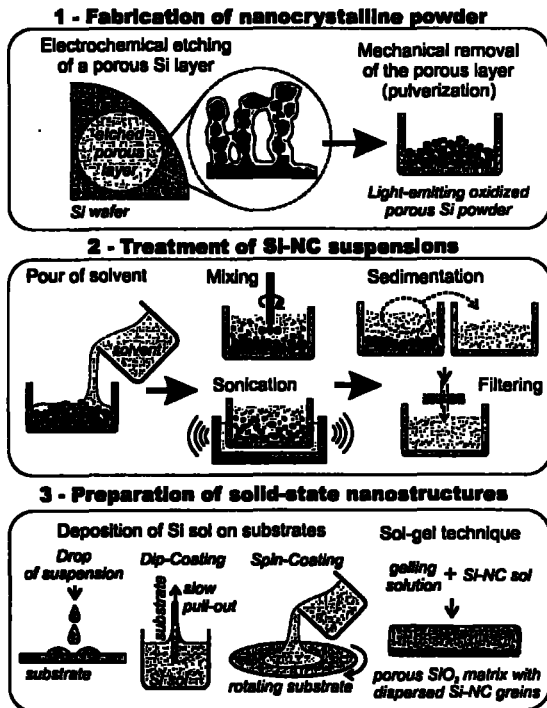


Fig. 1. Schematic illustration of the fabrication procedure of Si nanostructures from PSi powder through colloidal suspensions. See text for details.

a small propeller (Ultra-turrax) and in ultrasonic bath. Microscopical observation shows that the original powder contains many large PSi grains of several  $\mu\text{m}$  or even tens of  $\mu\text{m}$ . The mixing is breaking the largest grains but it is inefficient to decrease their size below a few  $\mu\text{m}$ . Further size selection is possible by repeated sedimentation or centrifugation. Some suspensions were filtered by teflon membranes (Sartorius) with pores of 200 nm.

Colloidal suspensions can be used to prepare Si NCs structures of various forms. For studying individual Si NC particles we deposit highly diluted suspensions onto cleaned substrates (Si wafers, glass or fused silica plates) by means of spin- or dip-coating techniques. On the other hand, concentrated suspension can form interesting self-organised structures when deposited under appropriate combination of solvent and substrate.

Solid-state samples with high concentration of Si NCs are formed by dispersing PSi powder into the commercially available SiO<sub>2</sub>-based undoped or doped spin-on-glasses [1]. The solution solidifies at room temperature and atmosphere within a few hours. At the first stage of the solidification, the samples are kept in ultrasonic bath for 1 h to avoid agglomeration. During the next step, the Si NCs are sedimenting on the bottom of the cell creating  $\sim 50\mu\text{m}$  thick layer containing densely packed Si NCs. The solidified samples of typical

dimensions  $10 \times 10 \times 1\text{mm}^3$  with a wide range (3–45 vol.%) of Si NCs concentrations were prepared.

PL spectra were measured under excitation by a cw Ar-ion laser (emission lines from 457 nm to 514 nm) and detected with Pentamax ICCD camera connected to an imaging spectrometer (Jobin-Yvon Triax 320). PL excitation spectra were measured with a fluorescence spectrometer (FluoroLog 2, excitation with monochromatized continuous Xe lamp). PL kinetics were excited by nanosecond pulses of a XeCl excimer laser (30 ns, 5 Hz,  $\lambda = 308\text{nm}$ ), emission was spectrally selected with narrow band interference filters, and detected by a Hamamatsu R928 photomultiplier connected to an oscilloscope. Raman scattering of the suspensions was detected by the LabRam spectrometer using a macro-lens and by excitation with the 532 nm output of a cw YAG laser. Micro-PL images were studied using an imaging spectrometer (Triax 190) connected to an optical microscope Nikon Optiphot 120. Light from the sample was collected by an objective lens (100 $\times$ /0.73 NA), imaged onto the entrance slit of a spectrometer and detected by a LN-cooled CCD camera Hamamatsu C 4880. An unfocused UV line (325 nm) of a cw He-Cd laser was used as excitation source.

### 3. Experimental results and discussion

The prepared suspensions of Si NCs are yellowish, light diffusive liquids in which sedimentation of  $\mu\text{m}$  sized grains occur on a time scale of hours (depending on specific density and viscosity of solvent). They show strong orange PL (peaking around 640 nm, with small shifts depending on applied solvent) under UV or blue excitation (see Fig. 2a). After filtering (filter pore size 0.2  $\mu\text{m}$ ) the suspensions lost its yellow colour and became clear colourless, this means most likely that the majority of

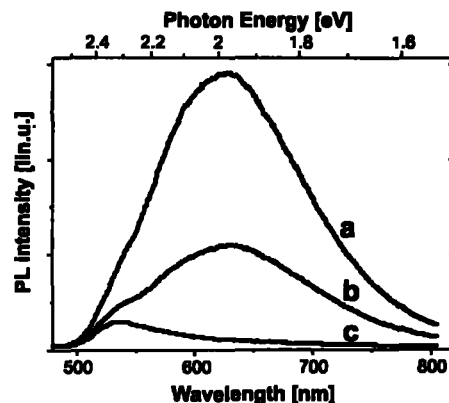


Fig. 2. PL spectra of a Si NCs suspension in ethanol (excitation by 457 nm line of Ar-laser): (a) freshly shaken colloid, (b) 1 h sedimented colloid and (c) filtered colloid.

PSi grains was lost in the filter and possibly only very small Si NCs grains remained in the colloid. The presence of Si NCs is indeed proved by absorption spectroscopy (the continuous absorption spectrum typical for Si NCs is observed slightly blue-shifted compared to non-filtered suspensions) and Raman spectroscopy which indicates Si NCs of mean diameter around 2 nm in both filtered and non-filtered suspensions.

The most peculiar observation in filtered or well-sedimented colloidal suspensions is a green photoluminescence. In Fig. 2 we show how the otherwise hidden green PL band becomes apparent when large grains of PSi go away by sedimentation or more efficiently by filtering. The effect is observed for all solvents used in this study. It is repeatable and not related to the solvent itself (no such PL signal is observed in pure solvents under the same experimental conditions).

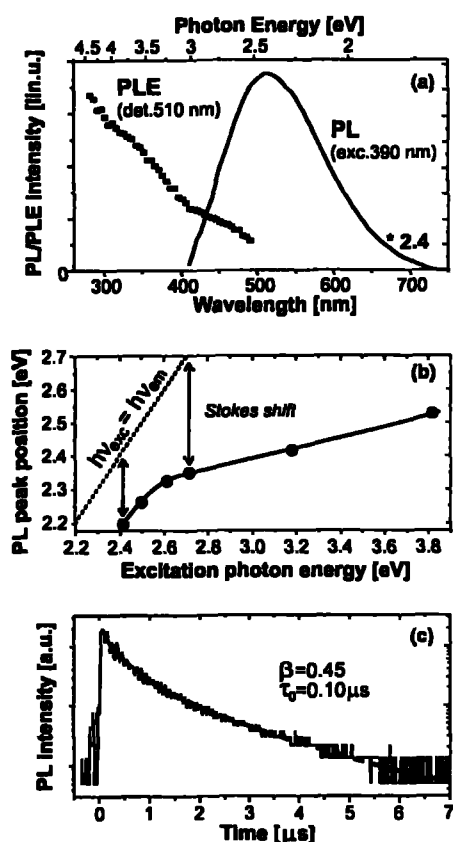


Fig. 3. PL characteristics of a filtered suspension of Si NCs in heptane: (a) PL emission (solid line) excited by a filtered Xe lamp at 390 nm and PL excitation (black dots) detected at 510 nm. (b) PL peak position as a function of excitation photon energy, the Stokes shifts are indicated. (c) Kinetics of PL (at 550 nm) decay after nanosecond pulse excitation (by XeCl excimer laser: 308 nm, 60 kW/cm<sup>2</sup>, 5 Hz). The experimental curve (black line) is fitted by a stretch exponential function with parameters  $\beta = 0.45$  and  $\tau_0 = 0.10 \mu$ s.

The main characteristics of the green PL are summarised in Fig. 3 for Si NCs suspension in heptane. The PL excitation spectrum (Fig. 3a) has no evident resonances and resembles results obtained in other Si nanocrystalline structures (e.g. [2,3]). The green PL peak position (Fig. 3b) shifts with excitation wavelength and the Stokes shift becomes smaller for longer excitation wavelength—such behaviour is typical for an inhomogeneously broadened peak. The kinetics of the PL decay (Fig. 3c) is rather fast—time constant around 0.1  $\mu$ s—compared to the orange PL band of Si NCs (tens of  $\mu$ s [3]) but it has the same typical non-exponential shape often modelled by a stretch-exponential function.

What is the mechanism of the green PL? When adopting the model of Wolkin et al. [4] the above described experimental characteristics suggest that the green PL is connected with the presence of small Si NCs (diameter of about 2 nm) in which Si=O surface centres (responsible for orange PL) are no more affecting radiative recombination of electron-hole pairs in the core of NCs. We have to mention that there are several well-described observations of green (or even blue) PL of Si nanocrystals in the literature, e.g. in porous Si [2,4], Si colloids made by gas evaporation [5], Si NCs synthesized in inverse micelles [6] or in sterically stabilized Si NCs made by thermal degradation of diphenylsilane [7].

The reason why surface traps are not effective in our small Si grains has to be investigated in the future. Here we can speculate that the surface of very small Si NCs (not stacked in large aggregates) get relaxed in a colloidal suspension. Consequently the Si=O bonds, which are stable only under stress in the silicon-silica interface, are replaced by ordinary Si-O-Si or Si-OH bonds. Also carbon chains of solvent molecules can take part in passivation of the surface bonds of Si NCs, very much like sterical stabilization described by Holmes et al. [7]. The advantage of such green-light emitting Si NCs is that the emission rate is much higher than for those emitting orange PL and therefore they are more favourable for construction of optoelectronic devices.

The green PL emission of the Si NCs can be studied by means of single quantum dot spectroscopy by dispersing a diluted suspension of Si NCs on ultra-clean substrates (see Fig. 4a). The green emission remains stable even after evaporation of the solvent. Our single Si NCs experiments were described in [8]. The main observation that proves the single nanocrystal origin of the observed PL emission is an intermittence effect (ON-OFF blinking) and a high value of the fluorescence auto-correlation function. The single Si NC spectra have asymmetrically-enlarged shape to lower energies with a possible low-energy sub-band 120 meV below the main peak. Similar single Si NC spectra were observed by English et al. [9] and the sub-band was explained as a Si-O-Si vibrational feature.

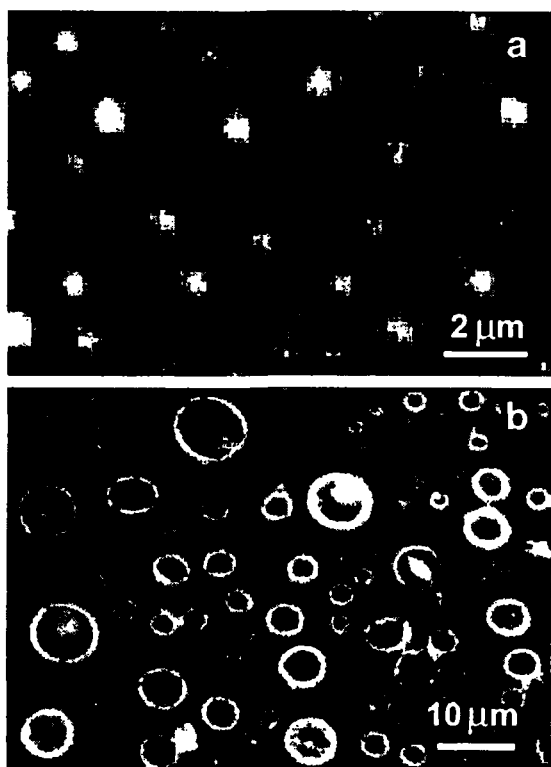


Fig. 4. Micro-PL images (objective lens  $100\times/0.73$ , excitation 325 nm) of Si NCs deposited from isobutanol colloidal suspension on a cleaned fused silica substrate: (a) Dispersed individual Si NC particles from highly diluted suspension (the size of emitting dots corresponds to the diffraction limited spots), (b) Self-organised ring resonators from deposition of concentrated suspension. (Optical resolution of the imaging system is about  $0.5\mu\text{m}$ .)

Si NCs in colloidal suspensions can be used as building blocks of various interesting photonic structures. Here we show for example micron-sized ring resonators (Fig. 4b) formed by self-assembly during evaporation of isobutanol suspension deposited onto a clean fused silica substrate. Under optimal conditions almost perfect resonators are formed in which spectral narrowing due to resonance effects is observed. For example the most intense ring in Fig. 4b has a PL spectrum almost three times narrower and more than twice as intense as the PL outside the resonator ring (details will be published separately). Other examples of interesting structures are highly concentrated layers of Si NCs formed in a porous  $\text{SiO}_2$  matrix by mixing PSi powder with commercially available spin-on-glass. This sol-gel method creates samples with exceptionally high concentrations of Si NCs (up to 45 vol.%) in which optical gain was observed [10]. A disadvantage of the sol-gel structures is inhomogeneity, which causes diffusion of propagating light.

#### 4. Conclusions

Production of colloidal suspensions of Si NCs from pulverized porous Si layers presents an inexpensive and fast way to produce important amounts of light-emitting Si-based nanomaterial. It can be used as building blocks of various nanostructures with promising optoelectronic applications. Moreover, an interesting blue-shift of the PL from the orange to the green spectral region is easily achieved in these materials.

There are however many technological aspects to improve. In particular, an efficient method to break the micrometer-sized grains of PSi into sub-micron parts has to be found. One possible way to be investigated is exploitation of spontaneous or induced charging of Si grains in colloids [11].

Further development of chemistry and physics of colloidal silicon materials is important not only from the point of view of Si-based optoelectronics but also for possible application of bio-compatible and bio-degradable Si nanostructures in bio-nanomaterials.

#### Acknowledgements

This work was supported by GACR (202/03/0789), GA AVCR (IAA1010316 and IAA1010413) and the Ministry of Education CR (projects LNOOA141 and ME 486). Partial funding was received from the Swedish Research Council (VR) and the Royal Swedish Academy of Sciences. One of the authors (JV) thanks J. Buršík and V. Machovič for technical assistance.

#### References

- [1] V. Švrček, A. Slaoui, J.C. Muller, *J. Appl. Phys.* **95** (2004) 3158.
- [2] A. Kux, M. Ben Chorin, *Thin Solid Films* **276** (1996) 272.
- [3] J. Valenta, J. Dian, K. Luterová, P. Knápek, I. Pelant, M. Nikl, D. Müller, J.J. Grob, J.-L. Rehspringer, B. Hönerlage, *Eur. Phys. J. D* **8** (2000) 395.
- [4] M.V. Wolkin, J. Jorne, P.M. Fauchet, G. Allan, C. Delerue, *Phys. Rev. Lett.* **82** (1999) 197.
- [5] K. Kimura, S. Iwasaki, *Jpn. J. Appl. Phys.* **38** (1999) 609.
- [6] J.P. Wilcoxon, G.A. Samara, P.N. Provencio, *Phys. Rev. B* **60** (1999) 2704.
- [7] J.D. Holmes, K.J. Ziegler, R.Ch. Doty, L.E. Pell, K.P. Johnston, B.A. Korgel, *J. Am. Chem. Soc.* **123** (2001) 3743.
- [8] J. Valenta, J. Linnros, R. Juhasz, F. Cichos, J. Martin, in: L. Pavesi, et al. (Eds.), *Towards the First Silicon Laser*, Kluwer Academic Publishers, 2003, p. 89.
- [9] D.S. English, L.E. Pell, Z. Yu, P.P. Barbara, B.A. Korgel, *Nano Lett.* **2** (2002) 681.
- [10] K. Luterová, K. Dohnalová, V. Švrček, I. Pelant, J.-P. Likforman, O. Crégut, P. Gilliot, B. Hönerlage, *Appl. Phys. Lett.* **84** (2004) 3280.
- [11] A. Fojtik, A. Henglein, *Chem. Phys. Lett.* **221** (1994) 363.

II

Light propagation in planar optical waveguides  
made of silicon nanocrystals buried in silica glass

P. Janda et al.  
Thin solid films  
January 2006



## Light propagation in planar optical waveguides made of silicon nanocrystals buried in silica glass

P. Janda<sup>a</sup>, J. Valenta<sup>a,\*</sup>, T. Ostatnický<sup>a</sup>, I. Pelant<sup>b</sup>, R.G. Elliman<sup>c</sup>

<sup>a</sup> Department of Chemical Physics and Optics, Faculty of Mathematics and Physics, Charles University, Ke Karlovu 3, CZ-121 16 Prague 2, Czech Republic

<sup>b</sup> Institute of Physics, Academy of Sciences of the Czech Republic, Prague, Czech Republic

<sup>c</sup> Electronic Materials Engineering Department, Research School of Physical Sciences and Engineering, Australian National University, Canberra, Australia

Available online 30 January 2006

### Abstract

Silicon nanocrystals fabricated by Si<sup>+</sup>-ion implantation (400 keV, fluences from 4 to 6 × 10<sup>17</sup> cm<sup>-2</sup>) of fused silica form interesting active planar optical waveguides. The nanocrystals emit orange-red photoluminescence (PL) (under UV-blue excitation) and define a region of high refractive index that guides part of the PL along the layer. Light from external light sources can also be coupled into the waveguides (directly to the polished edge facet or from the surface by applying a quartz prism coupler). In both cases the optical emission from the sample facet exhibits narrow (10–20 nm full-width-at-half-maximum) polarisation-resolved transverse electric and transverse magnetic modes instead of the usual broad nanocrystal spectra. This effect is explained by our theoretical model, which identifies the microcavity-like peaks as leaky modes propagating along the waveguide/substrate boundary (not the usual modes guided inside the nanocrystal plane due to its graded index profile). The unconventional properties of this relatively easy-to-make all-silicon structure may be interesting for future photonic devices and sensors.

© 2005 Elsevier B.V. All rights reserved.

PACS: 78.67.Bf; 42.79.gn; 81.07.Bc

Keywords: Nanocrystals; Waveguide; Silicon

### 1. Introduction

Research in silicon-based photonics aims to create integrated electronic and photonic functionality in a single silicon chip. Silicon nanocrystals (Si-NCs) are an important building block for such photonic circuits as they are efficient light emitters [1] and their assemblies can be used to form active optical waveguides [2]. For example, it was recently shown that Si-NC waveguides, with properly designed refractive index profile, exhibit spectral filtering and pronounced polarization of the Si-NC photoluminescence (PL) emission [3,4]. This unexpected effect was shown by our group to be due to leaky modes of the lossy planar waveguides [5]. In this paper we compare the propagation of PL excited inside the waveguide with that of light coupled from external sources.

### 2. Sample preparation and experimental techniques

The Si-NC waveguides were prepared by 400 keV Si<sup>+</sup>-ion implantation into optically polished Infrasil slabs with fluences of 4.0, 4.5, 5.0, 5.5, and 6.0 × 10<sup>17</sup> cm<sup>-2</sup>. Samples were subsequently annealed for 1 h at 1100 °C in a N<sub>2</sub> ambient to form Si-NCs and further annealed for 1 h at 500 °C in forming gas (N<sub>2</sub>/H<sub>2</sub>) to enhance the PL. The diameter of Si-NCs was estimated from Raman scattering spectra to be about 5 nm [6]. The implanted layer buried in a silica slab acts as a planar asymmetrical optical waveguide. Refraction index profiles were estimated from SRIM (the Stopping and Range of Ions in Matter [7]) calculations of implantation profiles and from modelling of VIS–IR transmission fringes [5] (the peak refraction index increases from 1.75 to 2 with increasing implantation dose). The profiles are asymmetric Gaussians with a peak around 600 nm below surface and a full-width at half-maximum of about 300 nm.

Photoluminescence was measured at room temperature under excitation with an Ar-ion laser (458 nm) or He–Cd

\* Corresponding author. Tel.: +42 2 21911272; fax: +42 2 21911249.

E-mail address: [jan.valenta@mff.cuni.cz](mailto:jan.valenta@mff.cuni.cz) (J. Valenta).

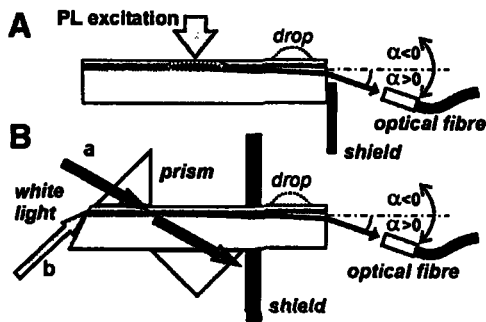


Fig. 1. Schematics of experimental set-ups: (A) PL measurements, (B) external source coupling through a prism (a) or directly through the facet (b).

laser (325 or 442 nm) and detected with an imaging spectrograph (Jobin–Yvon Triax 320) coupled to an i-CCD camera (Princeton Instruments PI-MAX). All spectra were corrected for the experimental system response. Light coming from the sample was collected by a quartz fibre (mounted on a goniometer) and imaged on the spectrograph input, the collection angle being of about  $1^\circ$  (see Fig. 1A). For comparison we coupled external light sources (Xe lamp, halogen lamp or white LED) to the waveguide either through a quartz prism or directly through the polished edge of the sample (arrows *a* and *b*, respectively, in Fig. 1B). A black shield and a prism on the bottom of the sample eliminated direct detection of light and reflections from the sample interface, respectively.

### 3. Experimental results

PL measurement of the samples under UV excitation at about  $45^\circ$  and with signal collection perpendicular to the layer shows a wide PL band centred around 850 nm which is almost equal for all implantation fluences (upper spectra in Fig. 2A). Such broad-band spectra are typical of the inhomogeneously broadened emission from Si-NCs. In contrast, the PL spectra collected from the edge of the sample or for angles of a few degrees below the plane of the waveguide ( $\alpha > 0$  in Fig. 1), reveal pronounced spectral filtering and polarization. The “facet” spectra are composed of two distinct peaks separated by about 30 nm, which are systematically red-shifted with increasing implantation fluence (lower spectra in Fig. 2A). The short-wavelength peak has linear polarization parallel to the Si-NCs layer (TE-polarization) while the long-wavelength one has polarization perpendicular to the film (TM-polarization) (see Fig. 2B).

The external-light coupling experiments using a quartz prism show the best transmission in the “facet” direction or slightly below ( $\alpha \sim 7^\circ$ ). The transmission spectra consist of two broad bands (Fig. 3A) with a small degree of polarization. The spectral positions of the long-wavelength bands agree with the luminescence TE and TM peaks of respective layers. The coupling of light directly through the polished facet is more delicate but is also possible. Fig. 3B compares the two coupling methods for the sample implanted with fluence of  $5.5 \times 10^{17}$

$\text{cm}^{-2}$ . The direct coupling gives much narrower absorption peaks with distinct TE and TM resolution.

### 4. Discussion of the guiding mechanism

Two different mechanisms were proposed to explain this novel guiding behaviour:

- (i) The linearly polarized PL peaks could simply result from standard guided modes of the planar waveguide. However, an ideal transparent planar waveguide should transmit a continuous spectrum of guided modes up to a cut-off wavelength [8], which is estimated to lie above  $\sim 1500$  nm for the first order modes in our waveguides. Some spectral structure might arise from wavelength dependent losses, with those modes (wavelengths) that undergo the smallest loss being guided to the edge of the sample. These are likely those modes that are “weakly guided”, i.e. the modes whose electric field is strongly delocalized and the modes that propagate basically as a planar wave in the substrate [3,8]. Their effective guide thickness approaches infinity. Ray optics describes these modes by an angle of incidence  $\theta$  that is *greater than* but very close to the critical angle  $\theta_c$  for total internal reflection. The salient feature of the filtering, namely, the

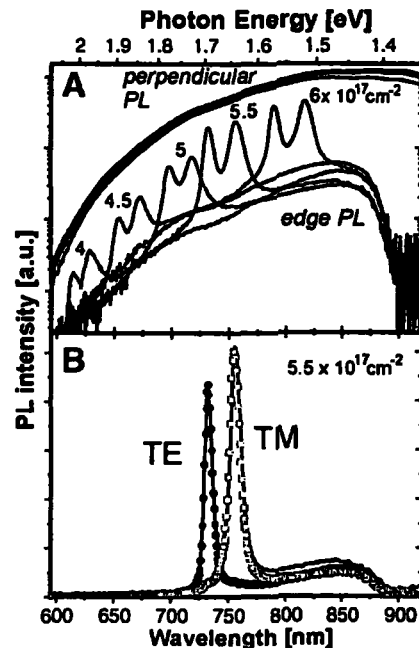


Fig. 2. (A) PL spectra of layers implanted with fluences of  $4$  to  $6 \times 10^{17} \text{ cm}^{-2}$ . The upper spectra are taken perpendicular to the plane of waveguide layer, while the lower spectra are taken from the facet at angle of  $7^\circ$ . The TE/TM peaks shift to longer wavelength with increasing implantation fluence. (Note the log scale of PL intensity). (B) Polarization resolved PL spectra of the sample  $5.5 \times 10^{17} \text{ cm}^{-2}$  taken for angle  $7^\circ$ . TE and TM peaks (black dots and open squares, respectively) are linearly polarized parallel or perpendicular to the implanted layer, respectively.



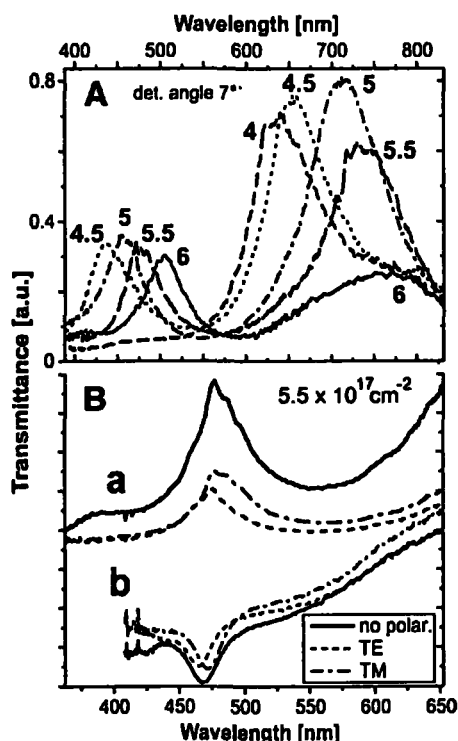


Fig. 3. (A) Transmission spectra for white light coupled to the waveguides through the quartz prism placed on the upper surface of waveguide. Detection angle was  $7^\circ$ . The two spectral bands are systematically red-shifted with increasing implantation fluence. (B) Comparison of short-wavelength transmission peak for prism-coupling (a) and transmission dip for direct coupling through the facet (b). The TE and TM polarizations are represented by dash and dot-dash lines, respectively.

separation between TE and TM modes, is a direct consequence of the asymmetric guide — different phase shifts  $\Phi$  for the TE and TM modes under total reflection at both boundaries. In order to fulfill the phase condition that after two successive reflections the phase difference can only be equal to integral multiple of  $2\pi$ , suitable wavelengths from the emission band are combined with available values of  $\Phi$ . Since the latter are slightly different for TE and TM polarizations at a given angle of incidence, the resulting mode wavelengths are also slightly different.

- (ii) The second possible mechanism involves substrate leaky (or radiation) modes of the Si-NCs waveguide [5,9]. These modes propagate at angle  $\theta$  situated close to but below  $\theta_c$ , undergo total reflection at the upper boundary Si-NCs/air (larger index difference) but are only partially reflected on the lower boundary Si-NCs/substrate (smaller index difference). Consequently, a small fraction of their power is radiated into the substrate at each bottom reflection. If the angle  $\theta$  is only slightly less than  $\theta_c$ , the leaky modes propagate nearly parallel to the Si-NCs plane. Moreover, the number of reflections is very high (reflectance is close to unity), resulting in a narrow spectral width of the modes. The mechanism of spectral

filtering in this case remains basically the same as discussed above, the only difference being that a phase shift  $\Phi$  at the upper boundary only comes in to play during the initial stages of propagation. After a finite number of internal reflections all the radiant power escapes into leaky modes and emerges from the sample facet in a well-defined direction, basically parallel to the Si-NCs film. This makes such leaky substrate modes virtually indistinguishable from the guided modes.

In our previous papers [5,6] we proved the validity of the leaky-mode model by numerical calculations and by experiment where drops of different liquids were placed on the surface above the excited spot or between the spot and the edge. In the first case the “facet” PL spectrum changes significantly depending on the refractive index of the liquid, while there are no changes with drops located some distance from the excited spot.

The prism-coupled transmission spectrum is broad with weak polarization dependence (Fig. 3A) because the number of reflections is very low and the waveguide becomes more symmetrical as the upper boundary is covered by the quartz prism (with an immersion oil). On the other hand, direct coupling through the facet reveals maxima of the absorption spectrum at the similar position as maxima of the transmission spectrum of the prism-coupled light. Properties of absorption spectra, namely, narrow spectral width and TE/TM splitting, are similar to the PL spectrum. However, in addition to one TE/TM doublet in the red spectral region in PL there is another one in the blue-green region (Fig. 3B, b). These are likely modes of the third order (the red ones being second order and undetected first order lay in infrared region), which cannot be observed in PL experiments since there is no blue PL in our Si-NCs. We proved also that a liquid drop on the surface of the waveguide (see Fig. 1) has no significant influence on the detected spectrum in this case.

The attenuation of guided modes in our samples is attributed to waveguide losses. Surface and sidewall roughness is usually supposed to cause waveguide losses. But in our sample the measured RMS roughness is only about 0.5 nm [6]. The loss is therefore likely due to self-absorption and/or Mie scattering in the waveguide core and diffraction of the guided modes at the output facet. The shifted-excitation-spot (SES) measurements revealed losses for guided modes to be about  $11 \text{ cm}^{-1}$  at 825 nm (implantation fluence of  $4 \times 10^{17} \text{ cm}^{-2}$ ) [10].

## 5. Conclusions

We have demonstrated the principal role of substrate radiation modes (leaky modes) in the spectral filtration effect in thin-film Si-NCs waveguides. The special features of the leaky modes are: (i) directionality better than for conventional waveguides, (ii) a high degree of polarization, and (iii) certain spectral tunability via varying the preparation conditions. Such features are interesting for photonic devices and may be compared with the emission of Si-NCs in an optical micro-cavity [11,12] (without the need to fabricate Bragg reflectors).

The consequences of this propagation mode for potential optical amplification (supposing the Si-NCs could give rise to stimulated emission) are being studied and will be published separately.

#### Acknowledgements

This work was supported through the projects No. IAA1010316 of GAAVCR, 202/03/0789 of GACR, the research centre LC510 of MSMT and the Australian Research Council. The research at the Institute of Physics is supported by the Institutional Research Plan AV0Z 10100521. Experimental assistance of K. Luterova and E. Skopalova is greatly appreciated.

#### References

- [1] S. Ossicini, L. Pavesi, F. Priolo (Eds.), *Light Emitting Silicon for Microelectronics*, Springer Tracts in Modern Physics, vol. 194, Springer, Berlin, 2003.
- [2] L. Dal Negro, M. Cazzanelli, N. Daldosso, Z. Gaburro, L. Pavesi, F. Priolo, D. Pacifici, G. Franzo, F. Iacona, *Physica, E* 16 (2003) 297.
- [3] L. Khriachtchev, M. Räsänen, S. Novikov, J. Lahtinen, *J. Appl. Phys.* 95 (2004) 7592.
- [4] J. Valenta, I. Pelant, K. Luterová, R. Tomasiunas, S. Cheylan, R.G. Elliman, J. Linnros, B. Hönerlage, *Appl. Phys. Lett.* 82 (2003) 955.
- [5] J. Valenta, T. Ostatnický, I. Pelant, R.G. Elliman, J. Linnros, B. Hönerlage, *J. Appl. Phys.* 96 (2004) 5222.
- [6] I. Pelant, T. Ostatnický, J. Valenta, K. Luterova, E. Skopalova, T. Mates, and R.G. Elliman, *Appl. Phys. B* (in press).
- [7] The software package SRIM developed by J.F. Ziegler et al., <http://www.srim.org>.
- [8] H.G. Unger, *Planar Optical Waveguides and Fibres*, Clarendon Press, Oxford, 1977.
- [9] T. Ostatnický, J. Valenta, I. Pelant, K. Luterová, R.G. Elliman, S. Cheylan, B. Hönerlage, *Opt. Mater.* 27 (2004) 781.
- [10] J. Valenta, I. Pelant, J. Linnros, *Appl. Phys. Lett.* 81 (2002) 1396.
- [11] S. Chan, P.M. Fauchet, *Appl. Phys. Lett.* 75 (1999) 274.
- [12] F. Iacona, G. Franzo, E.C. Moreira, F. Priolo, *J. Appl. Phys.* 89 (2001) 8354.

III

Silicon nanocrystals in silica -  
– Novel active waveguides for nanophotonics

P. Janda et al.  
Journal of Luminescence  
September 2006



## Silicon nanocrystals in silica—Novel active waveguides for nanophotonics

P. Janda<sup>a</sup>, J. Valenta<sup>a,\*</sup>, T. Ostatnický<sup>a</sup>, E. Skopalová<sup>b</sup>, I. Pelant<sup>b</sup>,  
R.G. Elliman<sup>c</sup>, R. Tomasiunas<sup>d</sup>

<sup>a</sup>Department of Chemical Physics & Optics, Faculty of Mathematics and Physics, Charles University, Prague, Czech Republic

<sup>b</sup>Institute of Physics, Academy of Sciences of the Czech Republic, Prague, Czech Republic

<sup>c</sup>Electronic Materials Engineering Department, Research School of Physical Sciences and Engineering, Australian National University, Canberra, Australia

<sup>d</sup>Institute of Materials Science and Applied Physics, Vilnius University, Vilnius, Lithuania

Available online 7 September 2006

### Abstract

Nanophotonic structures combining electronic confinement in nanocrystals with photon confinement in photonic structures are potential building blocks of future Si-based photonic devices. Here, we present a detailed optical investigation of active planar waveguides fabricated by Si<sup>+</sup>-ion implantation (400 keV, fluences from 3 to 6 × 10<sup>17</sup> cm<sup>-2</sup>) of fused silica and thermally oxidized Si wafers. Si nanocrystals formed after annealing emit red-IR photoluminescence (PL) (under UV-blue excitation) and define a layer of high refractive index that guides part of the PL emission. Light from external sources can also be coupled into the waveguides (directly to the polished edge facet or from the surface by applying a quartz prism coupler). In both cases the optical emission from the sample facet exhibits narrow polarization-resolved transverse electric and transverse magnetic modes instead of the usual broad spectra characteristic of Si nanocrystals. This effect is explained by a theoretical model which identifies the microcavity-like peaks as leaking modes propagating below the waveguide/substrate boundary. We present also permanent changes induced by intense femtosecond laser exposure, which can be applied to write structures like gratings into the Si-nanocrystalline waveguides. Finally, we discuss the potential for application of these unconventional and relatively simple all-silicon nanostructures in future photonic devices.

© 2006 Elsevier B.V. All rights reserved.

PACS: 78.67.Bf; 42.79.gn; 81.07.Bc

Keywords: Nanocrystals; Waveguide; Silicon; Photonics

### 1. Introduction

Research on silicon-based photonics is motivated by the aim to combine integrated electronic and photonic structures on a single silicon chip. Silicon quantum dots or nanocrystals (Si-NCs) have attracted much attention due to their strong photoluminescence (PL) [1] and have been used to demonstrate silicon-based light-emitting diodes [2,3]. Ensembles of Si-NCs can also be employed to fabricate active optical waveguides [4–8] that exhibit spectral filtering of the Si-NC PL emission, if the refractive

index profile is properly designed. The occurrence of narrow (~10 nm), polarization-dependent emission lines was reported by Khriachtchev et al. [4] for Si/SiO<sub>2</sub> waveguides and by our group [5,9] for samples containing Si-NC prepared by Si<sup>+</sup>-implantation into silica slabs. In our previous papers we explained the unexpected waveguiding properties using a model based on substrate leaking modes of a lossy waveguide [10,11].

In this work we compare the propagation of the intrinsic luminescence from Si-NCs with that of external light coupled into the waveguides. This knowledge is crucial for pump-and-probe measurements (e.g. optical gain) and potential application as photonic devices (modulators, amplifiers etc.). In addition we show permanent changes

\*Corresponding author. Tel.: +420 221911272; fax: +420 221911249.  
E-mail address: [jan.valenta@mff.cuni.cz](mailto:jan.valenta@mff.cuni.cz) (J. Valenta).

induced by femtosecond laser exposure which can be applied to write 2D structures (gratings etc.) into the Si-nanocrystalline waveguides with sub-micron resolution.

## 2. Experimental methods

Samples used in this study were prepared by Si<sup>+</sup>-ion implantation into 1 mm thick Infrasil (refractive index  $n_s = 1.455$ ) slabs with polished surfaces and edges, and into SiO<sub>2</sub> layers (about 5 μm thick) prepared by thermal oxidation of Si wafers. An implantation energy of 400 keV and ion fluences ranging between 3.0 and  $6.0 \times 10^{17} \text{ cm}^{-2}$  were used to fabricate the slab waveguides. In order to form Si nanocrystals the samples were annealed for 1 h at 1100 °C in an N<sub>2</sub> ambient and then passivated for 1 h at 500 °C in forming gas (5% H<sub>2</sub> in N<sub>2</sub>).

The implanted layer acts as an asymmetric planar waveguide. The profile of the refraction index depends not only on the implantation energy and fluence but also on the annealing conditions. Although the annealing temperatures, ambients and durations were nominally the same, various sets of samples were annealed in different laboratories and furnaces. Possible variations in the thermal history and levels of oxidation lead to apparent differences in refraction index for nominally identical samples (here, Figs. 2–4 present results from one set of samples and another set with lower refraction index is shown in Figs. 5–7). In order to numerically model the optical properties of particular samples the refraction index profiles were measured separately for each implanted sample. This was done by measuring infrared transmission spectra (see Fig. 2B) and fitting the interference fringes assuming an asymmetric double-Gaussian refraction index profile. The maximum of the profile is typically about 600 nm below surface with a half width of about 300 nm. The peak refraction index has a value as high as 2 for the highest implantation fluence [11]. The diameter of nanocrystals in the samples is estimated to be between 4 and 6 nm using Raman scattering (not shown here) [11].

PL was excited by a continuous wave He–Cd laser (325 nm, excitation intensity  $\sim 0.3 \text{ W/cm}^2$ ). The sample was placed on a rotatable  $x$ – $y$ – $z$  stage. A microscope with numerical aperture (NA) of 0.075 (i.e. an angular resolution of about 8.6°) was used to collect light and send it to a detection system consisting of an imaging spectrograph (Jobin Yvon Triax 190) with a CCD camera (Hamamatsu C4880) [9]. All measurements were performed at room temperature and all PL spectra were corrected for the system response.

The coupling of external light into the waveguides was achieved in two ways (Fig. 1):

- (a) Prism coupling of light from the upper surface of the sample. Light from the Xe or halogen lamp was collimated into a quartz prism. For better optical contact between the prism and sample an immerse liquid (index of refraction  $n = 1.515$ ) was dropped between the contact surfaces.

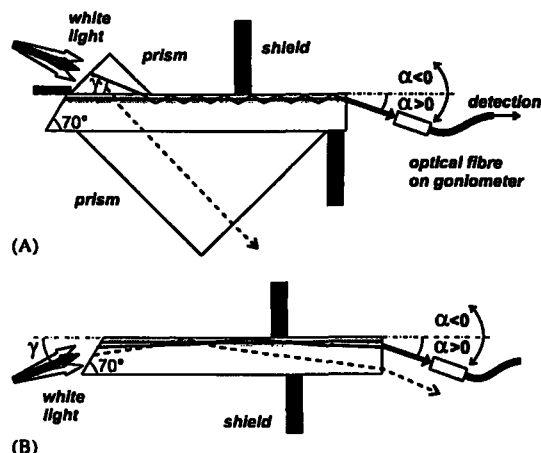


Fig. 1. Two experimental arrangements for coupling of external light into a waveguide sample: (A) coupling through a quartz prism on the upper sample surface. The second prism below sample is used to inhibit the back reflection of light not coupled into the waveguide; (B) focused light directed on the truncated edge of a sample. In both cases light leaving the opposite edge of sample is collected with an optical fiber and sent to a spectrometer. Sketches not to scale.

- (b) Direct coupling into the truncated facet (Fig. 1B). The edge of the sample was polished at angle of about 70° in order to separate light refracted to the higher-index waveguide from light entering lower-index substrate. Here a warm-white LED was used as a convenient light source. The angle of incidence  $\gamma$  was between 15° and 30° with respect to the plane of implanted layer. The divergence of incident light was about 10°.

In both external-light-coupling set-ups the signal is collected by an optical fiber (detection NA  $\sim 0.008$ ) and guided to the entrance slit of the imaging spectrometer Jobin Yvon Triax 320 (with the low-dispersion grating of 100 grooves/mm). Spectra are detected with the PI-Max intensified CCD (Princeton Instruments).

## 3. Results and discussion

### 3.1. Transmission spectra of Si-NC layers

The color of the Si-NC waveguide layers is yellow-brown with the optical density increasing with implantation fluence. The corresponding absorbance spectra are plotted in Fig. 2A (they are measured in a direction perpendicular to the nanocrystal plane using a UV-VIS double beam spectrometer (Hitachi U-3300), the non-implanted area of a silica slab being employed as a reference). The absorption edge has approximately exponential shape. In infrared spectral region several interference fringes are observed (Fig. 2B) which are used to model refraction index profile (see above).

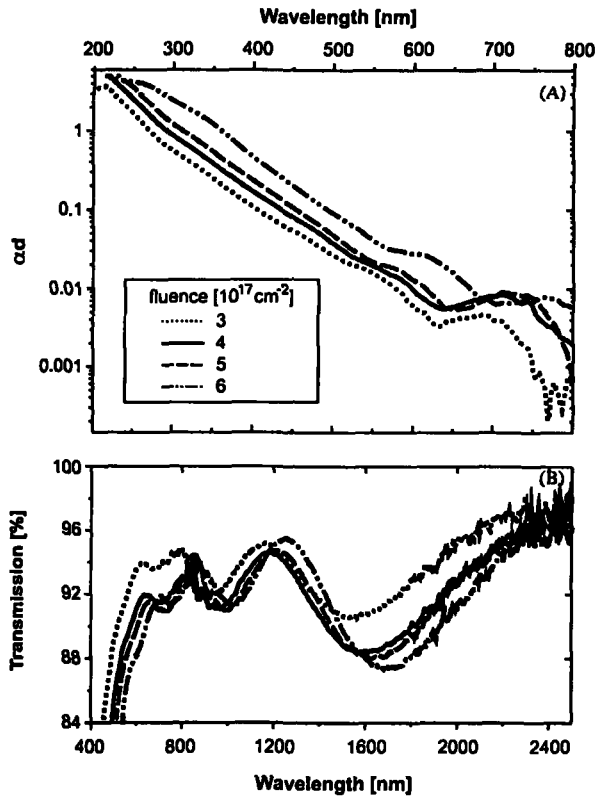


Fig. 2. (A) Absorption spectra of the samples implanted with fluences from 3 to  $6 \times 10^{17} \text{ cm}^{-2}$ . A non-implanted area of the fused silica slab was used as a reference. (B) Infrared transmission spectra of the same samples. Interference fringes are used to calculate refraction index profiles.

### 3.2. PL of active planar waveguides

The PL spectra of the active planar waveguides have very different shape depending on the experiment geometry. Two arrangements are used: (i) the light is collected in a direction roughly perpendicular to the sample plane (this is a conventional PL arrangement) or (ii) in the direction close to parallel to the waveguide plane (i.e. from the sample facet–waveguide arrangement)—see inset in Fig. 3. In the former geometry the PL spectra are always broad with a peak around 830 nm, typical of oxide-passivated Si NCs with mean diameter  $\sim 5 \text{ nm}$ . On the other hand, the waveguide geometry reveals narrow (down to 10 nm) spectral features with a high degree of linear polarization.

Figs. 3A and B show PL spectra of implanted oxide layers (on Si substrates) measured in directions perpendicular and parallel to the layer, respectively. The conventional PL (Fig. 3A) is modulated by deep interference fringes due to high reflectivity of the Si substrate. The facet-PL (Fig. 3B) is not affected by interference; instead a relatively narrow band is observed, the position of which depends on implantation fluence (i.e. refraction index profile). This peak shows partial linear polarization

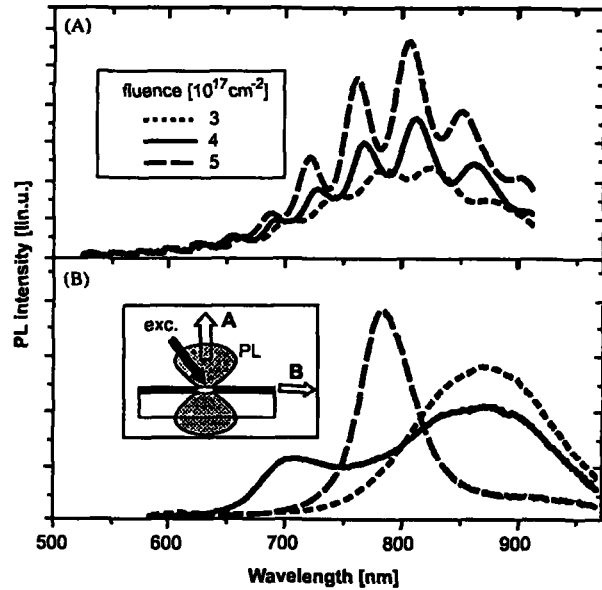


Fig. 3. PL spectra of  $\text{SiO}_2$  layers on Si substrates implanted with fluences of 3, 4, and  $5 \times 10^{17} \text{ cm}^{-2}$ . (A) PL detected in direction perpendicular to the layer. (B) PL detected in direction parallel to the layer (from the facet). The inset illustrates the experimental arrangement.

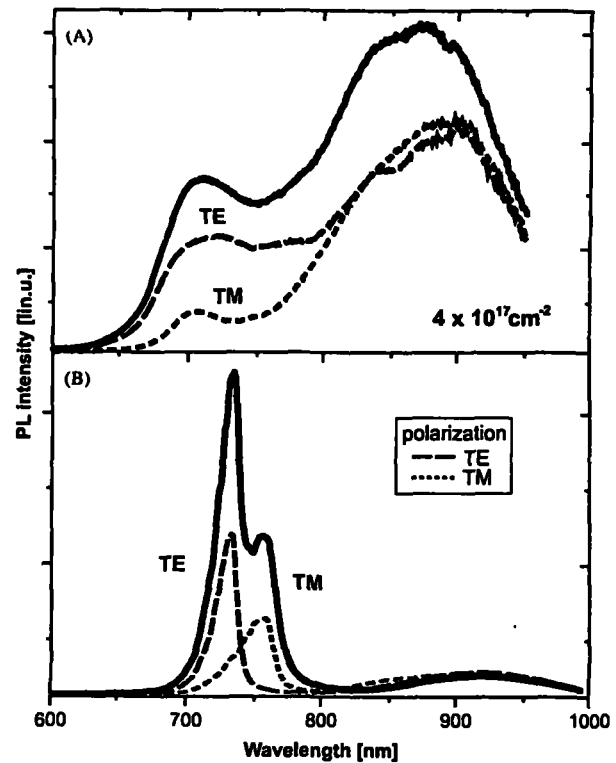


Fig. 4. PL spectra of  $4 \times 10^{17} \text{ cm}^{-2}$  layers measured in edge geometry without polarizer (solid line) or with a linear polarizer parallel (TE, dashed line) or perpendicular to the waveguide plane (TM, dotted line). The upper panel (A) concerns  $\text{SiO}_2$  layers on Si substrate, while the lower panel (B) is for implanted fused silica slab.

(Fig. 4A). Under identical conditions (of both fabrication and PL-experiment) the facet-PL features are much better resolved in implanted silica slabs (Fig. 4B). Here a clear splitting of the narrow PL peak into two peaks with polarization parallel (transverse electric TE or *s* mode) and perpendicular (transverse magnetic TM or *p* mode) to the Si-NC waveguide plane is observed. The following discussion is restricted to implanted fused silica slabs where the TE/TM splitted modes are nicely resolved.

PL spectra of other set of five samples prepared by implantation to fluences of 4.0, 4.5, 5.0, 5.5, and  $6.0 \times 10^{17} \text{ cm}^{-2}$  are plotted in Fig. 5. The upper spectra in Fig. 5A represent PL collected from the plane of implanted layers, while the lower PL spectra with TE/TM double-peaks are collected from the facet at angle  $+5^\circ$  ( $\text{NA}_{\text{det}} = 0.075$ ). An angle-resolved facet PL spectra from the layer implanted with dose of  $6 \times 10^{17} \text{ cm}^{-2}$  are plotted in Fig. 5B and the polar representation of their integrated intensity is shown in Fig. 5C. The TE/TM split doublets shift

to longer wavelength with increasing implantation dose. The facet PL has a very narrow emission cone with the maximum slightly shifted closer to substrate ( $\alpha \geq 0^\circ$ ) (Figs. 1B and C).

### 3.3. Theoretical model of the mode structure—radiative substrate modes

The surprising PL observations reported above do not correspond to simple waveguiding in ideal transparent waveguide which should transmit a continuous spectrum of guided modes up to a cut-off wavelength [12]. The cut-off for the first order modes of our waveguides can be estimated to lie above  $\sim 1500 \text{ nm}$ . Consequently, the waveguides should transmit the entire 600–900 nm band emitted by Si-NCs, which is clearly not the case. There are two possible explanations:

- (i) *Delocalized guided modes*: Let us assume wavelength-dependent losses in the waveguide, then those modes

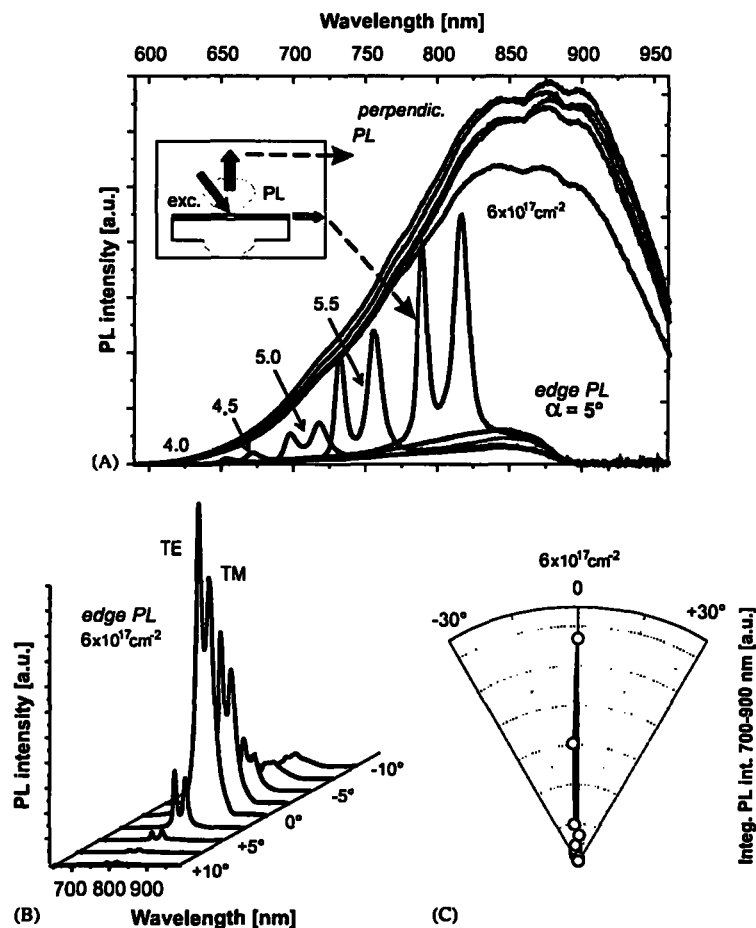


Fig. 5. PL spectra of five fused silica slabs implanted to fluences of  $4\text{--}6 \times 10^{17} \text{ cm}^{-2}$ . (A) Upper curves (a single wide band) correspond to PL emitted in a direction perpendicular to the waveguide, while lower spectra with doublet peaks are facet-PL detected in a direction  $\alpha = 5^\circ$  (a sketch of the experimental arrangement is shown in the inset). (B) Angle resolved facet PL spectra of the sample  $6 \times 10^{17} \text{ cm}^{-2}$ . (C) Polar representation of integrated PL intensity of angle resolved facet spectra from the panel B. Most of the PL intensity is emitted in a direction close to  $0^\circ$ .

(wavelengths) that undergo the smallest losses will be advantaged. These are likely those modes that are “weakly guided” with a strongly delocalized electric field. Such modes propagate basically as planar waves in the substrate [13]. Ray optics describes these modes by an angle of incidence  $\theta$  that is *greater than* but very close to the critical angle  $\theta_c$  for total internal reflection (here the lower core/SiO<sub>2</sub>-substrate boundary is of importance only since the refractive index contrast at the upper core/air boundary is high enough to ensure total internal reflection at angles  $\theta$  safely higher than  $\theta_c$ ). This model was proposed by Khriachtchev et al. [14,15] to explain TE/TM mode structure in Si-NC planar waveguides similar to ours. The spectral separation between TE and TM modes, is then a direct consequence of the asymmetric index profile with different phase shifts expected for the TE and TM modes under total reflection at both boundaries.

- (ii) *Radiative substrate modes*: We have previously proposed an alternative mechanism involving substrate leaking or radiation modes of the Si-NC waveguide [10,11]. These modes propagate at angle  $\theta$  situated close to but *below*  $\theta_c$  and undergo total reflection at the upper boundary (larger index difference) but are only partially reflected on the lower boundary (smaller index difference). Consequently, a small fraction of their power is radiated into the substrate at each bottom reflection. If the angle  $\theta$  is only slightly less than  $\theta_c$ , the leaking modes propagate near-parallel to the Si-NC plane. Moreover, the number of reflections is very high ( $R$  is close to unity), resulting in a narrow spectral width for the modes. The mechanism of spectral filtering in this case remains the same as discussed above, the only difference being that a phase shift at the upper boundary only comes to play during the initial stages of propagation. After a finite number of internal reflections all the radiant power escapes into leaking modes and emerges from the sample facet in a well defined direction, basically parallel to the Si-NC film. This makes such substrate modes virtually indistinguishable from the guided modes. The substrate modes are usually considered undesirable parasitic radiation and thus do not normally receive much attention. Indeed, only in cases where guided modes undergo significant losses (absorption and scattering in the waveguide core and diffraction on the narrow output aperture) do the substrate leaking modes play a dominant role.

The fact that the two above proposed mechanisms have a different dependence on the refractive index difference at the surface provides the basis for testing their validity experimentally. The principle is to change locally the cladding layer refractive index. This was done by placing liquid drops on the waveguide/air surface [11,16]. If a drop is above the excited PL spot, the TE/TM modes gradually red-shift and broaden with increasing refraction index of

applied liquid and eventually disappear if the index contrast approaches zero. However, when the drop is placed some millimeters away from the spot (between the photo-excited spot and the output facet), no changes in modes is observed, consistent with all the radiant power escaping into radiative substrate modes. These experiments are supported by numerical modeling of the PL spectra which show excellent agreement with experiments and provide unambiguous validation of the leaking modes model [11].

### 3.4. Coupling and propagation of external light in Si-NC waveguides

The transmission spectra of the five samples (implantation fluence  $4\text{--}6 \times 10^{17} \text{cm}^{-2}$ ) obtained by white-light coupling through a prism (Fig. 1A) are shown in Fig. 6. In the measured spectral region two broad transmission bands (blue and red) are observed for each sample. The positions of both bands red-shift with increasing fluence and the position of long-wavelength bands coincides with that of the PL leaking modes (Fig. 5A). Our calculation show that the red and blue bands correspond to second and third order leaking modes (the first one being in infrared). Broadening of the mode structure may be a consequence of the very low number of reflections undertaken by coupled light before escaping to the substrate [17].

Coupling of external light (the warm-white LED) through a truncated facet (Fig. 1B) gives the best result for a coupling angle  $\gamma \sim 20^\circ$ , as expected (Fig. 7). In this configuration we detect narrow and polarization-split peaks at an output angle  $\alpha \sim 2^\circ$ . The peaks are, however, not transmission but absorption peaks. This can be understood if it is assumed that the detected light is not from radiative substrate modes (which represent a small portion of transmitted light) but from filtered transmitted light propagating almost parallel to the Si-NC waveguide

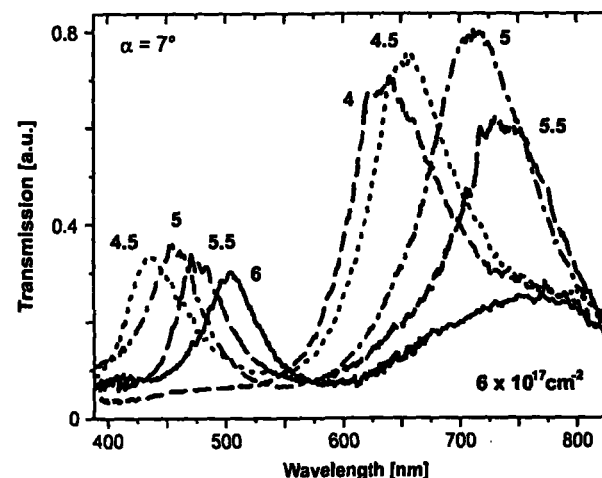


Fig. 6. The transmission spectra of prism-coupled light detected at angle  $\alpha = 7^\circ$  from samples presented in Fig. 5.



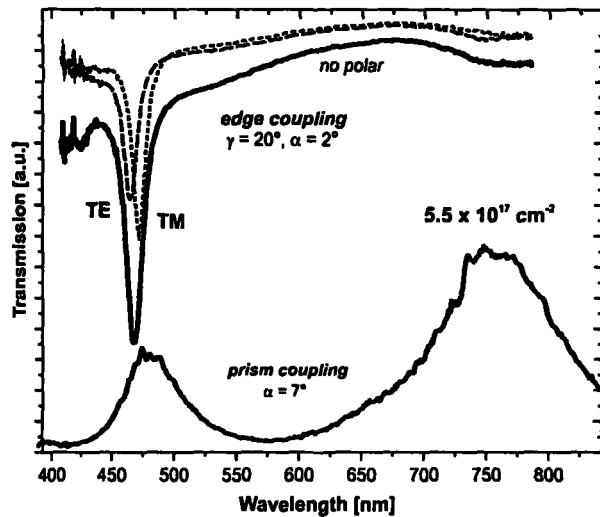


Fig. 7. Comparison of transmission spectra of sample  $5.5 \times 10^{17} \text{ cm}^{-2}$  obtained by the direct facet-coupling (upper curves, solid line—no-polarization, dashed and dotted lines correspond to TE and TM polarization, respectively) and by the prism-coupling (lower spectrum).

from which a part of power escaped to the substrate modes. The blue third order modes are much stronger compared to second order because of higher absorption in blue spectral region.

### 3.5. Leaking modes vs. optical gain

One of the most interesting questions concerning nanocrystal waveguides is the interplay between radiative substrate modes and optical amplification by stimulated emission. Since the first report on optical gain in Si-ion implanted Si-NC layers by Pavesi et al. [18] similar samples have been investigated by other groups with both positive [4] and negative [19] results. Two aspects of this problem are addressed here.

First, experimental artefacts have been shown to play an important role when measuring optical gain close to leaking modes maxima by the commonly used variable-stripe-length (VSL) technique [20]. These artefacts are mainly due to unconventional propagation and coupling of these modes in the detection system, and their interplay with the NA of detection. In order to correct most of these artefacts it has previously been proposed that VSL measurements be combined with a shifting-excitation-spot (SES) technique [20]. Indeed, it should be stressed that the interpretation of VSL results without associated SES measurements can lead to erroneous results.

Secondly, the potential advantages of leaking modes for achieving optical gain are spectral narrowing, low losses, and directionality of propagation. On the other hand the propagation path of radiative modes through a pumped active medium (Si-NCs forming the waveguide) is limited by leakage into the substrate. Attempts to achieve optical

gain on leaking modes was successful only under strong nanosecond pulsed pumping (6 ns, 355 nm from THG-Nd:YAG laser) with the gain threshold around  $50 \text{ mJ/cm}^2$  and maximum gain at TM mode of about  $12 \text{ cm}^{-1}$  for  $100 \text{ mJ/cm}^2$  excitation [21].

Further theoretical investigation of the radiative modes in the loss/gain medium is in progress.

### 3.6. Permanent changes of Si-NC waveguides induced by laser pulses

The Si-NC waveguides in silica may be damaged by high-intensity laser excitation and apparent differences in damage are evident for nanosecond and femtosecond pulses. When irradiated with the 420-nm, 5 ns output of an optical parametric oscillator (OPO) pumped by THG-Nd:YAG (NL 303 + PG122, Ekspla) the damage threshold is very sharp at around  $800 \text{ mJ/cm}^2$ . The damage appears as micrometer-size granular aggregates in the Si-NC followed immediately by complete ablation of the implanted layer. The mechanism is most probably related to heating and even melting of Si-NCs [22] which leads to failure of the silica matrix. This is evidenced by the appearance of cracks and surface ruptures which can lead to complete removal of the SiNC layer.

In contrast, femtosecond laser excitation (400 fs, 400 nm from SHG-Ti:sapphire laser) starts to modify sample at much lower pulse energies  $\geq 20 \text{ mJ/cm}^2$ . There are two distinct phases of layer damage. The initial stage appears as darkening (brown coloration) of the excited area. Micro-Raman measurements (not presented here) show that it corresponds to amorphization of the Si-NC layer

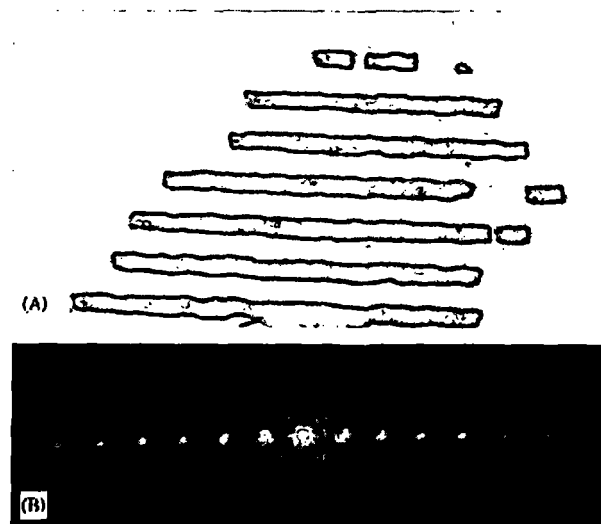


Fig. 8. (A) The diffraction grating (period of about  $12 \mu\text{m}$ ) ablated in the Si-NC waveguide (implanted fluence  $4 \times 10^{17} \text{ cm}^{-2}$ ) by an interfering laser pulses from femtosecond laser (SHG-Ti:sapphire laser, 400 fs, 400 nm). (B) A photograph of the pattern produced by diffraction of 633 nm He-Ne laser beam on the ablated grating.

(it appears similar to the implanted layer before annealing). In the second step at higher excitation the layer is ablated. Clearly, the damage mechanism for ultrashort laser pulses (400 fs) is different to that of the longer (5 ns) pulses. The advantage of fs-ablation is that the boundary between the ablated and unchanged area can be very sharp, enabling fs-laser-ablation to be used for lithography to create microstructures in the planar waveguides. In Fig. 8 we demonstrate a diffraction grating with 12  $\mu\text{m}$  period written into  $4 \times 10^{17} \text{cm}^{-2}$  implanted layer by 400 fs, 400 nm fs-pulses.

#### 4. Conclusions

Si-ion implantation into silica slabs or oxide layers on Si wafer followed by annealing is a relatively easy way to fabricate active nanocrystalline planar waveguides. In spite of their simplicity these waveguides show rich optical phenomena which are mainly connected to peculiar radiative substrate modes—so-called leaking modes. This study has investigated the influence of these complex propagation modes on PL, transmission, and gain spectra both experimentally and theoretically. Similar anomalous phenomena connected to the interplay between radiative and guided modes are expected to take place in other types of active waveguides. The possibility of spectral, polarization, and spatial filtering reported for active Si-NC waveguides offer interesting possibilities for application in silicon-based photonic devices or sensors.

#### Acknowledgement

Financial support through the projects of Research plan MSM0021620835 and Research centre LC510 of MSMT CR, Project no. IAA1010316 of GAAV CR, 202/01/D030 of GACR, the Australian Research Council, and a grant of the Lithuanian State Foundation for Science and Studies (R.T.) is greatly acknowledged. The research work at the Institute of Physics is supported by Institutional Research Plan no. AV0Z 10100521. One of the authors (I.P.) thanks the Laserlab-Europe Integrated Initiative for financial support (vulrc001168).

#### References

- [1] S. Ossicini, L. Pavesi, F. Priolo (Eds.), *Light Emitting Silicon for Microelectronics*, vol. 194, Springer, Berlin, 2003 Springer Tracts in Modern Physics.
- [2] A. Irrera, D. Pacifici, M. Miritello, G. Franzo, F. Priolo, F. Iacona, D. Sanfilippo, G. Di Stefano, P.G. Fallica, *Appl. Phys. Lett.* 81 (2002) 1866.
- [3] R.J. Walters, G.I. Bourianoff, H.A. Atwater, *Nature Mater.* 4 (2005) 143.
- [4] L. Khriachtchev, M. Räsänen, S. Novikov, J. Sinkkonen, *Appl. Phys. Lett.* 79 (2001) 1249.
- [5] J. Valenta, I. Pelant, K. Luterová, R. Tomasiunas, S. Cheylan, R.G. Elliman, J. Linnros, B. Hönerlage, *Appl. Phys. Lett.* 82 (2003) 955.
- [6] L. Dal Negro, M. Cazzanelli, N. Daldosso, Z. Gaburro, L. Pavesi, F. Priolo, D. Pacifici, G. Franzo, F. Iacona, *Physica E* 16 (2003) 297.
- [7] M. Cazzanelli, D. Navarro-Urrios, F. Riboli, N. Daldosso, L. Pavesi, J. Heitmann, L.X. Yi, R. Scholz, M. Zacharias, U. Gösele, *J. Appl. Phys.* 96 (2004) 3164.
- [8] L. Khriachtchev, M. Räsänen, S. Novikov, J. Lahtinen, *J. Appl. Phys.* 95 (2004) 7592.
- [9] J. Valenta, T. Ostatnický, I. Pelant, R.G. Elliman, J. Linnros, B. Hönerlage, *J. Appl. Phys.* 96 (2004) 5222.
- [10] T. Ostatnický, J. Valenta, I. Pelant, K. Luterová, R.G. Elliman, S. Cheylan, B. Hönerlage, *Opt. Mater.* 27 (2005) 781.
- [11] I. Pelant, T. Ostatnický, J. Valenta, K. Luterová, E. Skopalova, T. Mates, R.G. Elliman, *Appl. Phys. B* 83 (2006) 87.
- [12] H.G. Unger, *Planar Optical Waveguides and Fibres*, Clarendon Press, Oxford, 1977.
- [13] H. Kogelnik, V. Ramaswamy, *Appl. Opt.* 13 (1974) 1867.
- [14] L. Khriachtchev, M. Räsänen, S. Novikov, *Appl. Phys. Lett.* 83 (2003) 3018.
- [15] L. Khriachtchev, S. Novikov, J. Lahtinen, M. Räsänen, *J. Phys. Condens. Matter* 16 (2004) 3219.
- [16] K. Luterová, E. Skopalová, I. Pelant, M. Rejman, T. Ostatnický, J. Valenta, *J. Appl. Phys.*, accepted for publication.
- [17] P. Janda, J. Valenta, T. Ostatnický, I. Pelant, R.G. Elliman, *Thin Sol. Films* (in press).
- [18] L. Pavesi, L. Dal Negro, C. Mazzoleni, G. Franzo, F. Priolo, *Nature* 408 (2000) 440.
- [19] R.G. Elliman, M.J. Lederer, N. Smith, B. Luther-Davies, *Nucl. Instrum. Meth. Phys. Res. B* 206 (2003) 427.
- [20] J. Valenta, I. Pelant, J. Linnros, *Appl. Phys. Lett.* 81 (2002) 1396.
- [21] K. Luterová, D. Navarro, M. Cazzanelli, T. Ostatnický, J. Valenta, S. Cheylan, I. Pelant, L. Pavesi, *Phys. Status Solidi (c)* 2 (2005) 3429.
- [22] B.V. Kamenev, H. Grebel, L. Tsybeskov, *Appl. Phys. Lett.* 88 (2006) 143117.

IV

Optical gain in planar waveguides

T. Ostatnický et al.

XV Czech-Polish-Slovak optical conference

September 2006

# Optical gain in planar waveguides

T. Ostatnický<sup>a</sup>, P. Janda<sup>a</sup>, J. Valenta<sup>a</sup>, I. Pelant<sup>b</sup>

<sup>a</sup>Faculty of Mathematics and Physics, Charles University in Prague, Czech Republic

<sup>b</sup>Institute of Physics, Academy of Sciences of the Czech Republic, Czech Republic

## ABSTRACT

Description of optical waveguides is commonly restricted to propagation at distances much larger than the width of the waveguide core and therefore only guided modes are taken into account in theory. Effects connected with leaking of the waves into the substrate may be, however, very important for possible applications in microelectronics. In this paper, we overview our model of photoluminescence of an active planar waveguide and we extend it in order to describe mode formation during propagation in the waveguide. We also include optical amplification into our model and derive formula for description of the Variable Stripe Length (VSL) method widely used for measurement of the net gain coefficient. We demonstrate necessity for corrections of VSL results since their straightforward interpretation may be misleading.

**Keywords:** planar waveguide, optical gain, silicon nanocrystals, radiative modes

## 1. INTRODUCTION

High-density integration of current integrated circuits has physical limits due to heat dissipation and other effects. Some of these problems may be solved by incorporation of new types of devices, for example optoelectronic or spintronic.

Electronic chips are mostly fabricated on silicon substrates using planar technologies that enable to create Si/SiO<sub>2</sub> islands, metallic interconnections, *p* and *n*-doped areas etc., but cannot directly integrate devices based on other types of semiconductor materials (GaAs optoelectronic devices etc.). Unlike bulk silicon, which emits light inefficiently, nanostructured silicon could be used to build integrated light sources, which are under recent research.

Luminescence was achieved using porous silicon or silicon nanocrystals<sup>1</sup> and also electroluminescence was demonstrated.<sup>2,3</sup> A source of coherent light based on silicon is, nevertheless, under development because of a small optical gain of Si nanocrystals<sup>4,5</sup> (of the order  $\sim 10 \text{ cm}^{-1}$ ).

Light sources integrated in optoelectronic devices will be probably in a form of active planar or rib waveguides – waveguiding structures with embedded Si nanocrystals or other luminescent bodies. As shown previously,<sup>6,7</sup> these waveguides reveal unavoidable mode leaking of radiation from the waveguide core to the substrate. The radiated field then propagates along the waveguide core and it is detected in spectroscopic experiments together with the guided modes. Although we can take the advantage of this effect for e.g. luminescence spectral filtering in active nanophotonic devices<sup>8</sup> leaking of energy to the substrate is also potentially unwanted effect in integrated devices because it may be responsible for cross talks or other errors.

In this work, we present results of our theoretical investigation of the effects connected with guiding and leaking of light in planar structures on a transparent substrate. The paper may be divided to two main parts: stationary properties (sections 3 and 4) and mode propagation (sections 5 to 7). In the first part, we outline our model which explains our experimental observations in photoluminescence (PL) experiments under low excitation and we show how the parameters of samples may influence measured PL spectra. In the second part, we extend the model in order to describe mode propagation in the direction of the waveguide and we focus on mode formation with and without presence of optical gain. At the end, we show important consequences which follow from our theory for optical spectroscopy but also for future applications in optoelectronics.

---

<sup>\*</sup> Corresponding author e-mail: [ostv@matfyz.cz](mailto:ostv@matfyz.cz); Address: Ke Karlovu 3, 12116 Prague 2, Czech Republic

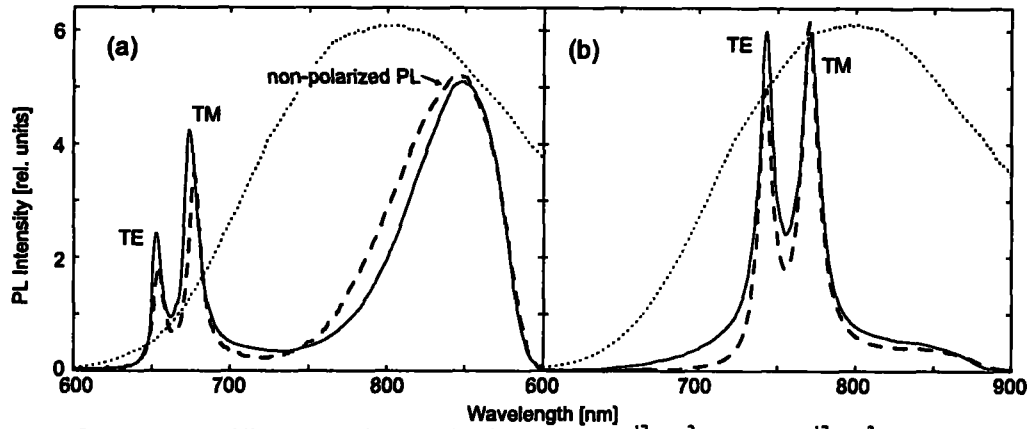


Fig. 1: PL from the waveguiding samples implanted to fluences of  $4 \cdot 10^{17} \text{ cm}^{-2}$  (a) and  $5 \cdot 10^{17} \text{ cm}^{-2}$  (b). The dotted line depicts PL collected in the normal geometry and the solid line the PL measured in the waveguiding geometry. The dashed line is the result of numerical modeling. The TE and TM-polarized peaks are well resolved.

## 2. EXPERIMENTAL

Our samples are formed by a thin layer ( $\sim 1 \mu\text{m}$  thick) of silicon nanocrystals (Si-NCs) with average diameter of about 5 nm (determined by Raman scattering) in 1 mm thick silica slabs. The Si-NC layer was prepared by  $\text{Si}^+$ -ion implantation to a polished substrate at the energy of 400 keV. The samples were subsequently annealed in order to form Si-NCs in the implanted layer. As a result, active layers of luminescent Si nanocrystals with density controlled by the fluence of  $\text{Si}^+$  ions were formed on transparent substrates. The distribution of the Si-NCs density (and thus the refractive index) below the sample surface was non-uniform with a peak at the depth  $\sim 0.6 \mu\text{m}^9$  (Fig. 4b).

We measured photoluminescence (cw excitation by a He-Cd laser at 325 or 442 nm) of the waveguiding layer in two geometries (cf. Fig. 2): in a standard normal incidence geometry (both excitation and detection nearly perpendicular to the implanted layer) and in the waveguiding geometry (excitation perpendicular to the layer, detected light was collected from the sample edge in the direction parallel with the waveguide).<sup>7</sup> The signal was collected by a microscope objective lens with collection angle about  $9^\circ$ . At the normal incidence, the PL spectra reveal the usual shape (see Fig. 1) of Si nanocrystals – the PL spectrum covers a broad spectral region with the peak around 800 nm and obviously its shape is not affected by the spatial confinement in the waveguiding layer. In the waveguiding geometry, on the contrary, the PL spectrum contains narrow peaks besides a broad spectrum as seen in Fig. 1, the doublet contains the TE and TM polarized modes as verified experimentally. Similar spectral filtering feature of the waveguiding samples was reported also by other groups.<sup>10</sup>

The samples reveal also unique features when the core/substrate is irradiated at angles near  $\pi/2$ : spectra of absorbance reveal TE and TM-polarized peaks, see Fig. 3. Unlike the PL peaks, resonances are observable in a broader spectral region which is not limited by the spectrum of radiation of the Si-NCs and therefore we observe more TE/TM doublets in absorbance. Spectral positions of the PL maxima coincide with the peaks in the absorbance spectra.

Optical gain is usually measured by the Variable Stripe Length (VSL) method. The principle of the method is, that a spatially wide laser beam is focused by a cylindrical lens to excite a stripe in the sample. Depending on the stripe length  $\ell$ , the intensity of the amplified spontaneous emission (ASE) signal detected in the waveguiding geometry is expected to increase with extending length  $\ell$  due to amplification of the spontaneous emission<sup>11</sup> (the gain coefficient is denoted  $g$ ):

$$I(\ell) \propto \frac{\exp[g\ell] - 1}{g} \quad (1)$$

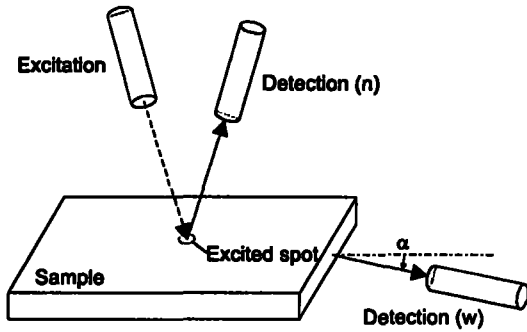


Fig. 2: Sketch of the experimental setup with the normal (n) and the waveguiding (w) geometry.

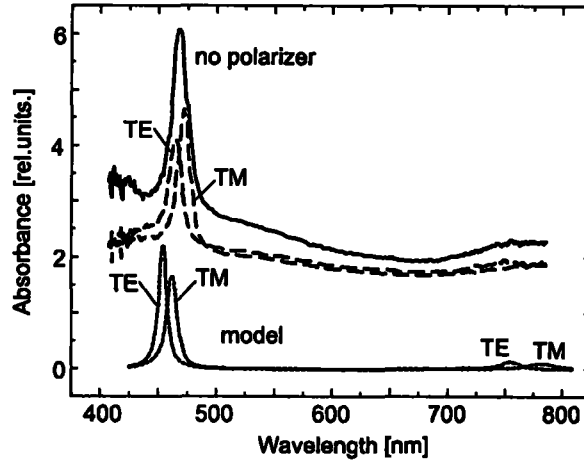


Fig 3: Absorbance of the waveguiding sample implanted to a fluence of  $5.5 \cdot 10^{17} \text{ cm}^{-2}$  in the reflection geometry when the implanted layer was illuminated by white light at an angle near  $90^\circ$ . The solid line is the overall measured signal, dashed lines depict measured TE and TM-polarized spectra and the dotted line is a numerical calculation.

The formula (1) is, however, valid only in the limit of high net gain since it doesn't take into account leaking of waves out of the excited stripe. This fact was pointed out and it was verified experimentally that interpretation of the results of the VSL experiments may be misleading if the results were not corrected for the leaking. For this reason, we proposed a simple experimental method – called Shifting Excitation Spot (SES)<sup>5</sup> – which is suitable for such corrections. Using the VSL and SES methods, it was shown,<sup>5,12</sup> that the measured net gain in the waveguiding samples strongly depends on the spectral position. We explain this fact by a model which follows.

### 3. MODEL

In this section, we consider a sample with a step-like profile of the refractive index (see Fig. 4a) for clarity. (Numerical calculations in the next section are performed with a real profile of the refractive index.) The waveguide with refractive index  $n$  and thickness  $d$  is deposited on a substrate with refractive index  $n_s$  and it is covered by a cladding with refractive index  $n_c$ . We consider that the substrate is transparent and the guiding layer absorbs light (the refractive indexes  $n_c$  and  $n(\lambda) = n(\lambda) + i\lambda\gamma(\lambda)/4\pi$  are generally complex). Nanocrystals randomly distributed in the guiding layer are the source of PL.

Our explanation of occurrence of the narrow peaks in PL spectra (under cw excitation) is based on the existence of the substrate radiative modes besides the guided modes of a waveguide.<sup>13</sup> The guided modes propagate mostly inside the waveguide core and leave a sample through its edge, see Fig. 4a. The radiative modes, on the contrary, leave the waveguide core after several reflections at the core/substrate boundary and then they freely propagate in the lossless substrate until they reach the edge. The crucial point is, that both types of the modes may propagate in the same directions and therefore we cannot separate them when using a detection system with a small numerical aperture.<sup>14</sup>

The total spectral density of the detected radiation may be expressed as  $I(\lambda) = I_G(\lambda) + I_R(\lambda)$ , where  $I_G(\lambda)$  stands for the part of the guided modes and  $I_R(\lambda)$  is the part of the radiative modes. The spectrum of the guided modes is broad without any narrow maxima since there exists a guided mode for every wavelength far below the cutoff (the cutoff is expected to be above  $2 \mu\text{m}$  in our samples). Although Khriachtchev *et al.* proposed<sup>10</sup> that the narrow peaks in the PL spectra are formed by the selective absorption due to the mode delocalization, our calculations and experiments have shown<sup>7</sup> that this model is insufficient. We therefore express the spectral profile of the guided modes by an approximate formula:

$$I_G(\lambda, z) = I_0(\lambda) \exp[-\gamma(\lambda)z], \quad (2)$$

where  $I_0(\lambda)$  stands for the spectral density of the PL of the nanocrystals (i.e. experimentally measured spectrum in the normal geometry) and a variable  $z$  is the distance of an excited spot from the sample edge. We consider that the spectrum of the guided modes does not depend on the observation angle  $\alpha$  due to diffraction on the sample edge.<sup>14</sup> On the contrary, there exists an unambiguous relation between the angle of detection of the radiative modes  $\alpha$  and their direction of propagation in the waveguide core  $\vartheta$  (see Fig. 4a). Considering this fact, one may derive<sup>6</sup> the formula for spectral density of the radiative modes:

$$I_R(\lambda, \alpha) = \frac{I_0(\lambda)T(\vartheta)}{|1 - r_1(\vartheta)r_2(\vartheta)\exp[2i\kappa(\lambda, \vartheta)d]|^2} \frac{d\vartheta}{d\alpha} \quad (3)$$

Functions  $r_1$  and  $r_2$  are the reflection coefficients for reflection on the two respective core boundaries,  $T$  is the transmittance of the core/substrate boundary,  $\kappa = \sqrt{\left(\frac{2\pi}{\lambda}n\right)^2 - \beta^2} = \frac{2\pi}{\lambda}n \cos \vartheta$  is the wave vector of the mode in the direction perpendicular to the propagation direction and the term  $\frac{d\vartheta}{d\alpha}$  is the correction factor for the spatial density of the PL radiated by a nanocrystal which is isotropic in the core. Assuming an aperture of the detection system with a nonzero size, the detected signal may be calculated using the equation:

$$I_{\text{TOTAL}}(\lambda) = \int_{\alpha_0}^{\alpha_1} [I_G(\lambda) + I_R(\lambda, \alpha)] d\alpha, \quad (4)$$

where  $\alpha_{0,1}$  denote the limits of the integration over the aperture of the detection system. Formula (3) clearly shows that the shape of PL spectrum of the radiative modes strongly depends on the angle of detection  $\alpha$  and therefore we may do the following conclusion.

The PL spectrum contains two components: narrow peaks and a broad spectrum shifted to longer wavelengths compared to the original PL of the intrinsic nanocrystals due to wavelength-dependent absorption. The ratio of the magnitudes of these two parts depends on the absorption coefficient of the core layer and the geometry of the detection system. We may generally state that the higher absorption induces stronger appearance of the radiative modes. This fact directly follows from Eqs. (2) and (3): since  $z \gg d$ , the guided modes are suppressed when losses in the core are too high, while radiative modes propagate mostly in the transparent substrate. This fact was clearly illustrated in our previous publications<sup>7</sup> where the absorption coefficient increases with the fluence of implantation. At the lowest fluence, a wide PL band is resolved above 700 nm and no radiative modes are seen while the spectra for higher fluences contain both types of PL. The above statements are further supported experimentally<sup>12</sup> – we were able to separate the PL of the guided modes by spatial filtering.

#### 4. NUMERICAL CALCULATIONS

We considered an asymmetric continuous profile of the refractive index below the sample surface. The particular profiles of the refractive indexes were determined on the basis of numerical fitting of infra-red transmission spectra<sup>9</sup> and are schematically plotted in Fig. 4b. We slightly modified the above formulae and we numerically calculated the PL spectra using the standard transfer matrix formalism. The results are plotted in Fig. 1 for the parameters used in the experiments.

The shape of the PL spectrum depends on the conditions of observation (position of a detector and its numerical aperture) and it also strongly depends on the sample parameters and thus the preparation conditions. These facts are summarized in Fig. 5 where we plotted the calculated dependences of PL characteristics (widths of the respective TE and TM peaks and their spectral positions) on the following parameters: the angle of observation  $\alpha$ , peak value of the core refractive index  $\Delta n$  (controlled by the fluence of implantation), width of the distribution of nanocrystals  $\sigma$  below the sample surface and the refractive index of the cladding  $n_a$ . We took parameters of the sample implanted with fluence of  $5 \cdot 10^{17} \text{ cm}^{-2}$  as a reference.

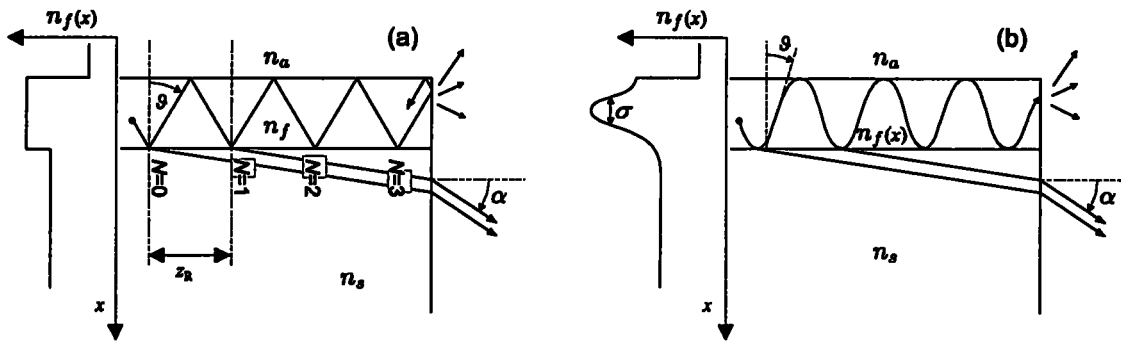


Fig. 4: Ray propagation in a sample with step-like (a) and continuous (b) profile of refractive index of the core.

In our particular case, the planar waveguide is considered to be asymmetric, i.e.  $n_a < n_s$ . Radiative modes are therefore expected to leak only to the substrate and to be observed only for angles  $\alpha > 0$  as seen in Fig. 5a. Change of the observation angle causes change of both the exponential factor in Eq. (3) and reflectivity on the core/substrate boundary and therefore the spectral positions and widths of the PL maxima change. The greater detection angle  $\alpha$  is, the smaller is the reflectivity of the core/substrate boundary and the wider PL peaks are.

Figs. 5b-d illustrate the possibility of tuning the sample properties by variation of the preparation conditions. We may prepare for example structures for real-time sensing of the refractive index of liquids which is represented by the refractive index of the cladding in Fig. 5d, Ref. 7.

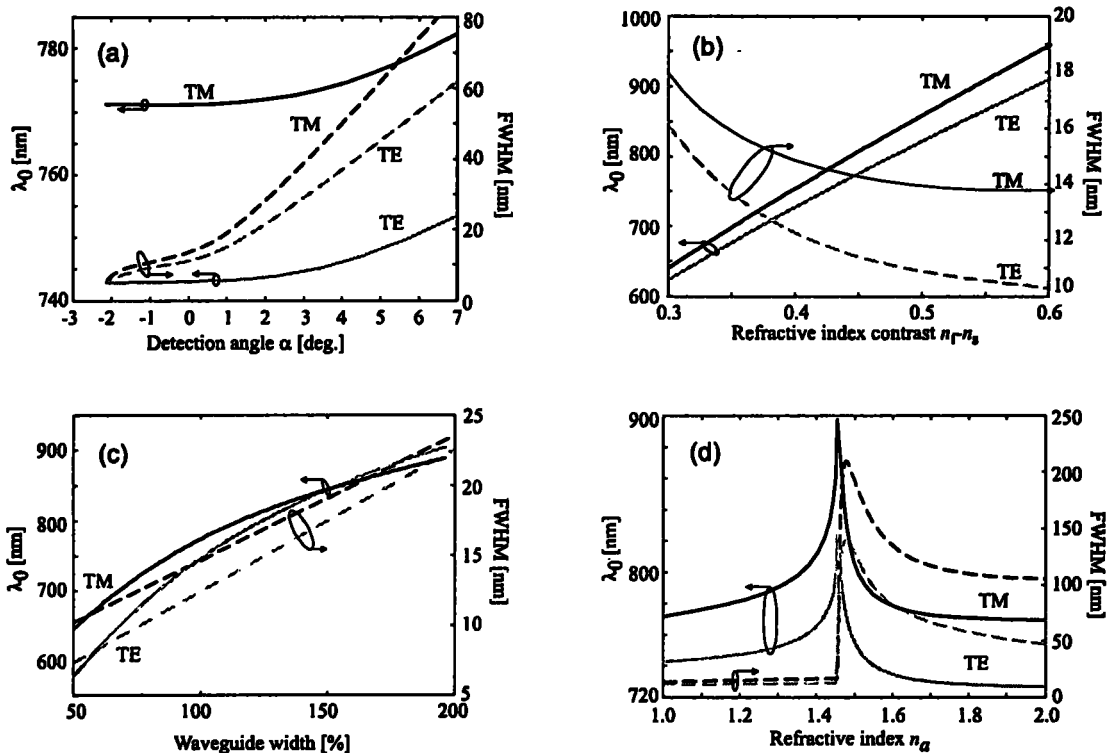


Fig 5: Calculated dependence of the spectral width and spectral position of the modes detected in PL on: (a) detection angle in the waveguiding geometry, (b) contrast of the maximum of the refractive index of the core relative to the refractive index of the substrate, (c) width of distribution of the refractive index of the core (100% means FWHM of the refractive index distribution  $6.5 \mu\text{m}$ ) and (d) refractive index of the cladding. We took the parameters of the sample implanted with fluence of  $5 \cdot 10^{17} \text{ cm}^{-2}$  as a reference.



The grazing incidence absorbance spectra depicted in Fig. 3 are also fully consistent with the model. Although light should be totally reflected by the waveguiding structure, some part is absorbed in the core. The maximum of absorption arises when the phase matching condition is met – this is the same condition as the condition for the peak of PL. Calculated theoretical curve of the absorbance is depicted in Fig. 3 by a dotted line.

## 5. FORMATION OF MODES

The model formulated in section 3 describes a situation when the waves undergo an infinite number of reflections inside the waveguide core. This situation corresponds to an experiment in which the excitation spot is far from the edge ( $z \gg d$ ). However, as pointed out in our previous publication<sup>15</sup> and later by Khriachtchev *et al.*,<sup>10</sup> the shape of the modes in PL undergoes evolution when the distance of the excitation spot from the edge is increased. Interpretation, based on our model, is simple: the smaller is the distance  $z$ , the less round-trips between the core boundaries are performed by the wave. Constructive/destructive interference is best met at an infinite number of reflections and therefore we expect the best mode formation at high number of reflections  $N$  and therefore at long distances  $z$  whereas no modes in the PL spectra are expected at small distances. The effect may be enhanced due to the dominance of radiative modes at long distances and the dominance of the flat spectrum of the guided modes at small distances.

Spectrum of the guided modes is not influenced by the number of internal reflections and therefore we can keep formula (2) for determination of their spectral profile. Formula (3), however, needs a correction for a finite number of reflections:

$$I_R(\lambda, \alpha, z) = \left| \frac{1 - [P(\lambda, \alpha)]^{N(\vartheta, z) + 1}}{1 - P(\lambda, \alpha)} \right|^2 I_0(\lambda) T(\vartheta) \frac{d\vartheta}{d\alpha}, \quad (5)$$

$$P(\lambda, \alpha) = r_1(\vartheta) r_2(\vartheta) \exp[2i\kappa(\lambda, \vartheta)d] \exp[-\gamma(\lambda, \vartheta)z_R / 2], \quad (6)$$

where  $N(\vartheta, z)$  is the number of reflections of the wave inside the core and  $z_R$  is the distance between two points of reflection on the core/substrate boundary. The intensity of radiation which remains in the core after  $N$  reflections of a ray on the core/substrate boundary (see Fig. 4a) may be expressed as:

$$I(N) = I_0 |r_1 r_2|^{2N} = I_0 \exp[-2\gamma_{\text{eff}} z], \quad (7)$$

and therefore the number of reflections may be evaluated in the following way:

$$N = - \frac{\gamma_{\text{eff}} z}{\log|r_1 r_2|}, \quad (8)$$

and  $z_R = - \frac{\log|r_1 r_2|}{\gamma_{\text{eff}}}$ , where  $\gamma_{\text{eff}}$  is an effective attenuation coefficient which reflects the leaking to the substrate. It may be calculated from the Poynting vector. In the case of an asymmetric waveguide with the step-like profile of the refractive index, the coefficient may be expressed for TE waves as:<sup>13</sup>

$$\gamma_{\text{eff}} = \frac{\kappa^2}{\beta d} \frac{\rho}{(\kappa + \rho)^2}, \quad (9)$$

$$\rho^2 = \left( \frac{2m_s}{\lambda} \right)^2 - \beta^2. \quad (10)$$

In structures with more complicated profile of the refractive index, the attenuation coefficient must be evaluated numerically, however Eqs. (7) and (8) remain valid. Results of the calculation of the narrowing of the modes in a sample with step-like profile of the refractive index are plotted in Fig. 6. Presence of the guided modes may cause apparent shift of the PL maxima due to wavelength-dependent absorption. Calculated widths of the maxima and the distance on which they are formed strongly depend on the profile of refractive index: if it changes continuously, modes would be wider and they would form on longer distances  $z$ .

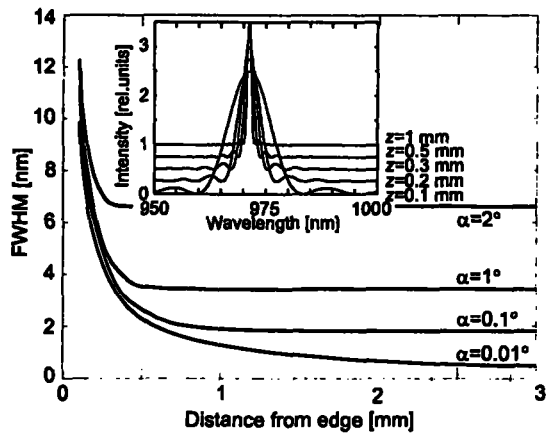


Fig. 6: Width of the radiative modes as a function of the distance of the excitation spot from the sample edge. Default parameters are  $n_s=1.46$ ,  $n_r=1.8$ ,  $\gamma=10 \text{ cm}^{-1}$ ,  $d=1.5 \mu\text{m}$ . Inset shows spectral profile of the modes.

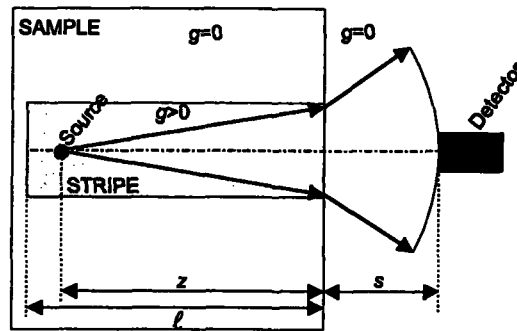


Fig. 7: Sketch for derivation of the ASE signal.

## 6. OPTICAL GAIN

Considering a homogeneously excited stripe with length  $\ell$  which reveals an optical gain and considering that only the plane waves which propagate in the direction of the excited stripe are detected, one derives formula (1) for dependence of the detected light intensity on  $\ell$ . The formula is widely used in spectroscopy in the VSL method, however it is valid (for real detectors with a nonzero numerical aperture) only in the limit of large optical gain. For the limit of small or zero optical gain and a large numerical aperture of the detector, a rigorous theoretical and experimental review was published,<sup>16</sup> however we use a simplified approach in order to show the main characteristics of the waveguiding samples. First we derive a formula for determination of the ASE signal as a function of the stripe length in a bulk sample. We must take into account that the amount of energy radiated by a nanocrystal and detected by a detector scales with the distance  $r$  between the nanocrystal and the detector as  $1/r^2$ . Let's denote the distance between the edge of the sample and the detector  $s$  considering that  $s$  is much larger than the width of the excited stripe, let's denote the gain coefficient  $g$  and the real part of the refractive index of the sample  $n_r$  (see Fig. 7). One may directly derive that the total intensity detected by the detector is:

$$I_G(\ell) \propto \int_0^{\ell} \frac{\exp[(g-\gamma)z]}{(z+n_r s)^2} dz. \quad (11)$$

Note that the above formula describes the situation depicted in Fig. 7 – if the signal is collected using some optical elements in front of the detector, the calculation must be adapted according to the particular situation. The function in Eq. (11) is not integrable analytically, however for large  $g$  it clearly reduces to Eq. (1). We plotted the function (11) for various parameters in graph in Fig. 8. Obviously it qualitatively fits the measured ASE curves.<sup>12</sup> The exponential growth of the experimental data slightly above the zero length of the excited stripe is due to diffraction or other optical artifacts which are not taken into account in the present model.

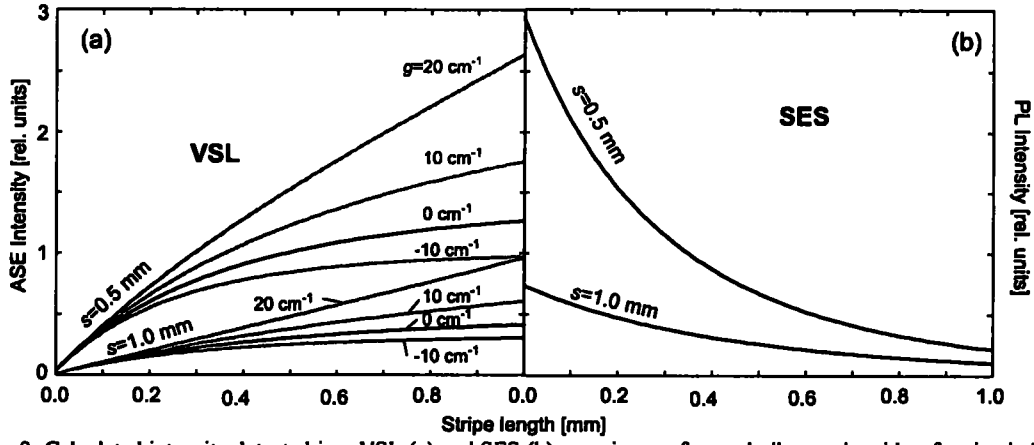


Fig. 8: Calculated intensity detected in a VSL (a) and SES (b) experiments from a bulk sample with refractive index 1.6 and with the detector in the distance 0.5 and 1 mm from the sample edge. Curves of ASE are calculated for zero, positive and negative gain coefficients considering the loss coefficient  $\gamma=10\text{ cm}^{-1}$ .

The ASE curves reveal interesting behavior on for larger lengths of the excitation stripe as shown in Fig. 9 where we plot dependence of ASE on the stripe length for the same parameters as in Fig. 8, however on a different scale for  $\ell$ . ASE curves in Fig. 8, when compared with Eq. (1), seem to reveal no net gain or a small net gain and strong saturation. Our calculations show that the apparent saturation is due to the beam divergence and the behavior of superlinear ASE growth arise for larger lengths of the stripe of the order of several mm. In Fig. 9a we show the ASE curves for gain coefficients  $g=0\text{ cm}^{-1}$  and  $g=20\text{ cm}^{-1}$  in linear scale with graphs of Eq. (1) for  $g=20\text{ cm}^{-1}$  and  $g=4.7\text{ cm}^{-1}$  (best fit). Fig. 9b shows the same curves on an even large scale for  $\ell$  in order to show that fitting by (1) may give incorrect results if performed for small stripe lengths – the net gain may be underestimated.

Discussion of optical amplification in waveguides is more complicated because of the existence of the waves which leak into the substrate. Guided modes propagate in the waveguiding layer and thus they are amplified on the whole path. The formula analogous to Eq. (9) for the guided modes thus differs only in the denominator which is in the first power:

$$I_{RC}(\ell) \propto \int_0^{\ell} \frac{\exp[(g-\gamma)z]}{z+n_r s} dz. \quad (12)$$

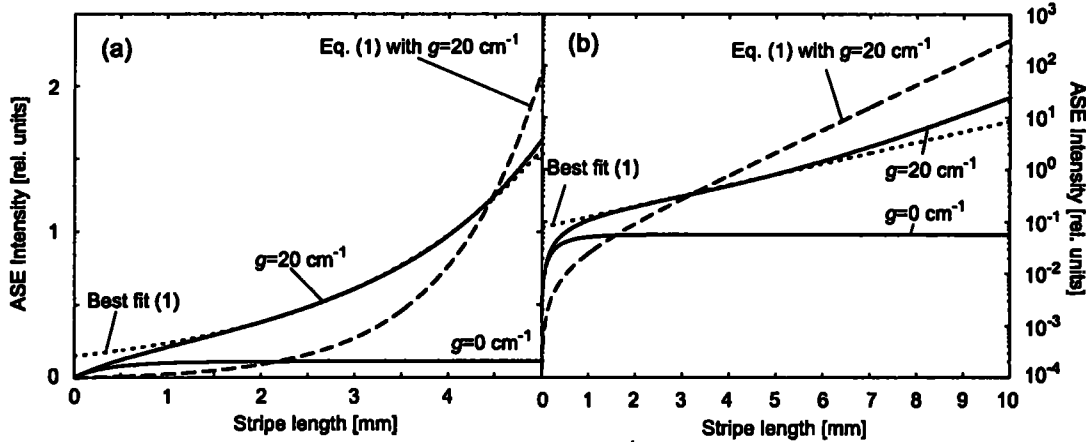


Fig. 9: Same as Fig. 8 on longer scales for  $\ell$  for  $g=0$  and  $20\text{ cm}^{-1}$ , respectively. The solid curves stand for predictions of our model based on Eq. (12), the dashed curve is the result of Eq. (1) with  $g=20\text{ cm}^{-1}$  and the dotted line is the best fit of Eq. (12) by Eq. (1) with  $g=4.6\text{ cm}^{-1}$ .

The radiative modes, on the contrary, may be amplified only on a part of their path because of their leakage to the substrate. Some of the radiative modes are effectively amplified if the gain coefficient is high enough to compensate the losses by leaking. We divide derivation of the intensity of the detected waves into two parts: (i) a contribution from the wave which remains in the core until it reaches a sample edge and (ii) from the wave refracted to the substrate. For the waves in the core, the same formula as Eq. (12) holds when  $\gamma$  is substituted by  $\gamma_{\text{eff}}$  according to Eq. (9) ( $\gamma_{\text{eff}} = \gamma$  for the guided modes). Considering the refracted waves, we must take into account that they are amplified only during propagation in the core and that once the wave leaves the core, its intensity decreases with the second power of the distance:

$$I_{\text{RS}}(z) = \frac{I_0}{(z + n_r s)^2} \left| \frac{1 - P^{N+1}}{1 - P} \right|^2 T \frac{d\theta}{d\alpha}, \quad (13)$$

$$P = r_1 r_2 \exp[2i\kappa d] \exp\left[\frac{g z_M}{2m}\right] \exp[(g - \gamma)z_R / 2]. \quad (14)$$

The total ASE signal in the VSL experiment is expressed as the sum:

$$I(\ell) = \int_0^\ell I_{\text{RS}}(z) dz + C_C I_0 \int_0^\ell \frac{\exp[(g - \gamma_{\text{eff}})z]}{z + n_r s} dz. \quad (15)$$

Here the symbol  $C_C$  expresses an efficiency of coupling of the guided modes to the detector – generally it is less than 1 due to nonzero numerical aperture of the waveguide. The above function is plotted for various parameters in Fig. 10a-d. The panels a-b in Fig. 10 show for comparison predicted ASE and SES curves for parameters similar to Fig. 8 (bulk sample). The initial rise of the ASE measured at wavelengths of the radiative modes is not an effect of optical gain but a specific (linear optical) characteristics of the waveguiding samples as proven by our calculations. The influence of mode leaking is clearly seen in Figs. 9c-d: the leaking is most efficient for large detection angles  $\alpha$  and near the mode maximum at 971.5 nm while the modes are mostly guided far from the resonance or at low detection angles. Leaking causes very complex dependence of the mode coupling to the detector on the distance of the excitation spot from a sample edge. This effect was also observed experimentally.<sup>5</sup> Due to the limited path in the core, leaking waves are amplified with low efficiency compared to the guided modes, as seen in Fig. 10a. Their net gain may be, nevertheless, positive but always lower than the net gain of the guided modes.

## 7. DISCUSSION

Spectrally narrow modes which leak into the substrate are formed, as demonstrated in the results in the previous two sections, on distances much larger than the waveguide width. This phenomenon was observed experimentally by our group<sup>15</sup> and by Khriachtchev *et al.*<sup>10</sup> Our results do not fit the experimental data exactly because we did not take into account the exact profile of the refractive index of the sample and we did not consider that the excitation spot has a nonzero size. The qualitative agreement between the experiment and calculations is, however, excellent and we may conclude that our model describes the PL experiments with high precision.

In our calculations of SES and ASE curves, we considered a specific experimental setup depicted in Fig. 7 which models an experiment in which the PL signal is collected by an optical fiber without any optics between the sample and the fiber. Additional optical elements, however, make the calculations more complex. Optics usually display the sample edge on an input of a detector (e.g. an optical fiber, an entrance slit of a spectrometer) and its influence is therefore that only the numerical aperture is changed and the effective distance between the sample and the detector is  $s \rightarrow 0$ . The values  $s \approx 1$  mm used above are not therefore underestimated and the results of calculations may be qualitatively compared with experimental data.

The curves in Fig. 8 qualitatively reproduce the measured data<sup>12</sup> except for the initial rise for  $\ell \rightarrow 0$  which is due to diffraction, as noted above. Although the ASE signal in the VSL experiments increase sublinearly, simulations show that it is not due to the saturation of optical gain but it is caused by the decrease of the coupling efficiency between the source and the detector. The effect of varying coupling may be eliminated by putting the detector far from the sample.

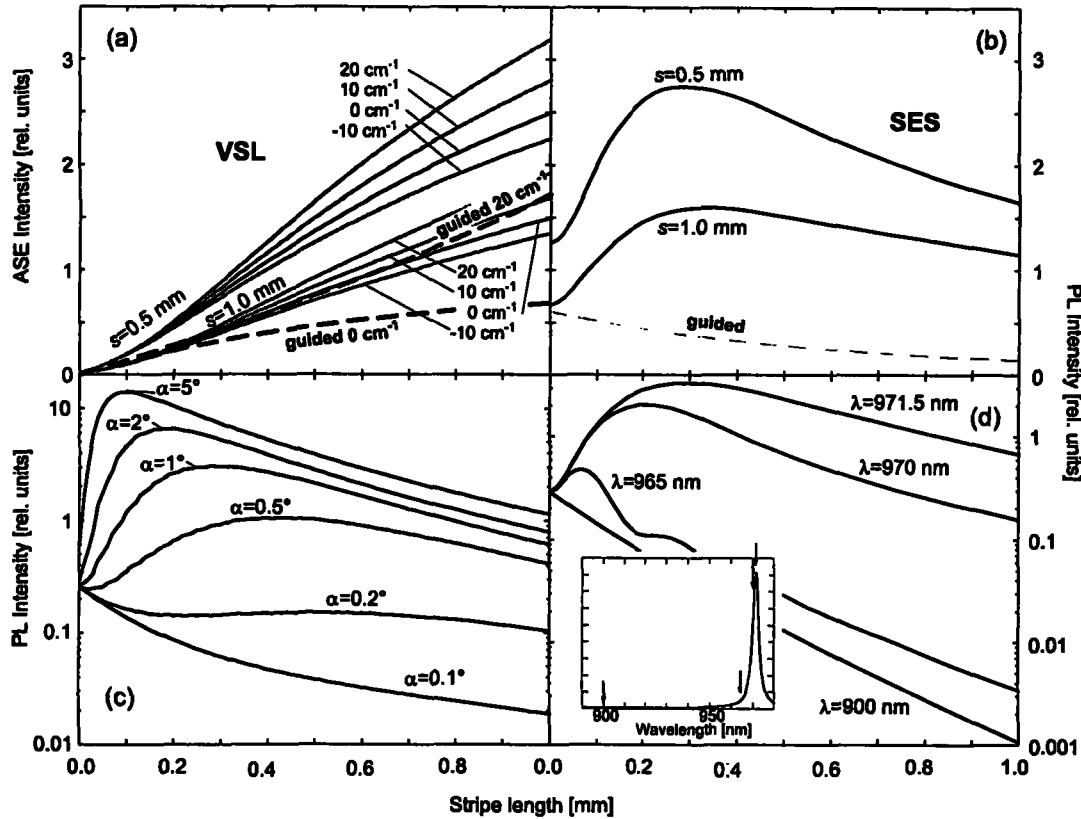


Fig. 10: Calculated ASE (a) and SES (b-d) curves from a waveguiding sample according to Eq. (15) for leaking waves (solid) and guided modes (dashed). Parameters of the sample were: refractive index  $n_s=1.46$ ,  $n_f=1.8$ ,  $\gamma=10 \text{ cm}^{-1}$ ,  $d=1.5 \mu\text{m}$ . Default detection angle was considered  $\alpha=1^\circ$ , distance of the detector from the sample edge  $s=0.5 \text{ mm}$ , detection wavelength  $971.5 \text{ nm}$  (in the maximum of a mode). Figs. (c) and (d) show how the shape of the SES curves change with detection angle and wavelength.

This setup corresponds to the Fraunhofer limit of diffraction, i.e. we detect only a plane wave with well defined direction and the formula (11) reduces to Eq. (1).

Simulations on the waveguiding samples in Fig. 10 are in a good agreement with our experimental data.<sup>5</sup> Guided modes reveal the usual behavior: they are amplified on the whole path through the sample until they reach the edge. The effective losses are only due to the divergence, i.e. due to the varying coupling to the detector. When compared to the bulk samples, the coupling coefficient decrease only with the first power of the distance between the excited spot and the detector and therefore the superlinear growth of the ASE signal may be more likely observed than in the bulk samples.

Leaking waves, on the other hand, reveal themselves very unusually. In the SES experimental setup, the PL intensity grows with the distance  $z$  and after reaching some limit, it starts to decrease. The limiting distance  $z$  is determined by the angle of the mode propagation in the waveguide core and therefore by the angle of observation. The SES experiments may be interpreted as follows. The wave is radiated in the core and it subsequently propagates in the core and partly leaks to the substrate. The longer is the distance of propagation, the more energy is transferred to the substrate. We detect the sum of the wave which remains in the core and the wave refracted to the substrate from the edge, however the refracted wave is usually stronger because of absorption in the core and diffraction at the edge. With increasing distance  $z$ , the intensity of PL is increasing until the growth is overridden by the decay due to decreasing coupling to the detector.

Presence of the positive optical gain is responsible for the growth of ASE in the VSL configuration and therefore the optical amplification may be detected by the direct comparison of the integrated SES and VSL measurements.

Determination of the gain coefficient is, however, difficult and the changes in PL are not pronounced as nicely as if the measurement is performed on the guided modes.

The gain measurement should give better results if measured on the guided modes only. We show in Fig. 10d that the guided modes may be experimentally separated by spectral filtering – if the detected signal is selected from the broad PL spectrum outside the TE and TM-polarized peaks, only guided modes are coupled to the detector. Analysis of the net optical gain is then based on Eq. (12) or on a more complex theory in Ref. 16.

## 8. CONCLUSIONS

We develop a model which describes formation and optical amplification of the modes in optical waveguides (both leaking and guided). The behavior of the guided modes is affected only by the effective reduction of the dimensionality of the sample to 2D (compared to bulk samples) and therefore the effective losses due to divergence of the radiated field are lower than in bulk samples. This fact may result in observation of superlinear increase of the ASE signal on waveguides containing Si nanocrystals, however we stress out that one must still compare ASE and SES curves in order to identify whether the net gain is positive or negative. A special attention must be, nevertheless, paid to the leaking waves since they cause a variety of unwanted effects.

Leaking waves may cause problems not only in spectroscopic experiments but they may play an important role in micro-optoelectronics on integrated devices. The source of signal (guided modes) then may be also the source of the noise guided by the substrate. It may therefore appear desirable to cut off the noise by addition of an absorbing layer to the substrate or in another way, if necessary.

## 9. ACKNOWLEDGEMENTS

The authors thank to Prof. R.G. Elliman from Australian National University Canberra for ion-implantation of waveguiding samples. This work was supported by the Grant Agency of the Academy of Sciences of the Czech Republic (grant IAA 1010316), by the Ministry of Education of the Czech Republic in the framework of the research centre LC510 and the research plans MSM 0021620834 and AV0Z 10100521.

## REFERENCES

1. L.T. Canham, "Silicon quantum wire array fabrication by electrochemical and chemical dissolution of wafers", *Appl. Phys. Lett.* **57**, 1046-1048, 1990.
2. L. Tsybeskov, S.P. Duttagupta, K.D. Hirschman, and P.M. Fauchet, "Stable and efficient electroluminescence from a porous silicon-based bipolar device", *Appl. Phys. Lett.* **68**, 2058-2060, 1996.
3. K. Luterová, I. Pelant, J. Valenta, J.-L. Rehspringer, D. Muller, J.J. Grob, J. Dian, and B. Hönerlage, "Red electroluminescence in Si<sup>+</sup>-implanted sol-gel-derived SiO<sub>2</sub> films", *Appl. Phys. Lett.* **77**, 2952-2954, 2000.
4. L. Khriachtchev, M. Räsänen, S. Novikov, and J. Sinkkonen, "Optical gain in Si/SiO<sub>2</sub> lattice: Experimental evidence with nanosecond pulses", *Appl. Phys. Lett.* **79**, 1249-1251, 2001.
5. J. Valenta, I. Pelant, and J. Linnros, "Waveguiding effects in the measurement of optical gain in a layer of Si nanocrystals", *Appl. Phys. Lett.* **81**, 1396-1398, 2002.
6. J. Valenta, T. Ostatnický, I. Pelant, R.G. Elliman, J. Linnros, and B. Hönerlage, "Microcavity-like leaky mode emission from a planar optical waveguide made of luminescent silicon nanocrystals", *J. Appl. Phys.* **96**, 5222-5225, 2004.
7. I. Pelant, T. Ostatnický, J. Valenta, K. Luterová, E. Skopalová, T. Mates, and R.G. Elliman, "Waveguide cores containing silicon nanocrystals as active spectral filters for silicon-based photonics", *Appl. Phys. B* **83**, 87-91, 2006.
8. P. Janda *et al.*, *J. Lumin.*, in print, 2006.
9. R.G. Elliman, M.J. Lederer, and B. Luther-Davis, "Optical absorption measurements of silica containing Si nanocrystals produced by ion implantation and thermal annealing", *Appl. Phys. Lett.* **80**, 1325-1327, 2002.
10. L. Khriachtchev, M. Räsänen, and S. Novikov, "Efficient wavelength-selective optical waveguiding in a silica layer containing Si nanocrystals", *Appl. Phys. Lett.* **83**, 3018-3020, 2003.
11. K.L. Shaklee, R.F. Leheny, and R.E. Nahory, "Stimulated Emission from the Excitonic Molecules in CuCl", *Phys. Rev. Lett.* **26**, 888-891, 1971.

12. K. Luterová, M. Cazzanelli, J.-P. Likforman, D. Navarro, J. Valenta, T. Ostatnický, K. Dohnalová, S. Cheylan, P. Gilliot, B. Hönerlage, L. Pavesi, and I. Pelant, "Optical gain in nanocrystalline silicon: comparison of planar waveguide geometry with a non-waveguiding ensemble of nanocrystals", *Opt. Mater.* **27**, 750-755, 2005.
13. M. Dietrich: *Theory of dielectric optical waveguides*, Academic Press, Boston, 1991.
14. T. Ostatnický, J. Valenta, I. Pelant, K. Luterová, R.G. Elliman, S. Cheylan, and B. Hönerlage, "Photoluminescence from an active planar waveguide made of silicon nanocrystals: dominance of leaky substrate modes in dissipative structures", *Opt. Mater.* **27**, 781-786, 2005.
15. J. Valenta, I. Pelant, K. Luterová, R. Tomasiunas, S. Cheylan, R.G. Elliman, J. Linnros, and B. Hönerlage, "Active planar optical waveguide made from luminescent silicon nanocrystals", *Appl. Phys. Lett.* **82**, 955-958, 2003.
16. L. Dal-Negro, P. Bettotti, M. Cazzanelli, D. Pacifici, and L. Pavesi, "Applicability conditions and experimental analysis of the variable stripe length method for gain measurements", *Opt. Commun.* **229**, 337-348, 2004.

V

Modified spontaneous emission of silicon nanocrystals  
embedded in artificial opals

P. Janda et al.

article sent in February 2007 to Applied Physics B



# Modified spontaneous emission of silicon nanocrystals embedded in artificial opals

**Petr Janda, Jan Valenta\***

*Department of Chemical Physics & Optics, Faculty of Mathematics and Physics,  
Charles University, Ke Karlovu 3, 121 16 Prague 2, Czechia*

**Jean-Luc Rehspringer, Rodrigue R. Mafouana**

*Institut de Physique et Chimie des Matériaux de Strasbourg, GMI et GONLO,  
UMR46 CNRS-ULP-ECPM, 23, rue du Loess, F-67037 Strasbourg, France*

**Jan Linnros**

*Department of Microelectronics & Information Technology  
Royal Institute of Technology, Electrum 229, 164 21 Kista-Stockholm, Sweden*

**Robert G. Elliman**

*Electronic Materials Engineering Department, Research School of Physical Sciences and  
Engineering, Australian National University, Canberra, ACT 0200, Australia*

**PACS:** 78.67.Bf, 42.79.gn, 81.07.Bc

## ABSTRACT

Si nanocrystals were embedded in synthetic silica opals by means of Si-ion implantation or opal impregnation with porous Si suspensions. In both types of sample photoluminescence (PL) is strongly Bragg-reflection attenuated (up to 75%) at the frequency of the opal stop-band in a direction perpendicular to the (111) face of the perfect hcp opal structure. Time-resolved PL shows a rich distribution of decay rates, which contains both shorter and longer decay components compared to the ordinary stretched exponential decay of Si nanocrystals. This effect reflects changes in the spontaneous emission rate of Si NC due to variations in the local density of states of real opal containing defects.

## 1. Introduction

Silicon nanostructures are promising materials for realizing all-silicon optoelectronics. Light emission from bulk silicon, is very inefficient due to its indirect band-gap structure and the dominance of non-radiative recombination. In contrast, nanocrystalline silicon shows strong photoluminescence (PL) with quantum efficiency of the order of several percent [1]. However, the performance of Si-based light-emitting devices is limited by a relatively low emission rate and a broad emission spectrum. One possible way to manipulate the emission rate, wavelength, and direction is the inclusion of Si nanocrystals (NC) within photonic structures. For example, silicon nanocrystals can form active planar waveguides that exhibit surprising photoluminescence narrowing, polarization, and directionality [2]. They may also be coupled to a spherical micro-cavity and show whispering gallery modes in PL spectra [3].

The suppression of spontaneous emission by photonic band-gap structures was proposed in the seminal paper by E. Jablonovitch in 1987 [4] and is probably most clearly demonstrated for PL from a GaInAsP quantum well in a 2D photonic-crystal slab (five times

---

\* corresponding author: e-mail: [jan.valenta@mff.cuni.cz](mailto:jan.valenta@mff.cuni.cz), tel. +420 221911272

reduction of PL emission rate in the near-infrared spectral region) [5]. Throughout the past decade artificial opal has been used to demonstrate the influence of photonic structure on the luminescence of dye molecules or nanocrystals in the visible spectral range [6]. Artificial opals are prepared from sub-micrometer beads of silica, polystyrene, etc. that are organized into a stochastic mixture of hcp and fcc structures [7]. However, such material exhibits only optical stop-bands (not a complete photonic band-gap) due to the fact that the refractive index contrast between the beads and voids is low. This problem can be overcome by using inverted opals that are formed by filling the opal pores with higher index material (silicon [8], TiO<sub>2</sub> [9] etc.) and removing of initial (template) beads. This can be used to increase the refractive index contrast and thereby produce larger modification of the density of photonic states. Several attempts to fill the opal voids with semiconductor nanocrystals have been undertaken and their modified emission reported [10,11,12,13,14].

In this article we report on the fabrication of Si NCs in silica artificial opals by means of Si<sup>-</sup> ion implantation or opal impregnation with porous Si colloidal suspensions. PL spectra of Si NCs at the stop-band frequency are shown to be largely attenuated by Bragg reflection. PL decay rates show new slow and fast components due to variations in the local density of photonic states in the opal. Micro-PL imaging also highlights interesting aspects associated with light localization by defects.

## 2. Sample preparation and experimental set-up

Silica microspheres were prepared following the modified Stöber-Finck process that has been shown to result in particle size dispersion better than about 2 %. Large synthetic opals were prepared using electro-sedimentation from colloidal solution of silica spheres. The sedimentation lasts for approximately 4 days under static electric fields of 0.2 V/cm applied between a platinum grid and a mercury layer. Self-supporting bulk opals were obtained by partial sintering of the silica particles at 950°C for 2 hours (Fig. 1). The mean diameter of the silica balls used in this study was about 300 nm (Fig. 2a). Electron microscope and AFM images reveal an fcc structure of opal with (111) plane on the surface. Fig. 2b shows a Fourier-transform of the image in Fig. 2a which highlights the hexagonal structure of the opal and shows a layer periodicity of 288 nm and a mean bead size of 333 nm.

Si nanocrystals were introduced into the opal in two ways:

(i) Si<sup>-</sup> ion implantation (energy of 100 keV and dose of  $0.5 \times 10^{17} \text{ cm}^{-2}$ ) followed by annealing at 1100 °C for 1 hour in nitrogen. This procedure formed Si nanocrystals inside the SiO<sub>2</sub> balls. A TRIM (Transport of Ions in Matter) calculation [15] of the implantation profile for 100 keV Si<sup>-</sup> ions into quartz reveals a mean projected range of 150 nm. A simple numerical calculation gives an estimation of the excess Si concentration in the case of an opal structure (neglecting the curvature of the silica balls) showing that 66 %, 29 %, and 5 % of the ions are stopped in the first, second and third layer of silica spheres, respectively (implanting the (111) plane of a perfect opal fcc crystal). (ii) Luminescing Si nanocrystals were formed by conventional electrochemical etching of Si wafers (<100> p-type,  $\rho \sim 0.1 \text{ Ohm cm}$ ) in a HF-ethanol (1:2.5) solution. The etching current density was kept relatively low (1.6 mA/cm<sup>2</sup>) in order to obtain higher porosity and, consequently, resulting in a low mean size of Si-nc (the PL band peak is around 680 nm). Porous-Si (P-Si) powder (i.e. grains of interconnected oxidized Si NCs) was then obtained by mechanical pulverization (scratching with a blade) of the P-Si film from the silicon substrate. A colloidal suspension was prepared by pouring ethanol onto the P-Si powder and mixing it in an ultrasonic bath. The suspension was then sedimented for several days and the supernatant component extracted and dispensed onto the opal surface. The opal surface was subsequently flushed with high pressure filtered air to remove any residual P-Si particles.

PL and reflection spectra were measured using micro-spectroscopy set-ups based on imaging spectrographs (Horiba Jobin Yvon Triax 190 or 320) connected to conventional far-field microscopes. A liquid nitrogen (LN)-cooled CCD camera (Hamamatsu C4880) or amplified thermoelectrically (TE)-cooled camera (Princeton Instruments PI-max) was used for detection of images and spectra. The set-up enables controlled measurement of reflection or PL spectra from any spot on the sample with resolution down to the diffraction limit (i.e. roughly 500 nm for visible wavelengths). The UV-line of a cw He-Cd laser (325 nm) was employed to excite the PL (in grazing incidence to the observed sample plane, excitation intensity up to 0.5 W/cm<sup>2</sup>) and a halogen lamp (focused and collected by the microscope objective lens) was used for reflection measurement. Time-resolved PL was excited with an optical parametric oscillator (tuned to 420 nm, pulse duration around 5 ns, and excitation density on the sample of about 70 kW/cm<sup>2</sup>) pumped with a pulsed Nd:YAG laser (Ekspla NL303 and PG122) and detected with the PI-max camera (Princeton Instruments). Reflection micro-photographs were taken with a digital camera Olympus Camedia C5060wz and a micro-adapter C3040-ADUS.

### 3. Experimental results and discussion

#### 3.1. Reflection spectra

Reflection micro-imaging and spectroscopy of opals reveal large variations of reflection intensity due to existence of domains with various crystalline quality (Figs. 1 and 3a). Regions with high reflection in directions perpendicular to the surface have a perfect stop-band around 690 nm (compare Fig. 3b and Fig. 4). The relative band width  $\Delta\lambda/\lambda_C$  is about 0.055 (Fig. 4b) consistent with a high-quality photonic crystal structure. Due to the directionality of the stop-band reflection the best reflection spectra are detected with low numerical aperture lenses on well oriented opal surface (Fig. 4b).

The distance that light can penetrate into a photonic crystal (in the direction and frequency of the stop-band) is characterized by the Bragg attenuation length  $l_B=2d/[\pi\cdot(\Delta\lambda/\lambda_C)]$ , where  $d$  is the distance of reflecting planes (in the present case the period of (111) planes is about 288 nm) [16]. For the ordered areas of the opals we therefore obtain Bragg lengths as short as 3.3  $\mu\text{m}$  (i.e. less than 12 planes). Implantation or impregnation of opals with Si nanocrystals does not change the position or width of the stop-band significantly. The variations within a sample (due to varying crystalline quality) are much more significant.

#### 3.2. Photoluminescence of undoped opals

Under UV-light excitation the opals without Si nanocrystals show a weak bluish PL emission (possibly due to the oxygen-deficiency centers in silica [17]). In Fig. 5a we compare these PL spectra in places with excellent and poor stop-band reflection. At the position of perfect stop-band the PL intensity is reduced by up to 70 % (see Fig. 5b). The full-width at half-maximum (FWHM) is almost equal (more precisely it is about 5% narrower) to the reflection band at the same position on the sample.

This attenuation is comparable to results on emission changes in opals published in the literature. The fact that the attenuation is never complete is explained by Schriemer et al. [18] by a simple model taking into account diffuse scattering of light by intrinsic defects. The scattering by opal defects limits the mean free path  $l$  of light propagation to about 15  $\mu\text{m}$  in the best reported opals. Light originating shallower than  $l_B$  is hardly Bragg attenuated while light coming from deeper layers (but smaller than  $l$ ) reveals the stop-band. The attenuation  $A$  of emission in the stop band is related to the mean free path and the Bragg length through the

equation  $A = 1 - (I_B/I)$ . The value of  $A$  is usually between 0.5 and 0.8. [16]. For undoped opal (Fig. 5b) we observe  $A \sim 0.7$ , suggesting that  $l$  should be about 11  $\mu\text{m}$ .

### 3.3. Photoluminescence of implanted opals

Implanted regions of opal shows red photoluminescence with a single wide band typical of Si nanocrystalline materials. Modifications of the PL spectra due to the opal stop-band were partially described in our previous paper [10]. In Fig. 6a we show a micro-PL image of the same area as shown in the reflection image of Fig. 3a. The corresponding PL spectral image is shown in Fig. 6b and PL spectra in Fig. 7. The PL reduction in the stop-band position is up to 50%. The effect is less pronounced than the PL reduction in bare opal, because the implantation by Si-ions at 100 keV affects only the layers close to the surface. A relative decrease in the PL intensity calculated from the upper panel (blue area) is compared with the relative reflection difference on the same opal spots (black line) in Fig. 7b.

### 3.4. Photoluminescence of impregnated opals

The opal impregnated with P-Si colloid reveals also a typical decrease of PL at the stop-band (Fig. 8a). Here the position of the stop-band happens to be near the PL maximum ( $\sim 680$  nm) and the PL depression is observed to be more than 70% (Fig. 8b). We note that the FWHM of the stop-band is equal to the FWHM of the PL dip (38 nm, 100 meV) and that this value is also comparable to the 120-meV homogeneous width of PL spectra of single Si quantum dots [19]. (The FWHM of the whole PL band is about 374 meV, i.e. three times wider than the homogeneous linewidth).

At the long wavelength side of the PL spectrum we observe increased emission. Although the absolute comparison of PL intensity from different places of opal has limited precision due to non-perfect morphology of the opal in this case the effect is observed systematically and is strong enough to be considered as real. Possible explanations of this PL enhancement based on the formation of standing waves at the edges of stop gaps [20] or the escape of diffuse light [16] predict enhancement of emission at the short-wavelength side of the spectrum (at higher frequency than the stop-band). Therefore we can rule them out. We therefore propose that reabsorption of PL from smaller Si NCs by bigger NCs and their reemission is responsible for the apparent PL increase at the long-wavelength edge of the spectrum.

The PL decay of P-Si grains in disordered areas of the opal shows (Fig. 9) a typical stretched exponential decay  $\sim \exp[-(t/\tau)^\beta]$  ( $\tau = 33.2$  ms and  $\beta = 0.765$ ) while the perfectly ordered region of opal gives a decay with a significantly wider distribution of decay rates. There are always both shorter and longer kinetic components and the PL decay curve cannot be fitted with a standard stretched exponential function. Here we fitted the decay curve with two exponential decays ( $\tau = 1.5$   $\mu\text{s}$  and 2.1 ms) added to a stretched exponential identical to that used above.

Since we are comparing decay rates from chemically identical regions of the impregnated opal that differ only in their structural perfection, the broader distribution of decay rates is most likely due to variations in the local density of photonic states. A low density of photonic states at the stop-band frequency and direction decreases the probability of spontaneous emission (PL) while defects in the structure localize photonic states (like defects inside band-gaps of semiconductors) and increase the rate of emission [21].

### 3.5. Local variations of photoluminescence intensity

In order to confirm that local variations in the PL intensity are due to structural variations we studied micro-PL images with high magnification. For this experiment we used only implanted opals where the distribution of Si NCs is very homogeneous (in contrast to

impregnated opals with P-Si colloids that do not necessarily provide an equal distribution of nanocrystals). In Fig. 10 we show high magnification images (objective lens 100 $\times$ , NA = 0.73) of reflection (A) and photoluminescence (B) on the implanted opal (area with excellent stop-band in average reflection view). Panels (C) and (D) plot the respective intensity profiles (average intensity being normalized to unity). One can see that intensity variations are mainly within 20% (and sometimes 40%) of the average value. In some locations we observe correlations between decreased reflection and increased PL. We speculate that this is due to structural defects (e.g. several missing opal beads). In Fig. 11 we show one such place which has shape of a ring (micro-PL image in the inset of Fig. 11). The PL intensity in the ring is about 20 % higher than out of the ring (Fig. 11). The stop-band signature is missing in the PL spectrum as we use the objective with high NA that mixes signal leaving the sample within a wide solid angle.

A deeper understanding of the processes responsible for variations in the spontaneous emission rate and variations of the PL intensity is the subject of further study.

#### IV. Conclusions

We have prepared light-emitting Si nanocrystals inside artificial opals by means of Si-implantation or impregnation with porous Si suspensions. In both cases we observed significant changes of Si-NC luminescence at the opal stop-band frequency in directions perpendicular to the opal (111) surface. The luminescence intensity was shown to be reduced by as much as 75 % at the stop band mainly due to Bragg-reflection attenuation. There is also a signature of enhanced PL at the red-edge of PL spectra of Si NCs impregnated in the perfect opal structure which is interpreted as absorption and reemission of PL within the inhomogeneously broadened PL band. PL decay times for Si NCs embedded in well ordered opal was also shown to exhibit new slower as well as faster components compared to the standard stretched exponential decay of Si NCs. These observations demonstrate that photonic crystals can have a significant effect on the broadband emission of silicon nanocrystals and suggest that more refined photonic structures could have potential application for novel Si-based optoelectronic devices and structures.

#### Acknowledgement

This work was supported by the Czech Ministry of education, youth and sports through the research centre LC510 and the research plan MSM0021620835. Partial support from the Australian Research Council and the Royal Swedish Academy of Sciences is also acknowledged.

#### Figure captions

**Figure 1.** Colour reflection micro-photographs of two opal samples used in this study. The white bars are 0.2 mm long. Regions with low omnisppectral diffuse reflection and strong red reflection due to the stop-band are clearly resolved.

**Figure 2.** (a) Atomic force microscope view of the 15 $\times$ 15  $\mu$ m surface of one opal sample. (b) Two-dimensional spatial Fourier transform of the upper figure showing clearly the hexagonal structure of the opal. The periodicity and particle size is 288 nm and 333 nm, respectively.

**Figure 3.** (a) Microscopic reflection image of the opal (objective lens 5×, NA=0.13) in false colours (the colour scale is on the right-hand side of the figure). (b) Reflection spectral image of the slit indicated on the upper panel by white lines. Arrows show positions of spectra plotted in Fig.4a.

**Figure 4.** (a) Reflection spectra extracted from different positions in Fig.3b. (b) Relative reflection changes between an ordered and disordered place of the opal sample observed with lenses of different numerical aperture and magnification. Relative band-widths  $\Delta\lambda/\lambda_c$  are indicated.

**Figure 5.** (a) Photoluminescence spectra of the as-prepared opal without silicon nanocrystals. The black and red lines represent spectra from an ordered and disordered area of the opal, respectively. (b) Relative decrease of PL (blue area) calculated from the upper panel compared with relative reflection difference on the ordered and disordered opal spot (black line).

**Figure 6.** (a) Microscopic PL image of the opal (the same area as in Fig.3a) in false colours (the colour scale is on the right-hand side of the figure). (b) PL spectral image of the slit area indicated on the upper panel by white lines.

**Figure 7.** (a) Photoluminescence spectra of the Si<sup>-</sup> ion-implanted opal. The black and red lines represent spectra from ordered and disordered area, respectively. (b) Relative decrease of PL calculated from the upper panel (blue area) compared with relative reflection difference on the same opal spots (black line).

**Figure 8.** (a) Photoluminescence spectra of the opal impregnated with the P-Si colloidal suspension. The black and red lines represent spectra from an ordered and disordered area, respectively. (b) Relative decrease of PL calculated from the upper panel (blue area) compared with relative reflection difference on the same opal spots (black line).

**Figure 9.** Si NC PL decay measured at the wavelength of the stop-band in ordered (black dots) and disordered (red dots) area (the signal was collected from well selected 80×60 μm areas of the opal). The decay in disordered opal can be fitted with a stretch exponential function (blue dashed line) with parameters  $\tau = 33.2 \mu\text{s}$  and  $\beta = 0.765$  while in the ordered opal (continuous blue line) we had to add a fast exponential decay ( $\tau = 1.5 \mu\text{s}$ , amplitude 0.29) and slow exponential component ( $\tau = 2.1 \text{ ms}$ , amplitude 0.011). The curves are normalized to the same peak intensity.

**Figure 10.** High magnification images (objective lens 100×, NA=0.73, false colour represents intensities) of reflection (a) and photoluminescence (b) on the implanted opal (area with excellent stop-band seen at wider reflection view). Panels (c) and (d) plots intensity profiles from areas in panels (a) and (b), respectively. (Average intensity is normalized to unity.)

**Figure 11.** PL spectra measured in (A - black curve) and out (B - red curve) of the light circle. The PL image with detected areas is shown in the inset. (Objective lens 100×, NA=0.73).

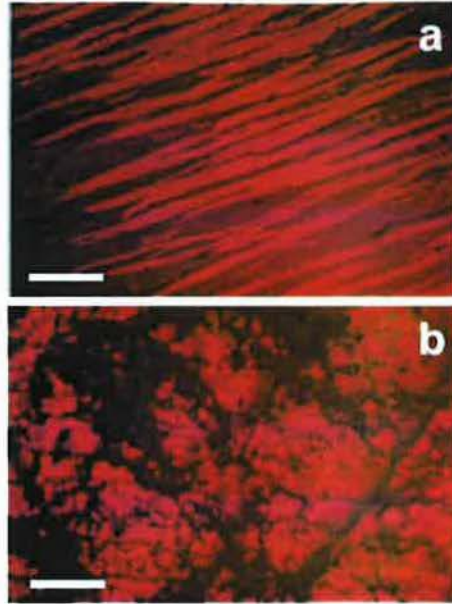


Fig. 1

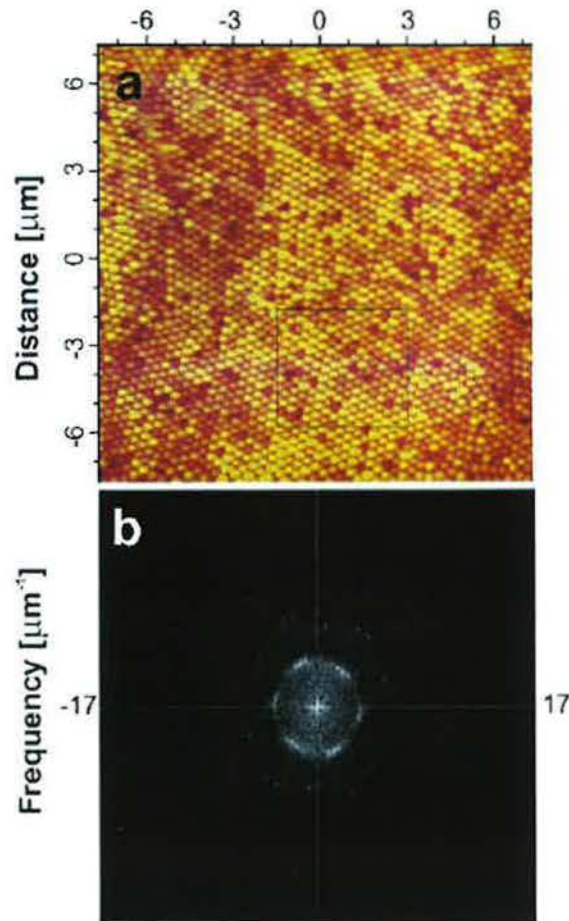


Fig. 2

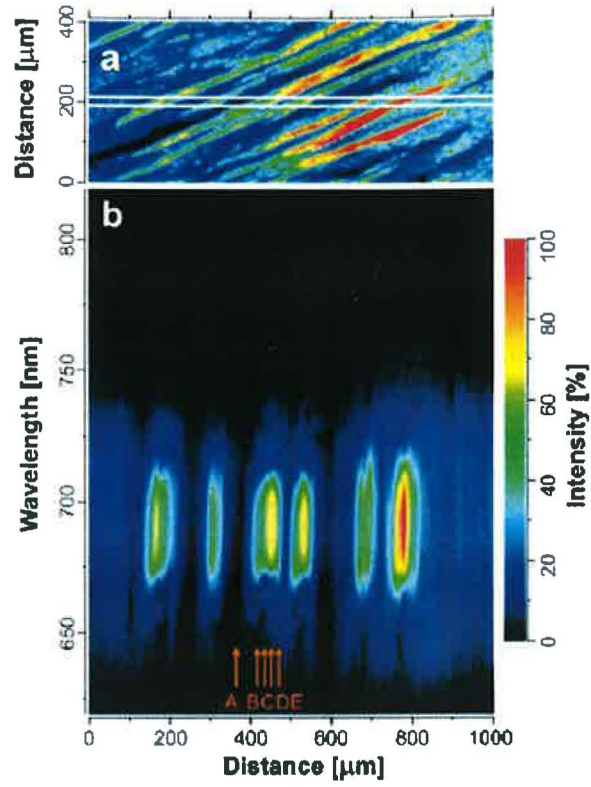


Fig. 3

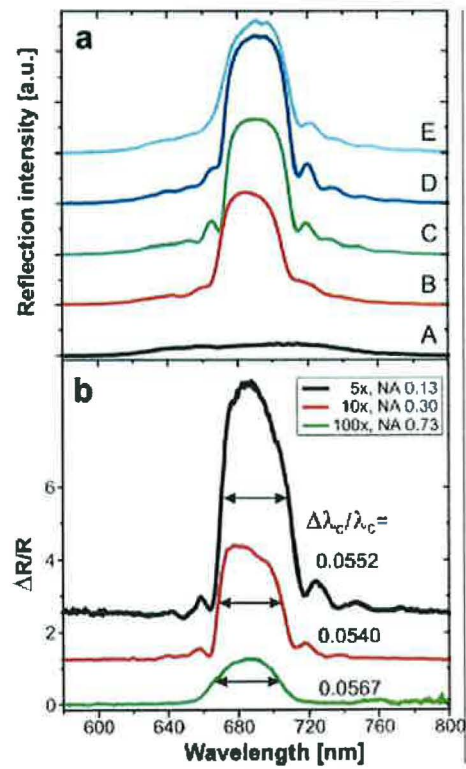


Fig. 4



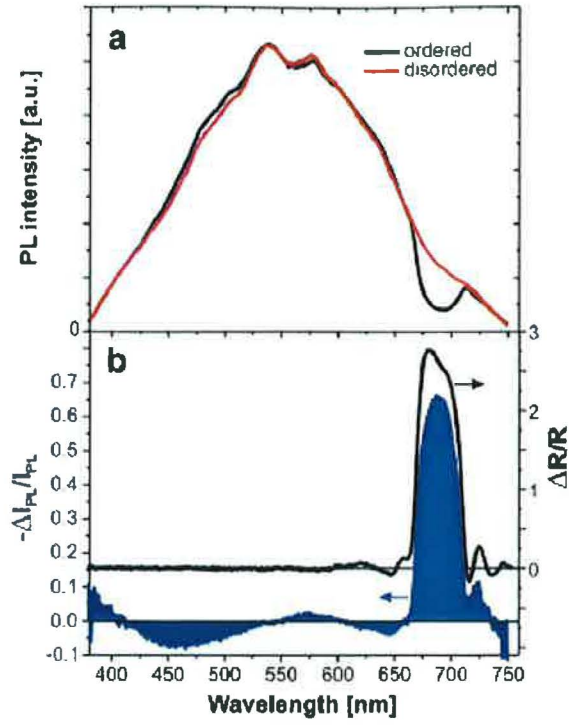


Fig. 5

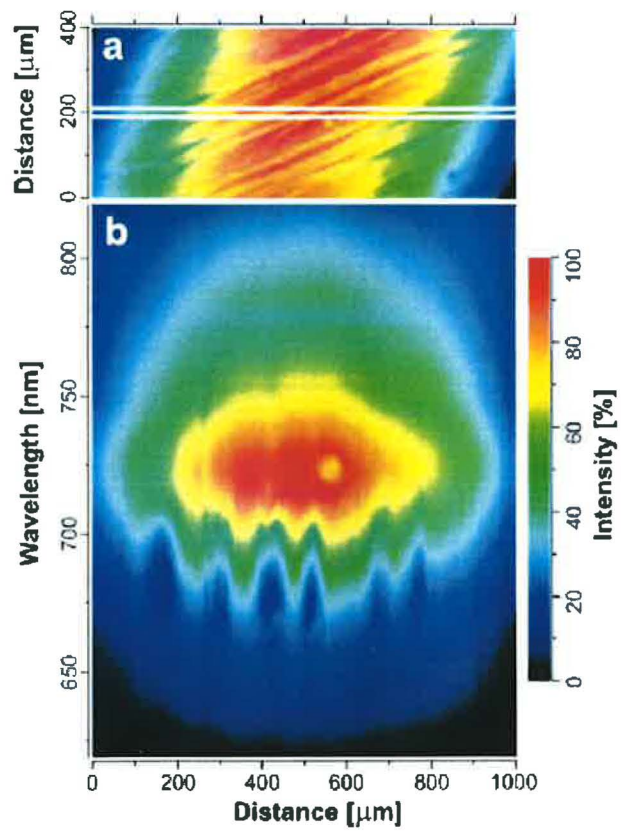


Fig. 6

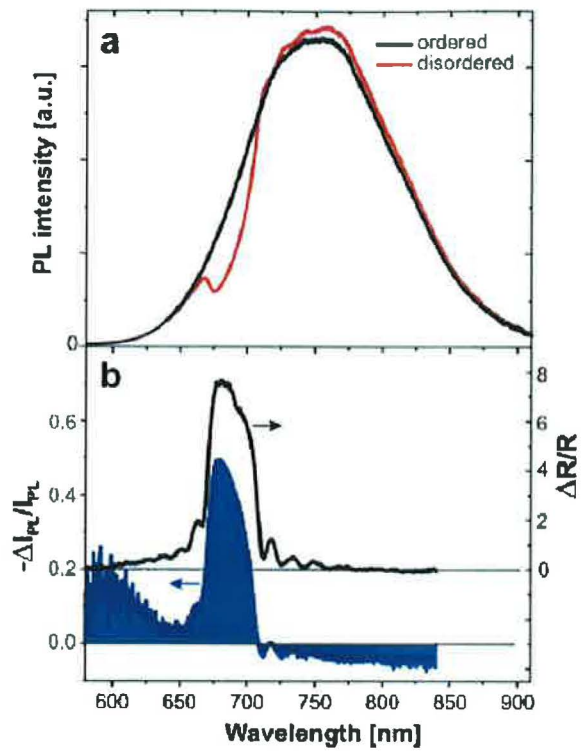


Fig. 7

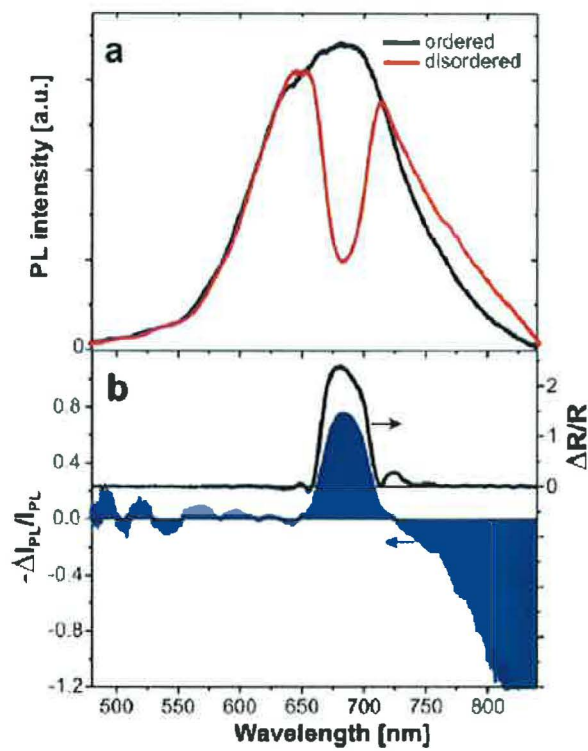


Fig. 8

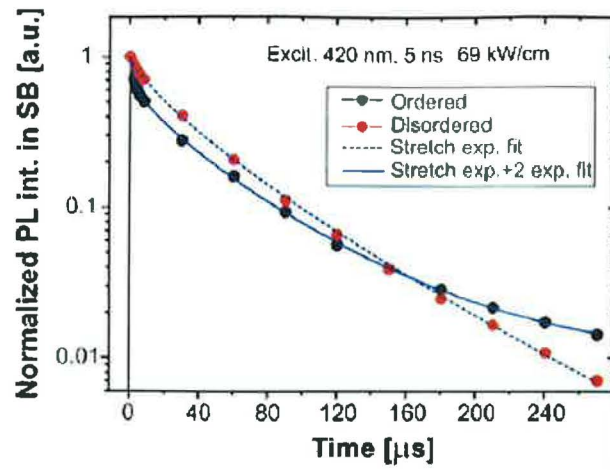


Fig. 9

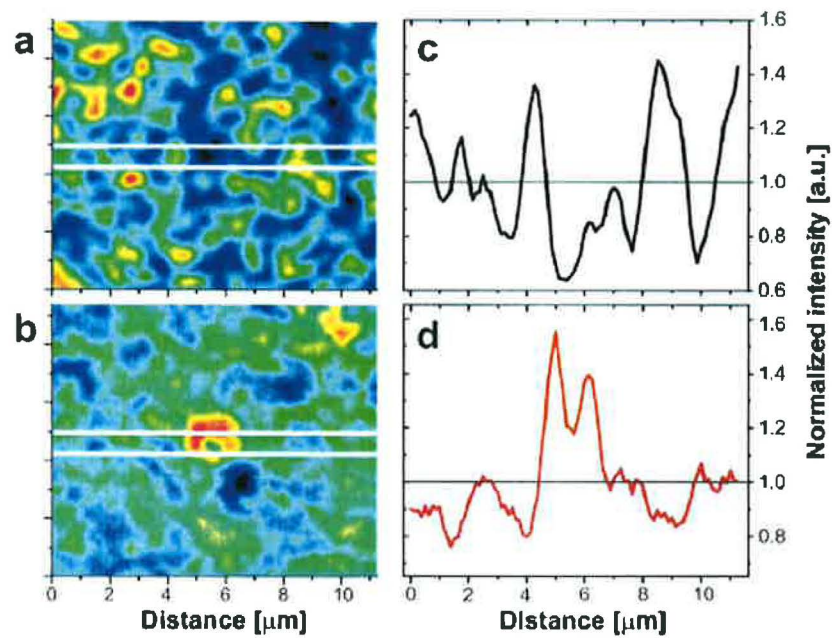


Fig. 10

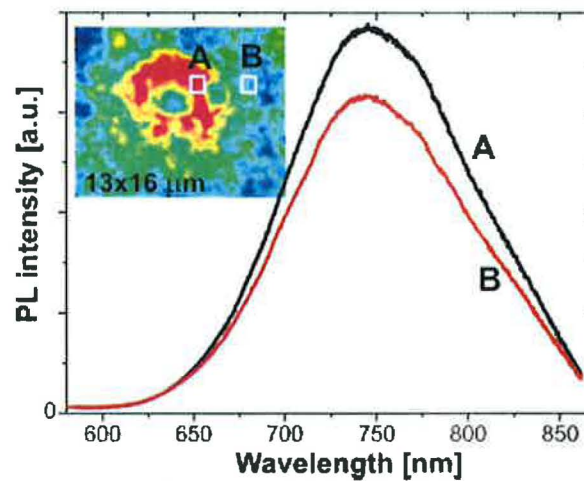


Fig. 11

## References

---

1. S. Ossicini, L. Pavesi, and F. Priolo: *Light emitting silicon for microphotonics*, Springer Verlag 2003
2. I. Pelant, T. Ostatnicky, J. Valenta, K. Luterova, E. Skopalova, T. Mates, and R.G. Elliman: *Appl. Phys. B* **83**, 87 (2006)
3. A. Meldrum, A. Hryciw, K.S. Buchanan, A.M. Beltaos, M. Glover, C.A: Ryan, and J.G.C. Veinot: *Optical Materials* **27**, 812 (2005)
4. E. Jablonovitch: *Phys. Rev. Lett.* **58**, 2059 (1987)
5. M. Fujita, S. Takahashi, Y. Tanaka, T. Asano, and S. Noda: *Science* **308**, 1298 (2005).
6. C. Lopez: *Adv. Mater.* **15**, 1679 (2003)
7. V.N. Bogomolov, S.V. Gaponenko, I.N. Germanenko, A.M. Kapitonov, E.P. Petrov, N.V. Gaponenko, A.V. Prokofjev, A.N. Ponyavina, N.I. Silvanovich, and S.M. Samoilovich: *Phys. Rev. E* **55**, 7619 (1997)
8. C. Díaz-Guerra, J. Piqueras, V.G. Golubev, D.A. Kurdyukov, and A.B. Pevtsov: *J. Appl. Phys.* **90**, 3659 (2001)
9. A.F. Koederink, L. Bechger, H.P. Schriemer, A. Lagendijk, and W.L. Vos: *Phys. Rev. Lett.* **88**, 143903 (2002)
10. J. Valenta, J. Linnros, R. Juhasz, J.-L. Rehspringer, F. Huber, Ch. Hirlimann, S. Cheylan, and R.G. Elliman: *J. Appl. Phys.* **93**, 4471 (2003)
11. S.V. Gaponenko, A.M. Kapitonov, V.N. Bogomolov, A.V. Prokofiev, A. Eychmüller, and A.L. Rogach: *JETP Lett.* **68**, 142 (1998)
12. S.G. Romanov, A.V. Fokin, and R.M. De La Rue: *Appl. Phys. Lett.* **74**, 1821 (1999)
13. Yu.A. Vlasov, M. Deutch, and D.J. Norris: *Appl. Phys. Lett.* **76**, 1627 (2000)
14. M. Barth, A. Gruber, and F. Cichos: *Phys. Rev. B* **72**, 085129 (2005)
15. *The Stopping and Range of Ions in Solids*, by J. F. Ziegler, J. P. Biersack, and U. Littmark, Pergamon Press, New York, 1996
16. L. Bechger, P. Lodahl, and W.L. Vos: *J. Phys. Chem. B* **109**, 9980 (2005)
17. L. Skuja: *J. Non-Crystalline Solids* **239**, 16 (1998)
18. H.P. Schriemer, H.M. van Driel, A.F. Koenderink, and W.L. Vos: *Phys. Rev. A* **63**, 011801 (2000)
19. J. Valenta, R. Juhasz, and J. Linnros: *Appl. Phys. Lett.* **80**, 1070 (2002)
20. A.G. Galstyan, M.E. Raikh, and Z.V. Vardeny: *Phys. Rev. B* **62**, 1780 (2000)
21. L. Novotny and B. Hecht: *Principles of Nano-Optics*, Cambridge university press, 2005